Corps
ers

Waterways Experiment
Station

Numerical Hydrodynamic Modeling and Flushing Study at Maalaea Harbor, Maui, Hawaii

by   *Harry V. Wang, Alan Cialone*

WES

33825538

TA7
W34m
no. CERC-95-8
c.3

Numerical Hydrodynamic Modeling and Flushing Study at Maalaea Harbor, Maui, Hawaii

by   Harry V. Wang, Alan Cialone

U.S. Army Corps of Engineers
Waterways Experiment Station
3909 Halls Ferry Road
Vicksburg, MS   39180-6199

Final report

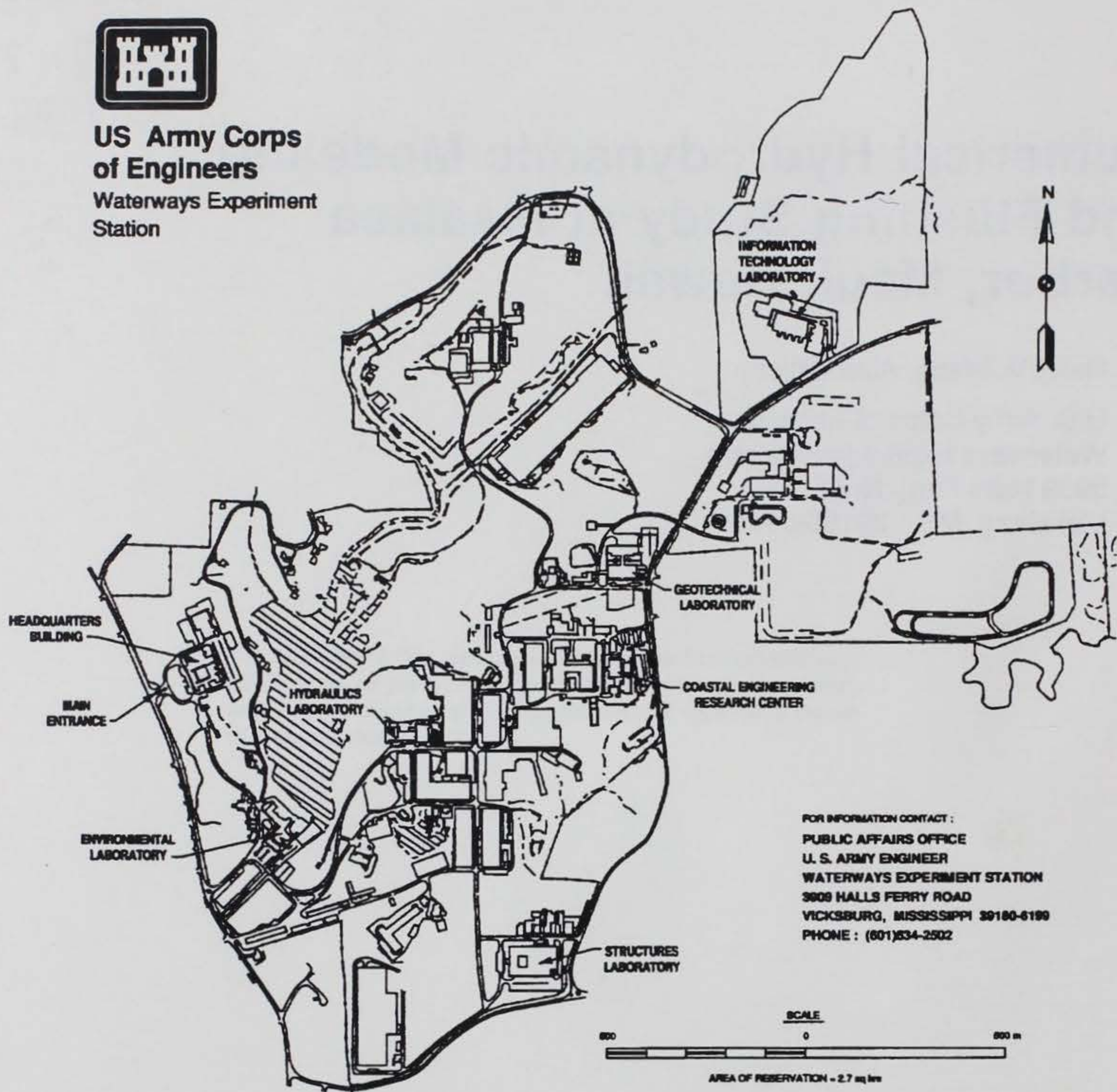Approved for public release; distribution is unlimited

**US Army Corps
of Engineers**
Waterways Experiment
Station

N

SCALE

AREA OF RESERVATION = 2.7 sq km

Contents

SF 298

List of Figures

Preface

This study was authorized by the U.S. Army Engineer Division, Pacific Ocean (POD), and was conducted by personnel of the Coastal Oceanography Branch (COB), Research Division (RD), Coastal Engineering Research Center (CERC), of the U.S. Army Engineer Waterways Experiment Station (WES). The investigation was conducted from June 1993 through November 1994. Mr. Stanley Boc, POD, oversaw progress of the study.

This report was prepared by Dr. Harry V. Wang, Research Physical Scientist, COB, and Mr. Alan Cialone, Civil Engineering Technician, COB. The work was performed under the general supervision of Dr. James R. Houston and Mr. Charles C. Calhoun, Jr., Director and Assistant Director, respectively, CERC. Direct supervision of this project was provided by Mr. H. Lee Butler, Chief, RD, and Dr. Martin C. Miller, Chief, COB, CERC.

The authors wish to thank Dr. K. R. Jin and Mr. John Ehrgott of Mississippi State University for their participation in generating a curvilinear numerical grid for complicated geometry. The logistics support provided by the Maalaea Harbor Master and the U.S. Coast Guard during the summer 1993 field experiment are also greatly appreciated.

The authors also wish to acknowledge excellent support from the Prototype Measurement and Analysis Branch, Engineering Development Division, CERC, in providing the following contributions: experiment planning by Mr. William Kucharski and Ms. Linda Lillycrop; prototype field measurements by Mr. Larry Caviness; and tidal data analysis by Mr. William D. Corson.

Dr. Robert W. Whalin was Director of WES during the study and publication of this report. COL Leonard G. Hassell, EN, was Commander of WES during early phases of this study. At the time of publication of this report, COL Bruce K. Howard, EN, was WES Commander.

Conversion Factors, Non-SI to SI Units of Measurement

Non-SI units of measurement used in this report can be converted to SI units as follows:

Multiply	By	To Obtain
acres	4046.856	square meters
feet	0.3048	meters
knots (international)	0.514444	meters per second
miles (U.S. nautical)	1.852	kilometers

1 Introduction

Maalaea Harbor is located on the southwest coast of the Island of Maui, Hawaii, approximately 8 miles[1] south of Kahului (Figure 1). The existing harbor facility consists of a 90-ft-wide, 12-ft-deep channel and an 11.3-acre dredged basin. The Harbor is surrounded by a 100-ft-long, 90-ft-wide break-water on the south side of the basin, an 870-ft-long breakwater on the east side, and a 300-ft-long, 50-ft-wide paved wharf on the north side of the basin (Figure 2).

During severe wave conditions, Maalaea Harbor experiences harbor surge and navigation difficulties in the entrance channel. The surge results from the existing configuration and alignment of the harbor entrance, which allow direct wave propagation through the channel opening. Surge problems cause naviga-tional hazards and prevent safe berthing in some portions of the harbor (Lillycrop et al. 1993). In early 1980, a hydraulic model study was conducted at the Coastal Engineering Research Center, U.S. Army Engineer Waterways Experiment Station (WES), to investigate the stability of the various break-water cross sections considered in the proposed plans of improvement. Details of the study are provided in Carver and Markle (1981) and in the "General Design Memorandum for Maalaea Harbor for Light-Draft Vessels" (U.S. Army Engineer Division, Pacific Ocean 1980).

While the improvements are aimed at the navigation and economic issues described above, it is important that the proposed designs have sound technical bases in meeting the environmental design criteria for small harbors (U.S. Environmental Protection Agency 1985). One of the key criteria in measuring the physical influence of water on the aquatic system is the flushing time; the amount of time that it takes to exchange the water within the harbor with the receiving water body.

In estimating flushing time, the tidal prism technique has been widely used (Harleman 1966, Dyer 1973, Callaway 1981, van de Kreeke 1983). However, the tidal prism method has two severe limitations for this application: (a) it does not account for wind effects, which are important factors in Maalaea

---

[1] A table of factors for converting non-SI units of measurement to SI units is presented on page viii.
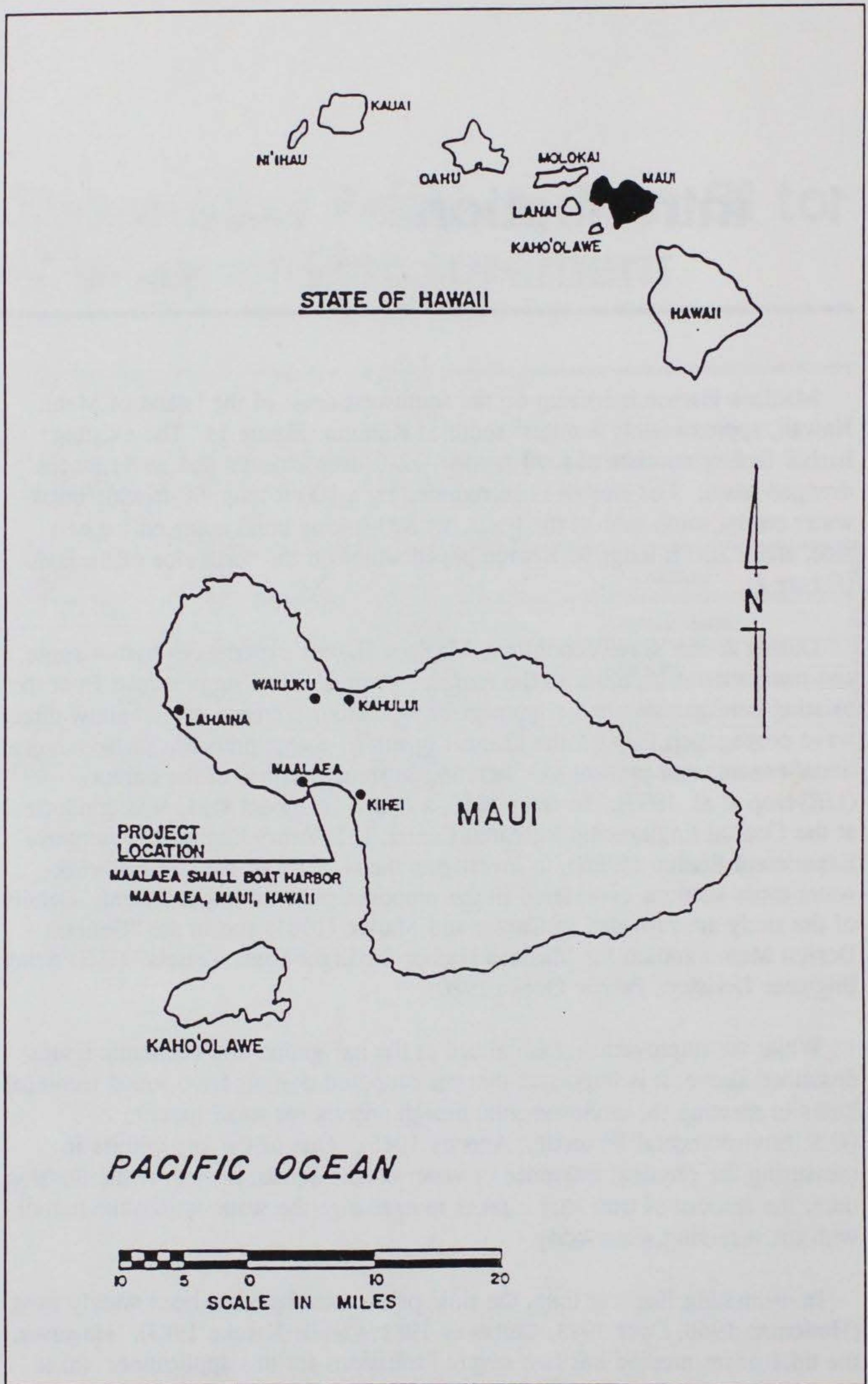
Figure 1.   Study location
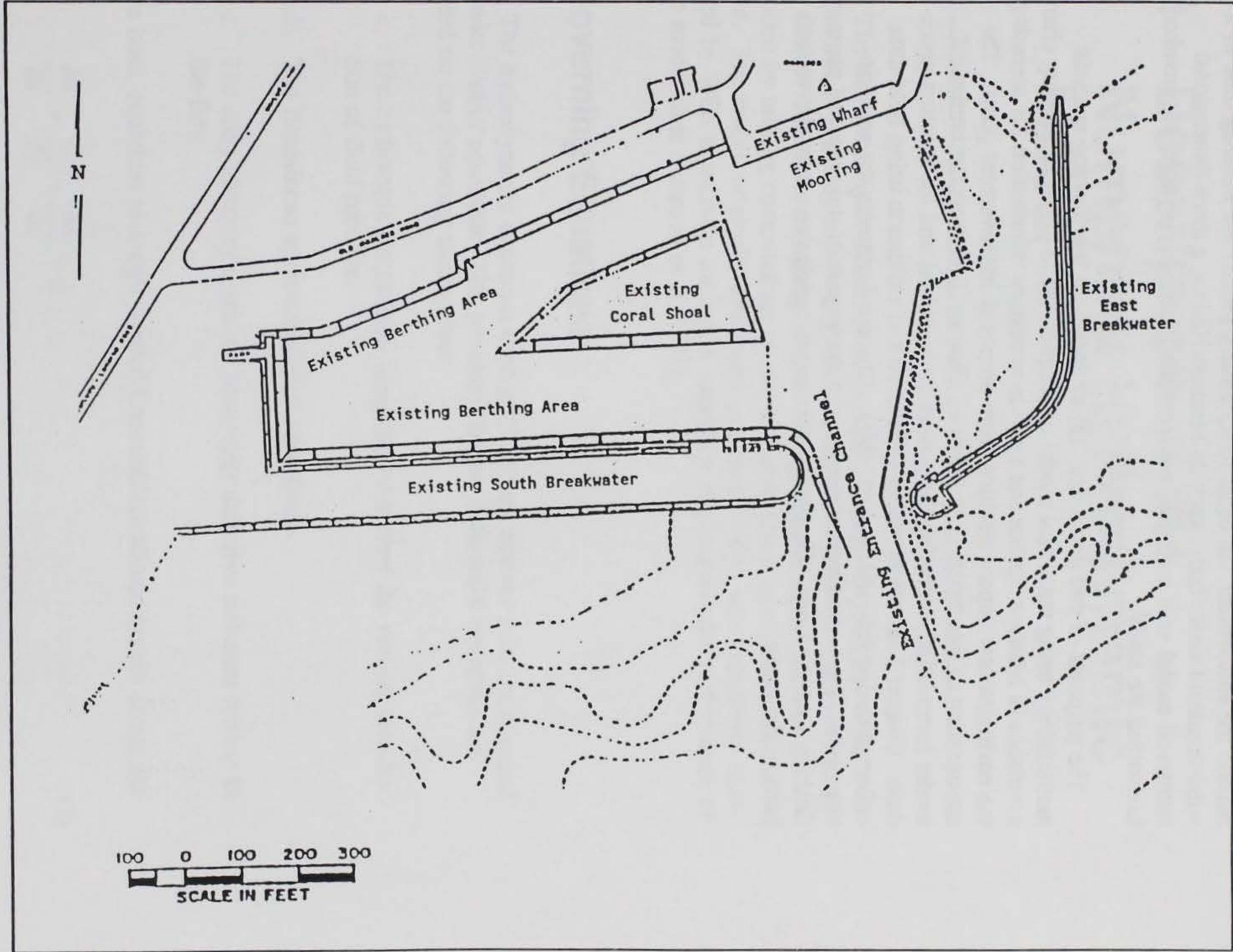
Figure 2. Existing harbor conditions

Harbor, and (b) it assumes that the receiving water body is well-flushed within tidal cycles. As pointed out by Sanford, Boicourt, and Rives (1992), the tidal flushing of the embayment depends not only on the embayment's channel currents, but also on the coastal currents and on the amount of mixing that occurs outside the embayment. In order to accurately predict the flushing time in a wind-dominant water body, such as Maalaea Harbor, a three-dimensional numerical model with a domain covering the harbor-bay system was invoked to conduct the study.

The purposes of this report are: (a) to document the flushing analysis methodology using numerical model techniques, (b) to estimate flushing characteristics in Maalaea Harbor and provide necessary information for assessing the environmental impact resulting from proposed improvement plans. The organization of this report is as follows: Chapter 2 presents the numerical model formulation, including the governing equations and the solution procedure. Chapter 3 describes model calibration and validation using field data collected during July and August, 1993. Chapter 4 presents the scenario description, the hydrodynamic results, and the impact of the proposed plans on flushing characteristics. Chapter 5 summarizes conclusions from the various parts of the study.

2 Description of the Numerical Hydrodynamic Model

The numerical hydrodynamic model used in this study is CH3D-WES (Curvilinear Hydrodynamics in Three Dimensions-WES). The salient feature of CH3D-WES is its capability of resolving the complex geometries in the system by making computations on the boundary-fitted curvilinear planform grid. The model, originally developed by Sheng (1986), was extensively modified by WES to enhance the model capability and improve the performance of the model code (Johnson et al. 1991).

Governing Equations

The hydrodynamic equations used in CH3D are derived from the classical Navier-Stokes equations. The governing partial differential equations are based on the following assumptions:

a. The hydrostatic distribution adequately describes the vertical distribution of fluid pressure.

b. The Boussinesq approximation is appropriate.

c. The eddy viscosity approach adequately describes turbulent mixing in the flow.

The basic equations in a right-handed Cartesian coordinate system (x,y,z) are:

$$\frac{\partial u}{\partial x} + \frac{\partial v}{\partial y} + \frac{\partial w}{\partial z} = 0 \tag{1}$$

$$\frac{\partial u}{\partial t} + \frac{\partial u^2}{\partial x} + \frac{\partial uv}{\partial y} + \frac{\partial uw}{\partial z} = fv - \frac{1}{\rho_o} \frac{\partial p}{\partial x}$$

$$+ \frac{\partial}{\partial x}\left(A_H \frac{\partial u}{\partial x}\right) + \frac{\partial}{\partial y}\left(A_H \frac{\partial u}{\partial y}\right) + \frac{\partial}{\partial z}\left(A_v \frac{\partial v}{\partial z}\right) \tag{2}$$

$$\frac{\partial v}{\partial t} + \frac{\partial uv}{\partial x} + \frac{\partial v^2}{\partial y} + \frac{\partial vw}{\partial z} = -fu - \frac{1}{\rho_o} \frac{\partial p}{\partial y}$$

$$+ \frac{\partial}{\partial x}\left(A_H \frac{\partial v}{\partial x}\right) + \frac{\partial}{\partial y}\left(A_H \frac{\partial v}{\partial y}\right) + \frac{\partial}{\partial z}\left(A_v \frac{\partial v}{\partial z}\right) \tag{3}$$

$$\frac{\partial p}{\partial z} = -\rho g \tag{4}$$

$$\frac{\partial T}{\partial t} + \frac{\partial uT}{\partial x} + \frac{\partial vT}{\partial y} + \frac{\partial wT}{\partial z}$$

$$= \frac{\partial}{\partial x}\left(K_H \frac{\partial T}{\partial x}\right) + \frac{\partial}{\partial y}\left(K_H \frac{\partial T}{\partial y}\right) + \frac{\partial}{\partial z}\left(K_v \frac{\partial T}{\partial z}\right) \tag{5}$$

$$\frac{\partial S}{\partial t} + \frac{\partial uS}{\partial x} + \frac{\partial vS}{\partial y} + \frac{\partial wS}{\partial z} = \frac{\partial}{\partial x}\left(K_H \frac{\partial S}{\partial x}\right)$$

$$+ \frac{\partial}{\partial y}\left(K_H \frac{\partial S}{\partial y}\right) + \frac{\partial}{\partial z}\left(K_v \frac{\partial S}{\partial z}\right) \tag{6}$$

$$\rho = \rho\,(T,S) \tag{7}$$

where

(u,v,w) = velocities in x,y, and z directions, respectively

t = time

f = Coriolis parameter defined as $2\Omega \sin \phi$

Ω = rotational speed of the earth

ϕ = latitude

ρ = density

p = pressure

A_H, K_H = horizontal turbulent eddy coefficients

A_v, K_v = vertical turbulent eddy coefficients

g = gravitational acceleration

T = temperature

S = salinity

Equation 4 implies that vertical accelerations are negligible and thus the pressure is hydrostatic. Various forms of the equation of state can be specified for Equation 7. In the present model, the formulation given below is used:

$$\rho = P/(\alpha + 0.698P) \tag{8}$$

where

$$P = 5890 + 38T - 0.375T^2 + 3S$$

$$\alpha = 1779.5 + 11.25T - 0.0745T^2 - (3.8 + 0.01T)S$$

Nondimensionalization of Governing Equations

The dimensionless forms of the governing equations are used to facilitate relative magnitude comparisons of the various terms in the equations. The following dimensionless variables are used:

$$(u^*, v^*, w^*) = (u, v, wX_r/Z_r)/U_r$$
$$(x^*, y^*, z^*) = (x, y, zX_r/Z_r)/X_r)$$
$$(\tau_x^*, \tau_y^*) = (\tau_x^w, \tau_y^w)/\rho_o fZ_r U_r$$
$$t* = tf$$
$$\zeta^* = g\zeta/fU_r X_r = \zeta/S_r$$
$$\rho^* = (\rho - \rho_o)/(\rho_r - \rho_o) \tag{9}$$
$$T^* = (T - T_o)/(T_r - T_o)$$
$$A_H^* = A_H/A_{Hr}$$
$$A_v^* = A_v/A_{vr}$$
$$K_H^* = K_H/K_{Hr}$$
$$K_v^* = K_v/K_{vr}$$

where

(τ_x^w, τ_y^w) = wind stress in x and y directions

ζ = water surface elevation

These definitions yield the following dimensionless parameters in the governing equations:

Vertical Ekman Number: $E_v = A_{vr} / fZ_r^2$

Lateral Ekman Number: $E_H = A_{Hr} / fX_r^2$

Vertical Prandtl (Schmidt) Number: $Pr_v = A_{vr} / K_{vr}$

Lateral Prandtl (Schmidt) Number: $Pr_H = A_{Hr} / K_{Hr}$

(10)

Froude Number: $F_r = U_r / (gZ_r)^{1/2}$

Rossby Number: $R_o = U_r / fX_r$

Densimetric Froude Number: $Fr_D = F_r / \sqrt{\varepsilon}$

where $\varepsilon = (\rho_r - \rho_o) / \rho_o$

S_r, T_r, U_r, ρ_r, X_r, Z_r, A_{Hr}, A_{vr}, K_{Hr}, and K_{vr} are arbitrary reference values of the salinity, temperature, velocity, density, etc.

External-Internal Modes

The basic equations (Equations 1-4) can be integrated over the depth to yield a set of vertically integrated equations for the water surface ζ and unit flow rates U and V in the x and y directions. Using the dimensionless variables (asterisks have been dropped) and the parameters previously defined, the vertically integrated equations constituting the external mode are:

$$\frac{\partial \zeta}{\partial t} + \beta \left(\frac{\partial U}{\partial x} + \frac{\partial V}{\partial y} \right) = 0 \tag{11}$$

$$\frac{\partial U}{\partial t} = -H \frac{\partial \zeta}{\partial x} + \tau_{sx} - \tau_{bx} + V$$

$$- R_o \left[\frac{\partial}{\partial x} \left(\frac{UU}{H} \right) + \frac{\partial}{\partial y} \left(\frac{UV}{H} \right) \right]$$

$$+ E_H \left[\frac{\partial}{\partial x} \left(A_H \frac{\partial U}{\partial x} \right) + \frac{\partial}{\partial y} \left(A_H \frac{\partial U}{\partial y} \right) \right] \qquad (12)$$

$$- \frac{R_o}{Fr_D^2} \frac{H^2}{2} \frac{\partial \rho}{\partial x}$$

$$\frac{\partial V}{\partial t} = - H \frac{\partial \zeta}{\partial y} + \tau_{sy} - \tau_{by} - U$$

$$- R_o \left[\frac{\partial}{\partial x} \left(\frac{UV}{H} \right) + \frac{\partial}{\partial y} \left(\frac{VV}{H} \right) \right]$$

$$+ E_H \left[\frac{\partial}{\partial x} \left(A_H \frac{\partial V}{\partial x} \right) + \frac{\partial}{\partial y} \left(A_H \frac{\partial V}{\partial y} \right) \right] \qquad (13)$$

$$- \frac{R_o}{Fr_D^2} \frac{H^2}{2} \frac{\partial \rho}{\partial y}$$

where

$$\beta = gZr \,/\, f^2 X_r^2 = (R_o \,/\, F_r)^2$$

H = total depth

As will be discussed later, the major purpose of the external mode is to provide the updated water-surface field for input to the internal mode equations.

The internal mode equations from which the 3-D velocity, salinity, and temperature fields are computed are:

$$\frac{\partial hu}{\partial t} = - h \frac{\partial \zeta}{\partial x} + E_v \frac{\partial}{\partial z} \left(A_v \frac{\partial hu}{\partial z} \right) + fv$$

$$- R_o \left(\frac{\partial huu}{\partial x} + \frac{\partial huv}{\partial y} + \frac{\partial huw}{\partial z} \right)$$

$$+ E_H \left[\frac{\partial}{\partial x} \left(A_H \frac{\partial hu}{\partial x} \right) + \frac{\partial}{\partial y} \left(A_H \frac{\partial hu}{\partial y} \right) \right] \qquad (14)$$

$$- \frac{R_o}{Fr_D^2} \left(\int_z^\zeta \frac{\partial \rho}{\partial x} \, dz \right)$$

$$\frac{\partial hv}{\partial t} = -h \frac{\partial \zeta}{\partial y} + E_v \frac{\partial}{\partial z} \left(A_v \frac{\partial hv}{\partial z} \right) - fu$$
$$- R_o \left(\frac{\partial hvu}{\partial x} + \frac{\partial hvv}{\partial y} + \frac{\partial hvw}{\partial z} \right)$$
$$+ E_H \left[\frac{\partial}{\partial x} \left(A_H \frac{\partial hv}{\partial x} \right) + \frac{\partial}{\partial y} \left(A_H \frac{\partial hv}{\partial y} \right) \right]$$
$$- \frac{R_o}{Fr_D^2} \left(\int_z^\zeta \frac{\partial \rho}{\partial y} \, dz \right)$$

(15)

$$W_{k+1/2} = W_{k-1/2} - \left(\frac{\partial uh}{\partial x} + \frac{\partial vh}{\partial y} \right)$$

(16)

$$\frac{\partial hT}{\partial t} = \frac{E_v}{Pr_v} \frac{\partial}{\partial z} \left(K_v \frac{\partial T}{\partial z} \right)$$
$$- R_o \left(\frac{\partial huT}{\partial x} + \frac{\partial hvT}{\partial y} + \frac{\partial hwT}{\partial z} \right)$$
$$+ \frac{E_H}{Pr_H} \left[\frac{\partial}{\partial x} \left(K_H \frac{\partial hT}{\partial x} \right) + \frac{\partial}{\partial y} \left(K_H \frac{\partial hT}{\partial y} \right) \right]$$

(17)

$$\frac{\partial hS}{\partial t} = \frac{E_v}{Pr_v} \frac{\partial}{\partial z} \left(K_v \frac{\partial S}{\partial z} \right)$$
$$- R_o \left(\frac{\partial huS}{\partial x} + \frac{\partial hvS}{\partial y} + \frac{\partial hwS}{\partial z} \right)$$
$$+ \frac{E_H}{Pr_H} \left[\frac{\partial}{\partial x} \left(K_H \frac{\partial hS}{\partial x} \right) + \frac{\partial}{\partial y} \left(K_H \frac{\partial hS}{\partial y} \right) \right]$$

(18)

In these equations h is the thickness of an internal layer; $k+1/2$ and $k-1/2$ represent the top and bottom, respectively, of the kth vertical layer.

Transformation of Governing Equations

The CH3D model utilizes a boundary-fitted or generalized curvilinear planform grid which can be made to conform to flow boundaries, providing a detailed resolution of the complex horizontal geometry of the flow system.

This necessitates the transformation of the governing equations into boundary-fitted coordinates (ξ, η). If only the (x,y) coordinates are transformed, a system of equations similar to those solved by Johnson (1980) for vertically averaged flow fields is obtained. However, in the CH3D model not only are the (x,y) coordinates transformed into the (ξ, η) curvilinear system but the velocity is also transformed such that its components are perpendicular to the (ξ, η) coordinate lines. This is accomplished by employing the definitions below for the components of the Cartesian velocity (u,v) in terms of contravariant components $\bar{u}$ and $\bar{v}$:

$$u = x_\xi \bar{u} + x_\eta \bar{v}$$

$$v = y_\xi \bar{u} + y_\eta \bar{v}$$

(19)

along with the following expressions for replacing Cartesian derivatives

$$f_x = \frac{1}{J} [(fy_\eta)_\xi - (fy_\xi)_\eta]$$

$$f_y = \frac{1}{J} [-(fx_\eta)_\xi + (fx_\xi)_\eta]$$

(20)

where f is an arbitrary variable and J is the Jacobian of the coordinate transformation defined as

$$J = x_\xi y_\eta - x_\eta y_\xi$$

With the governing equations written in terms of the contravariant components of the velocity, boundary conditions can be prescribed on the boundary-fitted grid in the same manner as on a Cartesian grid because $\bar{u}$ and $\bar{v}$ are perpendicular to the curvilinear cell faces (e.g., at a land boundary, either $\bar{u}$ or $\bar{v}$ is set to zero).

The vertical dimension is represented through the use of what is commonly referred to as a sigma-stretched grid. The vertical depth is discretized in a fixed number of layers, each layer equal in thickness to a fixed percentage of the local depth. The sigma-stretched grid is then transformed to a fixed-space grid where the computations are easily performed.

With both the Cartesian coordinates and Cartesian velocity transformed, the following boundary-fitted equations for $\bar{u}$, $\bar{v}$, w, S, and T, to be solved in each vertical layer, are obtained:

$$\frac{\partial h\bar{u}}{\partial t} = -h \left(\frac{G_{22}}{J^2} \frac{\partial \zeta}{\partial \xi} - \frac{G_{12}}{J^2} \frac{\partial \zeta}{\partial \eta} \right)$$

$$+ \frac{h}{J} \left(G_{12}\, \bar{u} + G_{22}\, \bar{v} \right) + \frac{R_o x_\eta}{J^2} \left[\frac{\partial}{\partial \xi} \left(Jy_\xi h\overline{u}\,\overline{u} \right. \right.$$

$$\left. + Jy_\eta h\overline{u}\,\overline{v} \right) + \frac{\partial}{\partial \eta} \left(Jy_\xi h\overline{u}\,\overline{v} + Jy_\eta h\overline{v}\,\overline{v} \right) \right]$$

$$- \frac{R_o y_\eta}{J^2} \left[\frac{\partial}{\partial \xi} \left(Jx_\xi h\overline{u}\,\overline{u} + Jx_\eta h\overline{u}\,\overline{v} \right) \right. \tag{21}$$

$$\left. + \frac{\partial}{\partial \eta} \left(Jx_\xi h\overline{u}\,\overline{v} + Jx_\eta h\overline{v}\,\overline{v} \right) \right] - R_o \left[(w\vec{u})_{top} - (w\vec{u})_{bot} \right]$$

$$+ E_v \left[\left(A_v \frac{\partial \bar{u}}{\partial z} \right)_{top} - \left(A_v \frac{\partial \bar{u}}{\partial z} \right)_{bot} \right] - \frac{R_o h}{Fr_D^2} \left[\int_z^\zeta \left(\frac{G_{22}}{J^2} \frac{\partial \rho}{\partial \xi} \right. \right.$$

$$\left. \left. - \frac{G_{12}}{J^2} \frac{\partial \rho}{\partial \eta} \right) dz \right] + \textit{Horizontal Diffusion}$$

$$\frac{\partial h\bar{v}}{\partial t} = -h \left(- \frac{G_{21}}{J^2} \frac{\partial \zeta}{\partial \xi} + \frac{G_{11}}{J^2} \frac{\partial \zeta}{\partial \eta} \right)$$

$$- \frac{h}{J} \left(G_{11}\, \bar{u} + G_{21}\, \bar{v} \right) - \frac{R_o x_\xi}{J^2} \left[\frac{\partial}{\partial \xi} \left(Jy_\xi h\overline{u}\,\overline{u} \right. \right.$$

$$\left. + Jy_\eta h\overline{u}\,\overline{v} \right) + \frac{\partial}{\partial \eta} \left(Jy_\xi h\overline{u}\,\overline{v} + Jy_\eta h\overline{v}\,\overline{v} \right) \right]$$

$$+ \frac{R_o y_\xi}{J^2} \left[\frac{\partial}{\partial \xi} \left(Jx_\xi h\overline{u}\,\overline{u} + Jx_\eta h\overline{u}\,\overline{v} \right) \right. \tag{22}$$

$$\left. + \frac{\partial}{\partial \eta} \left(Jx_\xi h\overline{u}\,\overline{v} + Jx_\eta h\overline{v}\,\overline{v} \right) \right] - R_o \left[(w\vec{v})_{top} \, (w\vec{v})_{bot} \right]$$

$$+ E_v \left[\left(A_v \frac{\partial \bar{v}}{\partial z} \right)_{top} - \left(A_v \frac{\partial \bar{v}}{\partial z} \right)_{bot} \right]$$

$$- \frac{R_o h}{Fr_D^2} \left[\int_z^\zeta \left(- \frac{G_{21}}{J^2} \frac{\partial \rho}{\partial \xi} + \frac{G_{11}}{J^2} \frac{\partial \rho}{\partial \eta} \right) dz \right]$$

$$+ \textit{Horizontal Diffusion}$$

$$w_{top} = w_{bot} - \frac{1}{J} \left(\frac{\partial J\bar{u}h}{\partial \xi} + \frac{\partial J\bar{v}h}{\partial \eta} \right)$$ (23)

$$\frac{\partial hS}{\partial t} = \frac{E_v}{Pr_v} \left[\left(K_v \frac{\partial S}{\partial z} \right)_{top} - \left(K_v \frac{\partial S}{\partial z} \right)_{bot} \right]$$

$$- \frac{R_o}{J} \left(\frac{\partial hJ\bar{u}S}{\partial \xi} + \frac{\partial hJ\bar{v}S}{\partial \eta} \right)$$ (24)

$$- R_o \left[(wS)_{top} - (wS)_{bot} \right]$$

+ Horizontal Diffusion

$$\frac{\partial hT}{\partial t} = \frac{E_v}{Pr_v} \left[\left(K_v \frac{\partial T}{\partial z} \right)_{top} - \left(K_v \frac{\partial T}{\partial z} \right)_{bot} \right]$$

$$- \frac{R_o}{J} \left(\frac{\partial hJ\bar{u}T}{\partial \xi} + \frac{\partial hJ\bar{v}T}{\partial \eta} \right)$$ (25)

$$- R_o \left[(wT)_{top} - (wT)_{bot} \right]$$

+ Horizontal Diffusion

where

$$G_{11} = x_\xi^2 + y_\xi^2$$

$$G_{22} = x_\eta^2 + y_\eta^2$$ (26)

$$G_{12} = G_{21} = x_\xi x_\eta + y_\xi y_\eta$$

Similarly, the transformed external mode equations become:

$$\frac{\partial \zeta}{\partial t} + \beta \left(\frac{\partial \bar{U}}{\partial \xi} + \frac{\partial \bar{V}}{\partial \eta} \right) = 0$$ (27)

$$\frac{\partial \bar{U}}{\partial t} = -\frac{H}{J^2}\left(G_{22}\frac{\partial \zeta}{\partial \xi} - G_{12}\frac{\partial \zeta}{\partial \eta}\right)$$

$$+\frac{1}{J}\left(G_{12}\bar{U} + G_{22}\bar{V}\right) + \frac{R_o x_\eta}{J^2 H}\left[\frac{\partial}{\partial \xi}\left(Jy_\xi \bar{U}\bar{U} + Jy_\eta \bar{U}\bar{V}\right)\right.$$

$$\left. + \frac{\partial}{\partial \eta}\left(Jy_\xi \bar{U}\bar{V} + Jy_\eta \bar{V}\bar{V}\right)\right]$$

$$-\frac{R_o y_\eta}{J^2 H}\left[\frac{\partial}{\partial \xi}\left(Jx_\xi \bar{U}\bar{U} + Jx_\eta \bar{U}\bar{V}\right)\right.$$

$$\left. + \frac{\partial}{\partial \eta}\left(Jx_\xi \bar{U}\bar{V} + Jx_\eta \bar{V}\bar{V}\right)\right]$$

$$+\tau_{s\xi} - \tau_{b\xi} - \frac{R_o}{Fr_D^2}\frac{H^2}{2}\left(G_{22}\frac{\partial \rho}{\partial \xi} - G_{12}\frac{\partial \rho}{\partial \eta}\right)$$

$$+ \textit{Horizontal Diffusion}$$

(28)

$$\frac{\partial \bar{V}}{\partial t} = -\frac{H}{J^2}\left(-G_{21}\frac{\partial \zeta}{\partial \xi} + G_{11}\frac{\partial \zeta}{\partial \eta}\right)$$

$$-\frac{1}{J}\left(G_{11}\bar{U} + G_{21}\bar{V}\right)$$

$$-\frac{R_o x_\xi}{J^2 H}\left[\frac{\partial}{\partial \xi}\left(Jy_\xi \bar{U}\bar{U} + Jy_\eta \bar{U}\bar{V}\right)\right.$$

$$\left. + \frac{\partial}{\partial \eta}\left(Jy_\xi \bar{U}\bar{V} + Jy_\eta \bar{V}\bar{V}\right)\right]$$

$$+\frac{R_o y_\xi}{J^2 H}\left[\frac{\partial}{\partial \xi}\left(Jx_\xi \bar{U}\bar{U} + Jx_\eta \bar{U}\bar{V}\right)\right.$$

$$\left. + \frac{\partial}{\partial \eta}\left(Jx_\xi \bar{U}\bar{V} + Jx_\eta \bar{V}\bar{V}\right)\right]$$

$$+\tau_{s\eta} - \tau_{b\eta} - \frac{R_o}{Fr_D^2}\frac{H^2}{2}\left(-G_{21}\frac{\partial \rho}{\partial \xi} + G_{11}\frac{\partial \rho}{\partial \eta}\right)$$

$$+ \textit{Horizontal Diffusion}$$

(29)

Equations 27-29 are solved first to yield water-surface elevations, which are then used to evaluate the water-surface slope terms in the internal mode equations. The horizontal diffusion terms are quite lengthy and thus are omitted in

14

this report. Full documentation of the terms is presented in Johnson et al. (1991) for the internal mode equations. Similar expressions for the diffusion terms in the vertically averaged equations can be inferred from those for the internal mode.

Finite Difference Scheme

Finite differences are used to replace derivatives in the governing equations, resulting in a system of linear algebraic equations to be solved in both the external and internal modes. The external mode solution consists of the surface displacement and vertically integrated contravariant unit flows $\bar{U}$ and $\bar{V}$. All terms in the transformed vertically averaged continuity equation are treated implicitly whereas only the water-surface slope terms in the transformed vertically averaged momentum equations are treated implicitly. If the external mode is used only as a vertically averaged model, the bottom friction is also treated implicitly. Those terms treated implicitly are weighted between the new and old time-steps. The resulting finite difference equations are then factored such that a ξ-sweep followed by an η-sweep of the horizontal grid yields the solution at the new time-step.

Writing Equations 11-13 as

$$\frac{\partial \zeta}{\partial t} + \beta \left(\frac{\partial \bar{U}}{\partial \xi} + \frac{\partial \bar{V}}{\partial \eta} \right) = 0 \tag{30}$$

$$\frac{\partial \bar{U}}{\partial t} + \frac{H}{J^2} G_{22} \frac{\partial \zeta}{\partial \xi} = M \tag{31}$$

$$\frac{\partial \bar{V}}{\partial t} + \frac{H}{J^2} G_{11} \frac{\partial \zeta}{\partial \eta} = N \tag{32}$$

ξ-sweep $\Rightarrow$

$$\zeta_{ij}^* + \frac{\beta\theta\Delta t}{\Delta \xi} \left(\bar{U}_{i+1,j}^* - \bar{U}_{ij}^* \right) = \zeta_{ij}^n$$

$$- (1 - \theta)\frac{\Delta t}{\Delta \xi} \left(\bar{U}_{i+1,j}^n - \bar{U}_{ij}^n \right) \tag{33}$$

$$- \frac{\Delta t}{\Delta \eta} \left(\bar{V}_{i,j+1}^n - \bar{V}_{ij}^n \right)$$

$$\bar{U}_{ij}^{n+1} + \frac{\theta \Delta t H G_{22}}{\Delta \xi J^2} \left(\zeta_{ij}^{*} - \zeta_{i-1,j}^{*} \right) = \bar{U}_{ij}^{n}$$

$$- (1 - \theta) \frac{\Delta t H G_{22}}{\Delta \xi J^2} \left(\zeta_{ij}^{n} - \zeta_{i-1,j}^{n} \right) + \Delta t \, M^{n} \tag{34}$$

and the η-sweep then provides the updated ζ and V at the $n+1$ time level.

η - sweep $\Rightarrow$

$$\zeta_{ij}^{n+1} + \frac{\beta \theta \Delta t}{\Delta \eta} \left(\bar{V}_{i,j+1}^{n+1} - \bar{V}_{ij}^{n+1} \right) = \zeta_{ij}^{*}$$

$$- (1 - \theta) \frac{\Delta t}{\Delta \eta} \left(\bar{V}_{i,j+1}^{n} - \bar{V}_{ij}^{n} \right) \tag{35}$$

$$+ \frac{\Delta t}{\Delta \eta} \left(\bar{V}_{i,j+1}^{n} - \bar{V}_{ij}^{n} \right)$$

$$\bar{V}_{ij}^{n+1} + \frac{\theta \Delta t H G_{11}}{\Delta \eta J^2} \left(\zeta_{i,j+1}^{n+1} - \zeta_{ij}^{n+1} \right) = V_{ij}^{n}$$

$$- (1-\theta) \frac{\Delta t H G_{11}}{\Delta \eta J^2} \left(\zeta_{i,j+1}^{n} - \zeta_{ij}^{n} \right) + \Delta t \, N^{n} \tag{36}$$

A typical value of θ of 0.55 yields stable and accurate solutions.

The internal mode consists of computations from Equations 21-25 for the three velocity components ($\bar{u}$, $\bar{v}$, and w), salinity, and temperature. The only terms treated implicitly are the vertical diffusion terms in all equations and the bottom friction and surface slope terms in the momentum equations. Values of the water-surface elevations from the external mode are used to evaluate the surface slope terms in Equations 21 and 22. As a result, the extremely restrictive speed of a free-surface gravity wave is removed from the stability criteria. Roache's second upwind differencing scheme is used to represent the convective terms in the momentum equations, whereas a spatially third-order scheme developed by Leonard (1979) (called QUICKEST) is used to represent the advective terms in Equations 24 and 25 for salinity and temperature, respectively. For example, if the velocity on the right face of a computational cell is positive, then with QUICKEST the value of the salinity used to compute the flux through the face is

$$S_R = \frac{1}{2} \left(S_{i,j,k} + S_{i+1,j,k} \right)$$

$$-\frac{1}{6} \left[1 - \left(\bar{U}_{i+1,j,k} \Delta \frac{t}{\Delta \xi} \right)^2 \right] (S_{i+1,j,k}$$

$$- 2 S_{i,j,k} + S_{i-1,j,k})$$

$$-\frac{1}{2} U_{i+1,j,k} \Delta \frac{t}{\Delta \xi} \left(S_{i+1,j,k} - S_{i,j,k} \right)$$

(37)

The more interested reader is referred to the paper by Leonard (1979).

It should be noted that once the $\bar{u}$ and $\bar{v}$ velocity components are computed, they are slightly adjusted to ensure conservation of mass. This is accomplished by forcing the sum of $\bar{u}$ over the vertical to be the vertically averaged velocity U/H and the sum of $\bar{v}$ over the vertical to equal V/H, where H is the total water depth.

Turbulence Parameterization

Vertical turbulence is handled by using the concepts of eddy viscosity and diffusivity to represent the velocity and density correlation terms that arise from time averaging of the governing equations. These eddy coefficients are computed from mean flow characteristics using a simplified second-order closure model originally developed by Donaldson (1973). The closure model has been further developed and applied to various types of flows by Lewellen (1977) and Sheng (1982, 1986). A discussion of the implementation of the turbulence model taken from Sheng (1990) follows. For more details, the interested reader should refer to these references and to Johnson et al. (1991).

Assuming local equilibrium of turbulence, i.e., no time evolution or spatial diffusion of the second-order correlations, an equation relating the turbulent kinetic energy and the macro-scale of turbulence to the mean flow shear and stratification (given by the Richardson number Ri) can be derived as

$$3A^2b^2sQ^4 + A[(bs + 3b + 7b^2s)Ri$$

$$- Abs(1 - 2b)]Q^2 + b(s + 3 + 4bs)Ri^2$$

(38)

$$+ (bs - A)(1 - 2b)Ri = 0$$

where

$$b = 0.125$$

$$s = 1.8$$

$$A = 0.75$$

and

$$Q = \frac{q}{\Lambda \sqrt{(\partial \bar{u}/\partial z)^2 + (\partial \bar{v}/\partial z)^2}} \tag{39}$$

In the above expression, q is defined as

$$q = \left(\overline{u'u'} + \overline{v'v'} + \overline{w'w'}\right)^{1/2}$$

and Λ is the macro-scale of turbulence. The quantities u', v', and w' are the turbulent velocity fluctuations and the overbar indicates time averaging. It can also be shown that the following relations hold:

$$\overline{u'w'} = - \frac{\frac{\partial \bar{u}}{\partial z} \Lambda}{q} \frac{1 + \frac{\bar{\omega}}{A}}{1 - \omega} \overline{w'w'} \tag{40}$$

$$\overline{v'w'} = - \frac{\frac{\partial \bar{v}}{\partial z} \Lambda}{q} \frac{1 + \frac{\bar{\omega}}{A}}{1 - \omega} \overline{w'w'} \tag{41}$$

$$q^2 b = \left[\frac{(1 + \frac{\bar{\omega}}{A})}{Q^2(1 - \omega)} + \bar{\omega} \right] \overline{w'w'} \tag{42}$$

where

$$\omega = \frac{Ri}{AQ^2} \tag{43}$$

and

$$\bar{\omega} = \frac{\omega}{1 - \dfrac{\omega}{bs}}$$ (44)

Thus, after the velocity shear and flow stratification are determined, q can be computed from Equations 38 and 39. $\overline{w'w'}$ is then determined from

$$\overline{w'w'} = \frac{\dfrac{q^2}{2} - q^2 b}{\dfrac{3}{2}(1 - 2\omega)}$$ (45)

Finally, after Λ is prescribed, $\overline{u'w'}$ and $\overline{v'w'}$ can be computed from Equations 40 and 41 and the vertical eddy coefficients can be determined from

$$A_v = \frac{-\overline{u'w'}}{\dfrac{\partial \bar{u}}{\partial z}} = \frac{\Lambda}{q} \frac{A + \bar{\omega}}{A(1 - \omega)} \overline{w'w'}$$ (46)

$$K_v = \frac{-\overline{\rho'w'}}{\dfrac{\partial \bar{\rho}}{\partial z}} = \frac{\Lambda}{q} \frac{bs}{(bs - \omega)A} \overline{w'w'}$$ (47)

In addition to setting $\Lambda = 0.65z$ near boundaries, the following three basic constraints are used to compute Λ at a vertical position z:

$$\left| \frac{d\Lambda}{dz} \right| \le 0.65$$ (48)

$$\Lambda \le \frac{q}{N} = ql \left(-\frac{g}{\rho} \frac{\partial \rho}{\partial z} \right)^{0.5}$$ (49)

$$\Lambda \le Q_{cut} \left(z_{q=qmax} - z_{q=qmax/2} \right)$$ (50)

where N is the Brunt-Vaisala frequency. Equation 50 states that Λ is less than a fraction of the spread of turbulence as measured by the distance between the location of a maximum q^2 to where q^2 is equal to 25 percent of the maximum. The coefficient Q_{cut} is on the order of 0.15 to 0.25.

3 Implementation of the Hydrodynamic Model

The preceding chapter discussed the governing equations for CH3D-WES and the finite difference scheme used to solve them. In this chapter, issues related to the actual implementation of the model will be addressed. Three procedures are required to be fulfilled before the numerical model can be enacted; they are: (a) the generation of the computational grid with the topographic information assigned to it, (b) the assigning of the appropriate initial and boundary conditions, and (c) the calibration and validation of the model using field-measured data.

Computational Grid and Topography

The computational grid used in the CH3D-WES allows boundary-fitted coordinates to fit the ship channel and irregular shoreline with accurate and economical grid schematization. With the aid of the grid generation software (Jin 1993), the detailed shoreline configuration including the breakwater and the coral shoal from U.S. Corps of Engineers base map for Maalaea Harbor were all well resolved, as shown in Figure 3. Total grid cells generated in the harbor-bay system were 9,720 with 81 in the east-west, 60 in the north-south and 2 layers in the vertical direction. The average cell size is 50 ft, with the finest resolution measured (25 ft) being mostly concentrated inside the harbor. The computational domain was bounded by the shoreline to the west and to the north, and by open boundaries in the east and the south. The open boundary in the east is about 800 ft from the east breakwater and the open boundary in the south is about 1,100 ft from the harbor entrance.

The topography shown in Figure 4 was read from the 1:800 scale chart and slightly smoothed through the discrete digitization. The greatest depth is 25-30 ft in the southeast portion of the computational domain and is shallowest to the east of the east breakwater with depths of 2-4 ft. The depth in the harbor basin itself is generally 8-10 ft except for a ship channel located from the entrance to the north pier, where the depth is 14-16 ft.
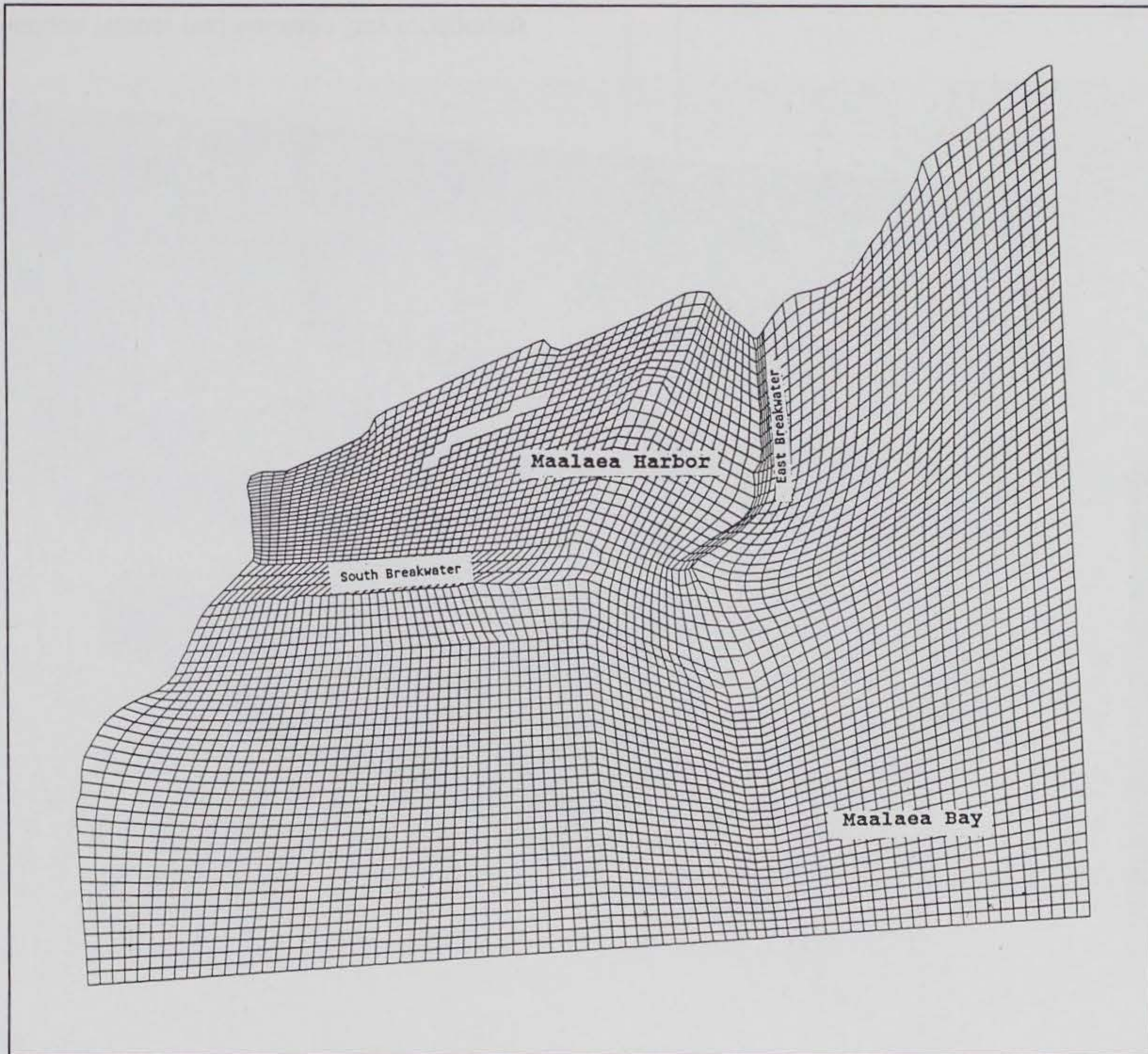
Figure 3. Curvilinear grid layout for Maalaea Harbor and its vicinity

	0.00
	2.21
	4.42
	6.63
	8.84
	11.05
	13.26
	15.47
	17.68
	19.89
	22.10
	24.31
	26.52
	28.73
	30.94
	33.15

(feet)
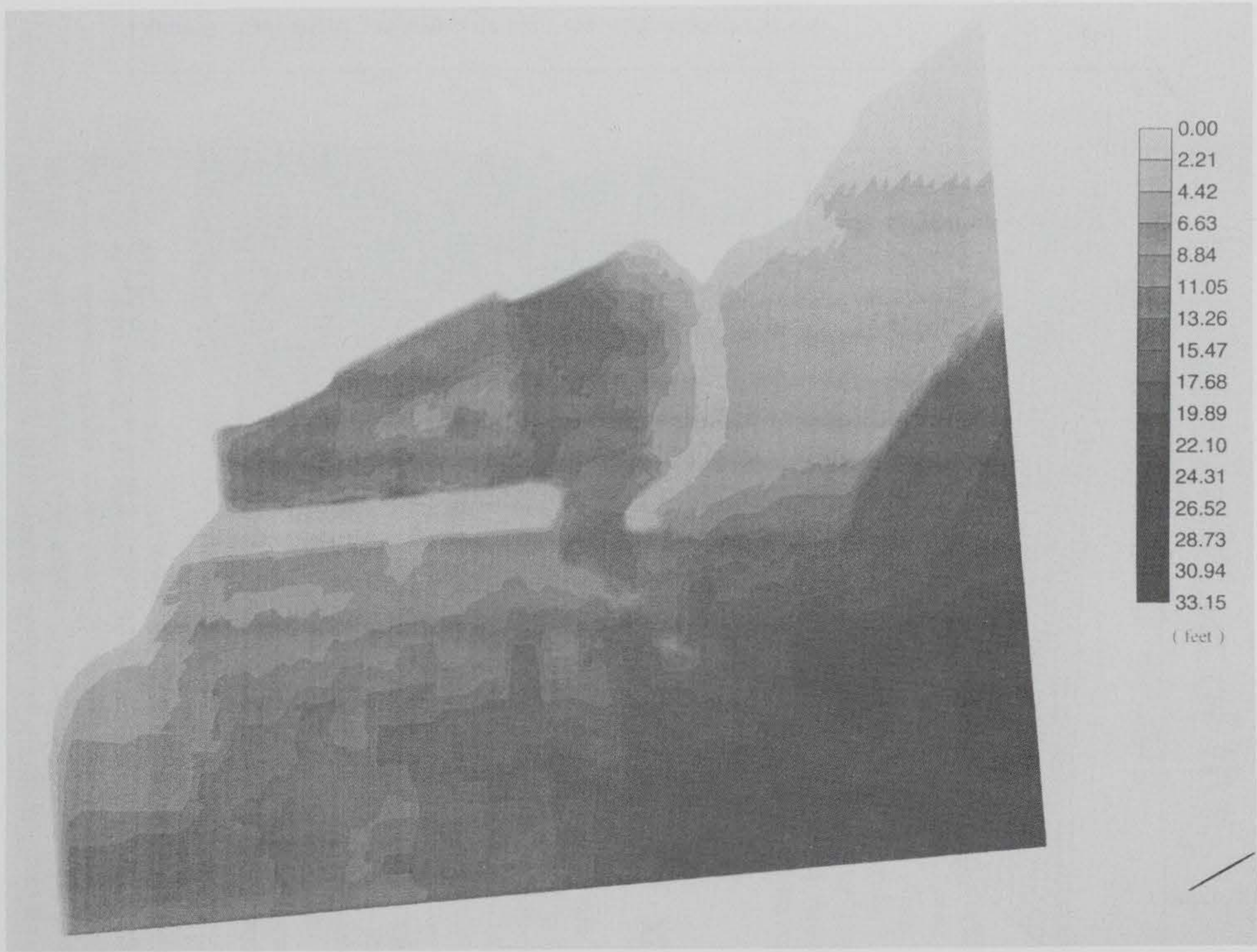
Figure 4.   Maalaea Harbor and Maalaea Bay topography

A vertically stretched, staggered grid scheme is used internally for computation. Figure 5 illustrates schematically the staggered grid, in which vertical velocity is shifted one half an interval relative to the density, while the horizontal velocity grid is shifted by half an interval horizontally relative to density. The vertically stretched grid preserves the same order of vertical resolution for the shallow and deeper part of the water body, which leads to a smooth representation of the topography.

Figure 5. Vertically stretched and staggered numerical grid

Initial and Boundary Conditions

When initiating a run of CH3D-WES, the values of ζ, $\bar{u}$, $\bar{v}$, $\bar{w}$, U and V are set to zero and, values of salinity and temperature are read from input files. Since the salinity and temperature are derived from prototype measurements at a limited number of locations, interpolation and smoothing were required to produce the final 3-D input files. Generally, the salinity and temperature fields are held constant for the first few days of a simulation.
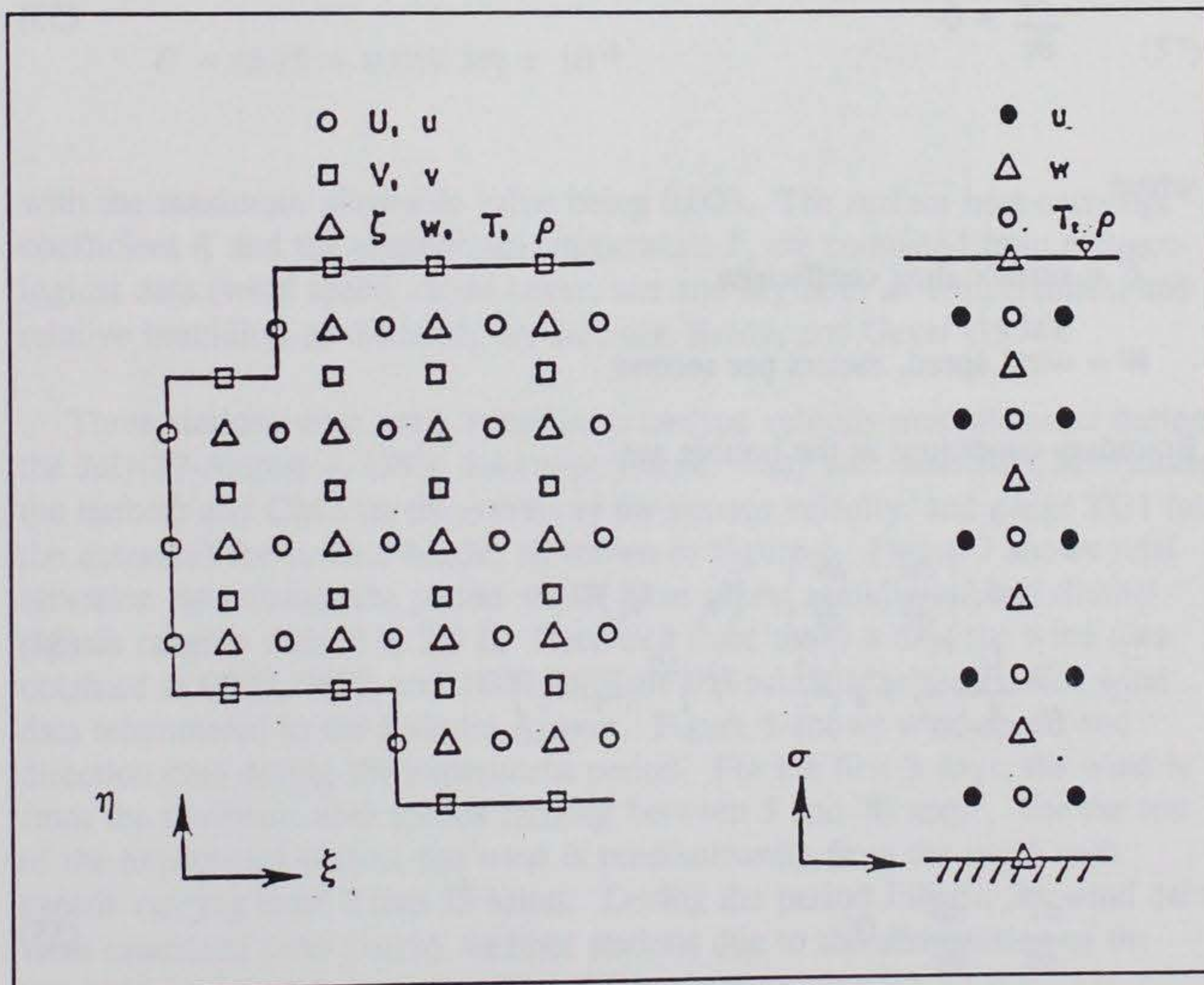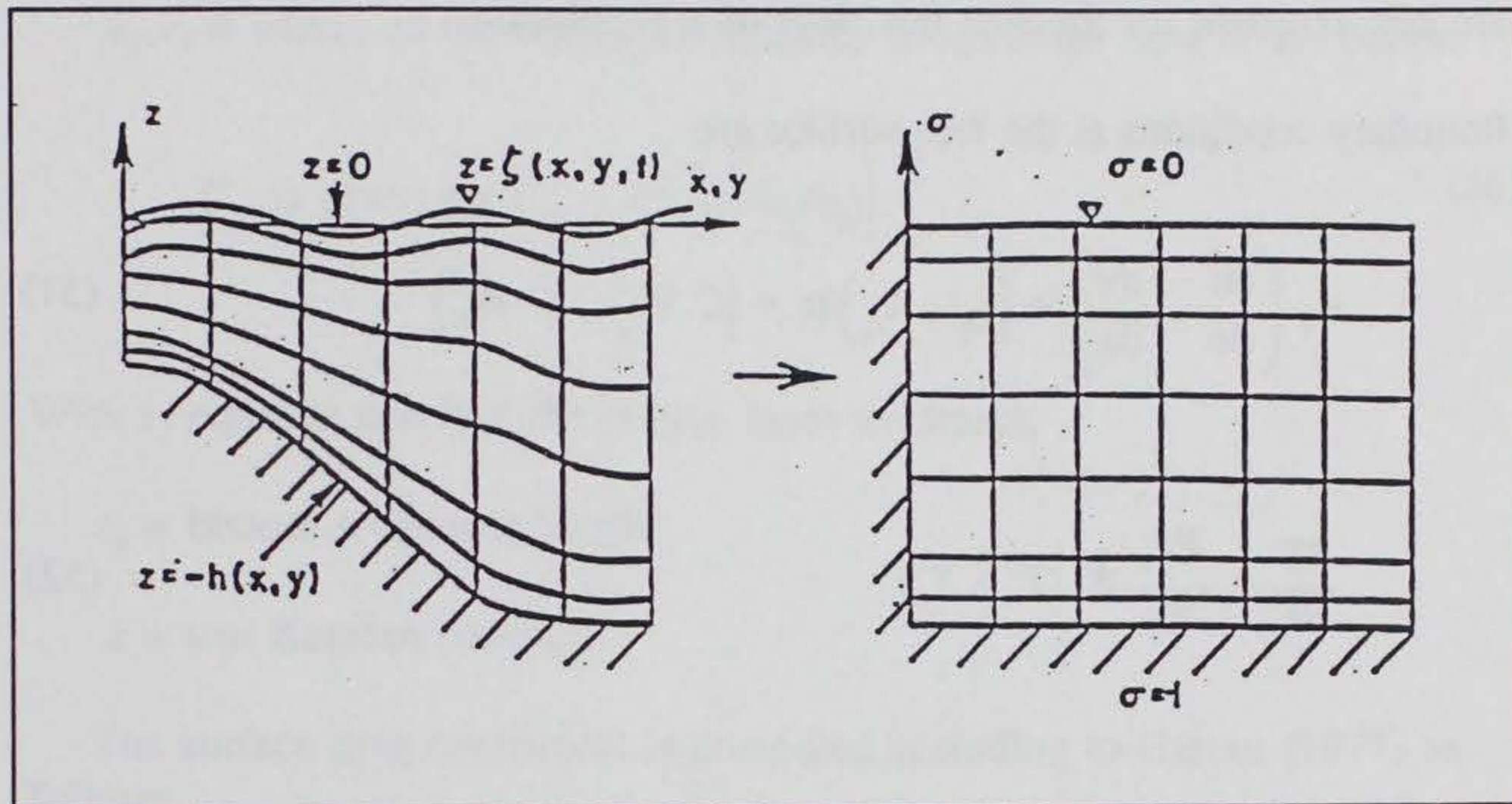
Boundary conditions at the free surface are

$$A_v \left(\frac{\partial \bar{u}}{\partial z} , \frac{\partial \bar{v}}{\partial z} \right) = \left(\tau_{s_\xi} , \tau_{s_\eta} \right) / \rho = \left(C\, W_\xi^2 , C\, W_\eta^2 \right) \tag{51}$$

$$\frac{\partial T}{\partial z} = \frac{Pr_v}{E_v}\, K\, (T - T_e) \tag{52}$$

$$\frac{\partial S}{\partial z} = 0 \tag{53}$$

where

C = surface drag coefficient

W = wind speed, meters per second

Boundary conditions at the bottom are

$$A_v \left(\frac{\partial \bar{u}}{\partial z} , \frac{\partial \bar{v}}{\partial z} \right) = \left(\tau_{b_\xi} , \tau_{b_\eta} \right) / \rho$$
$$= \frac{U_r}{A_{vr}}\, Z_r\, C_d \left(\bar{u}_1^2 + \bar{v}_1^2 \right)^{1/2} (\bar{u}_1, \bar{v}_1) \tag{54}$$

$$\frac{\partial T}{\partial z} , \frac{\partial S}{\partial z} = 0 \tag{55}$$

where

K = surface heat exchange coefficient

T_e = equilibrium temperature

C_d = bottom friction coefficient

$\bar{u}_1, \bar{v}_1$ = values of the horizontal velocity components next to the bottom

$$C_d \text{ is given by } C_d = k^2 \left[\ln \left(z_1/z_o \right) \right]^{-2} \tag{56}$$

With z_1 equal to one half the bottom layer thickness,

z_o = bottom roughness height

k = von Karman constant

The surface drag coefficient is computed according to Garratt (1977) as follows

$$C = (0.75 + 0.067 \ W) \ \text{x} \ 10^{-3} \tag{57}$$

with the maximum allowable value being 0.003. The surface heat exchange coefficient K and the equilibrium temperature T_e are computed from meteorological data (wind speed, cloud cover, wet and dry bulb air temperatures, and relative humidity) as discussed by Edinger, Brady, and Geyer (1974).

Three stations were used to collect prototype velocity measurements during the July 27-August 4, 1993, field experiment. They are: stations CM1 (inside the harbor) and CM2 (at the entrance) for current velocity, and gauge TG1 (at the entrance) for surface height, as shown in Figure 6. Figure 7 shows tidal elevation data during the period which have strong semidiurnal and diurnal signals ranging from 2 to 2.5 ft. Recorded three times a day, the wind data obtained at 0000, 0600, and 1800 daily are the actual Maalaea Harbor wind data telemetered to the Kahului Airport. Figure 8 shows wind speed and direction data during the experiment period. For the first 3 days, the wind is from the northeast with speeds ranging between 5 and 20 knots. For the rest of the experiment period, the wind is predominantly from the north with speeds ranging from 2 and 25 knots. During the period July 28-30, wind data were estimated from nearby weather stations due to the malfunction of the transmitter at the Maalaea weather station.
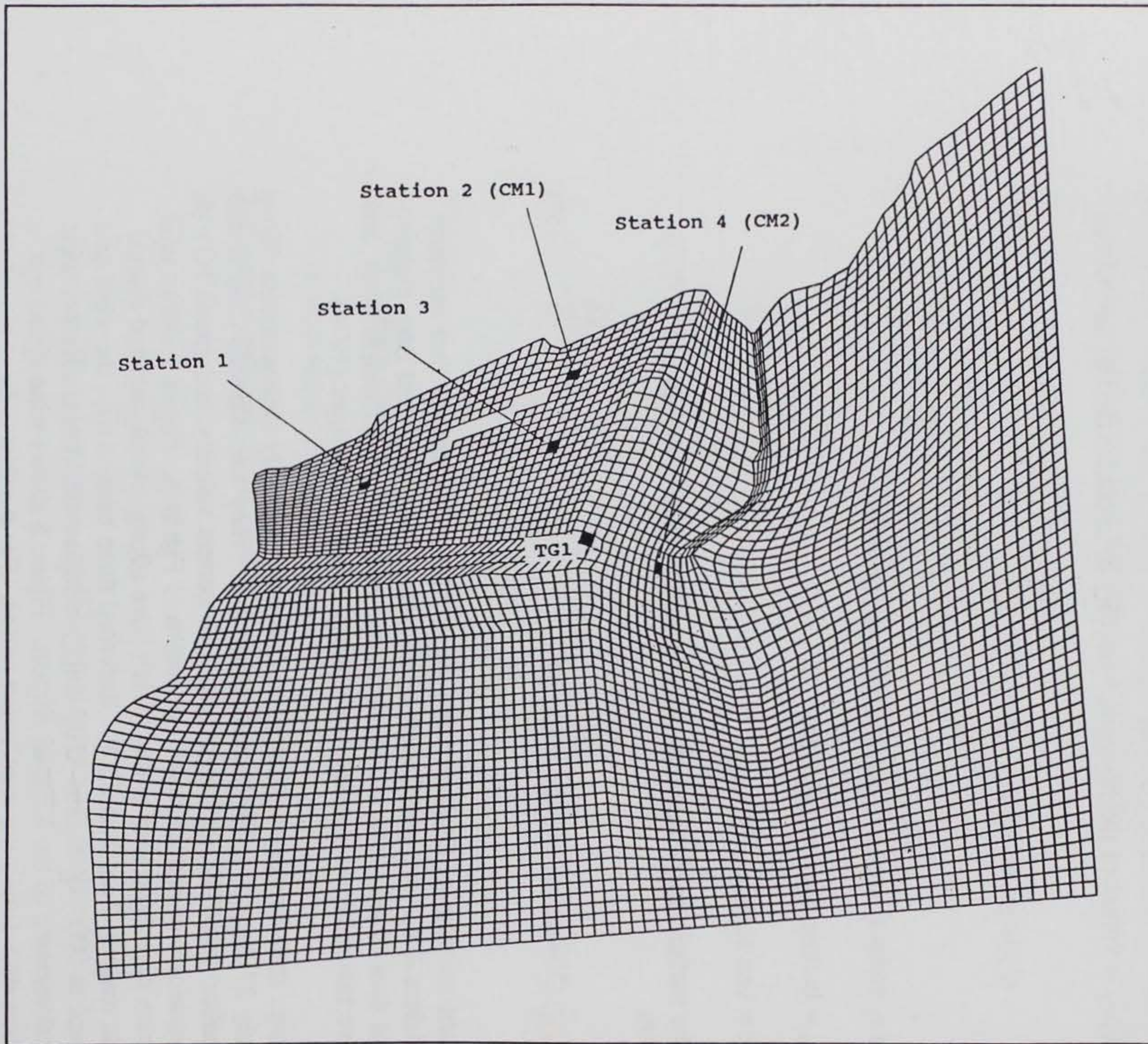
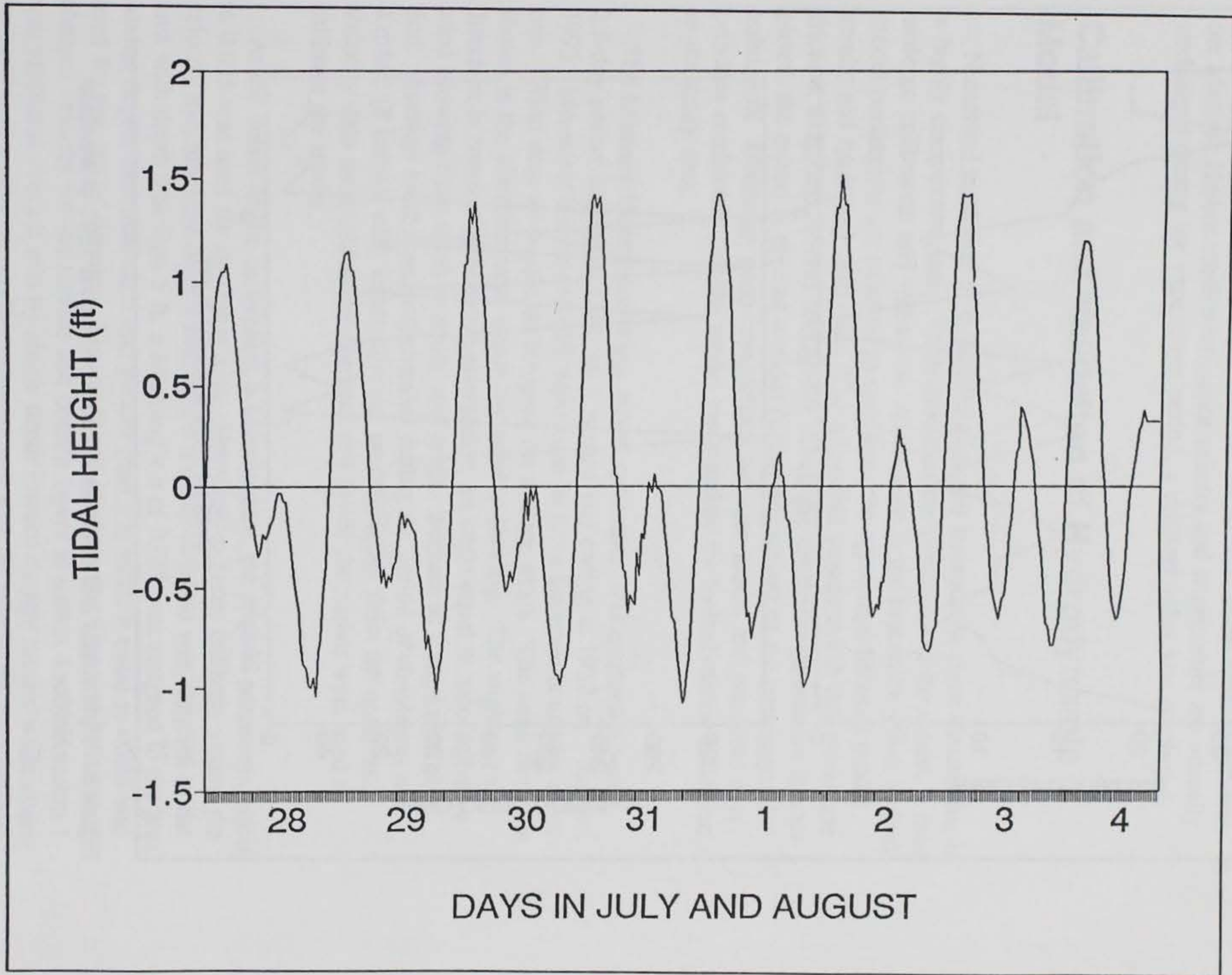Figure 6. Current meter, tidal gauge locations and stations for model output

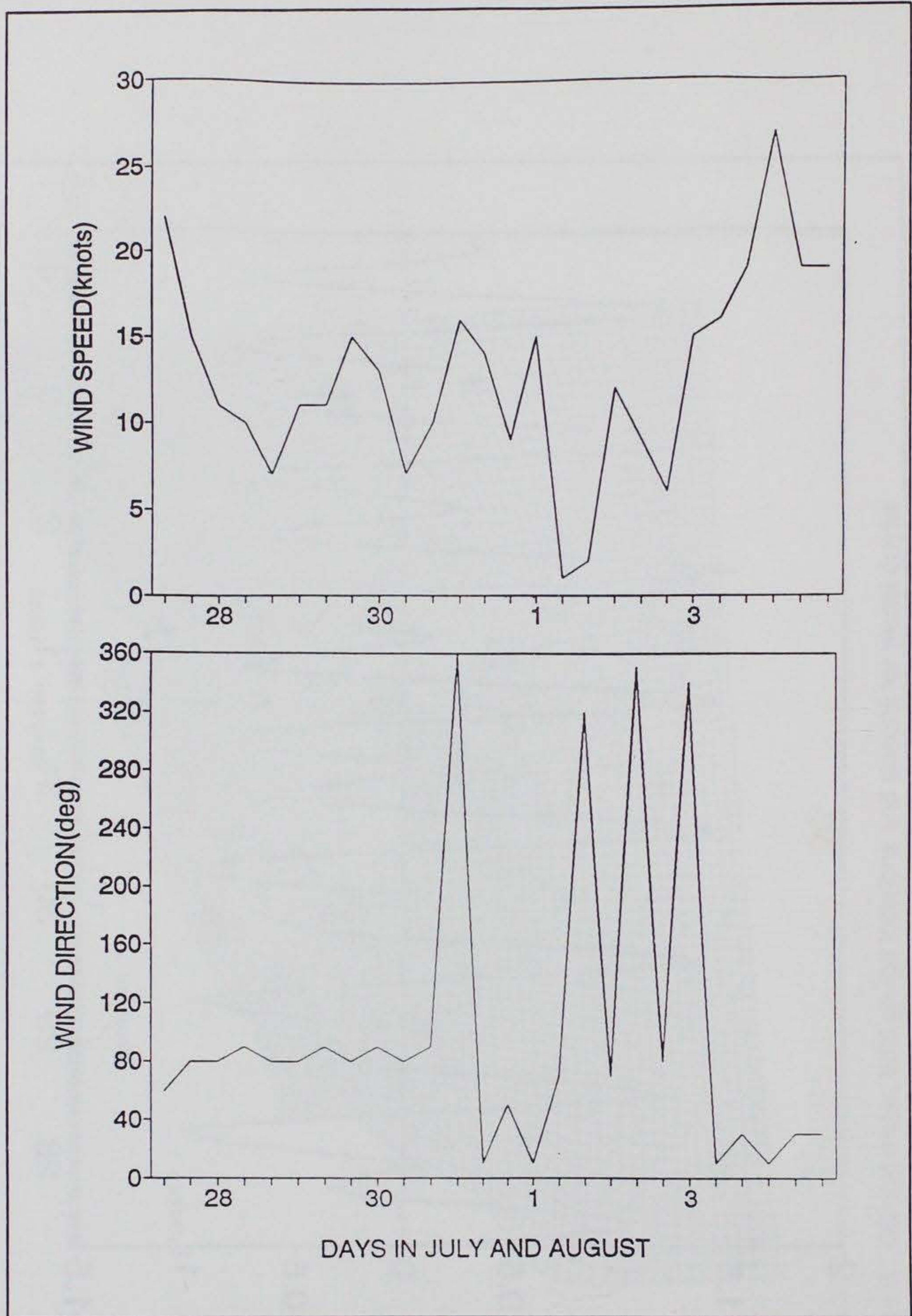Figure 7.   Tidal gauge data, 27 July - 4 August 1993

Figure 8. Wind speed and direction, 27 July - 4 August 1993 at Maalaea
Harbor

At the ocean boundary, the water-surface elevation is prescribed along with time-varying vertical distributions of salinity and temperature. Specified values of salinity and temperature are employed during flood flow, whereas during the ebb, interior values are advected out of the grid. Normal velocity, viscosity, and diffusivity components are set to zero along solid boundaries. In the Maalaea Harbor application, since salinity and temperature are virtually unchanged during the experiment period, a constant value was employed.

Calibration and Validation of Hydrodynamic Model

Numerical modeling of hydrodynamics and transport in three dimensions is a highly complicated task. To demonstrate the capability of the model, it must undergo calibration and validation. Calibration is the procedure where certain model parameters are adjusted to maximize the agreement between model results and measured field data. The adjustable parameters in this model are friction, drag, and mixing coefficient. Once the calibration procedure is completed, the model is applied without further adjustment of the parameters for validation. Obtaining good comparisons between model and measured data provides confidence that the model can simulate the hydrodynamic condition in the study area.

The Maalaea Harbor numerical model calibration was conducted over a 2.5-day period starting at 0800 on 1 August and ending at 1930 on 3 August, 1993. Measured tidal elevations were used to drive the open boundary condition. Wind data were used to compute the surface stress. The wind direction shown is the direction from which the wind is blowing. The angle of the direction is based on true north convention; an angle equal to zero defines a wind blowing from north to south, and angles increase in a clockwise direction. Average wind speed experienced during the period of simulation was 4 m/sec (8 knots), with winds blowing predominantly from the northeast. Velocity data measured at the entrance and inside the harbor were used to calibrate the model.

At the outset of the calibration, a Manning's n, the friction parameter, equal to 0.035 was used for the entire area. However, to better calibrate against the velocity measurement data, a Manning's n equal to 0.040 was assigned to the area with depth less than 5 ft, a Manning's n of 0.037 was assigned to the area having depths less than 10 ft and greater than 5 ft while n equal to 0.035 was used for the rest of the area. Figures 9 and 10 show the final comparisons of channel velocity for the surface and bottom layers at station 4. Observation 1 was measured every 2 min by single depth Endeco current meters while observation 2 was a velocity profiler measurement with 30 min as the time interval. A good agreement between modeled and measured velocity was obtained for both data sets. Notable exceptions occurred during brief periods, such as at hours 15, 19, and 22, where the model underpredicts the surface current
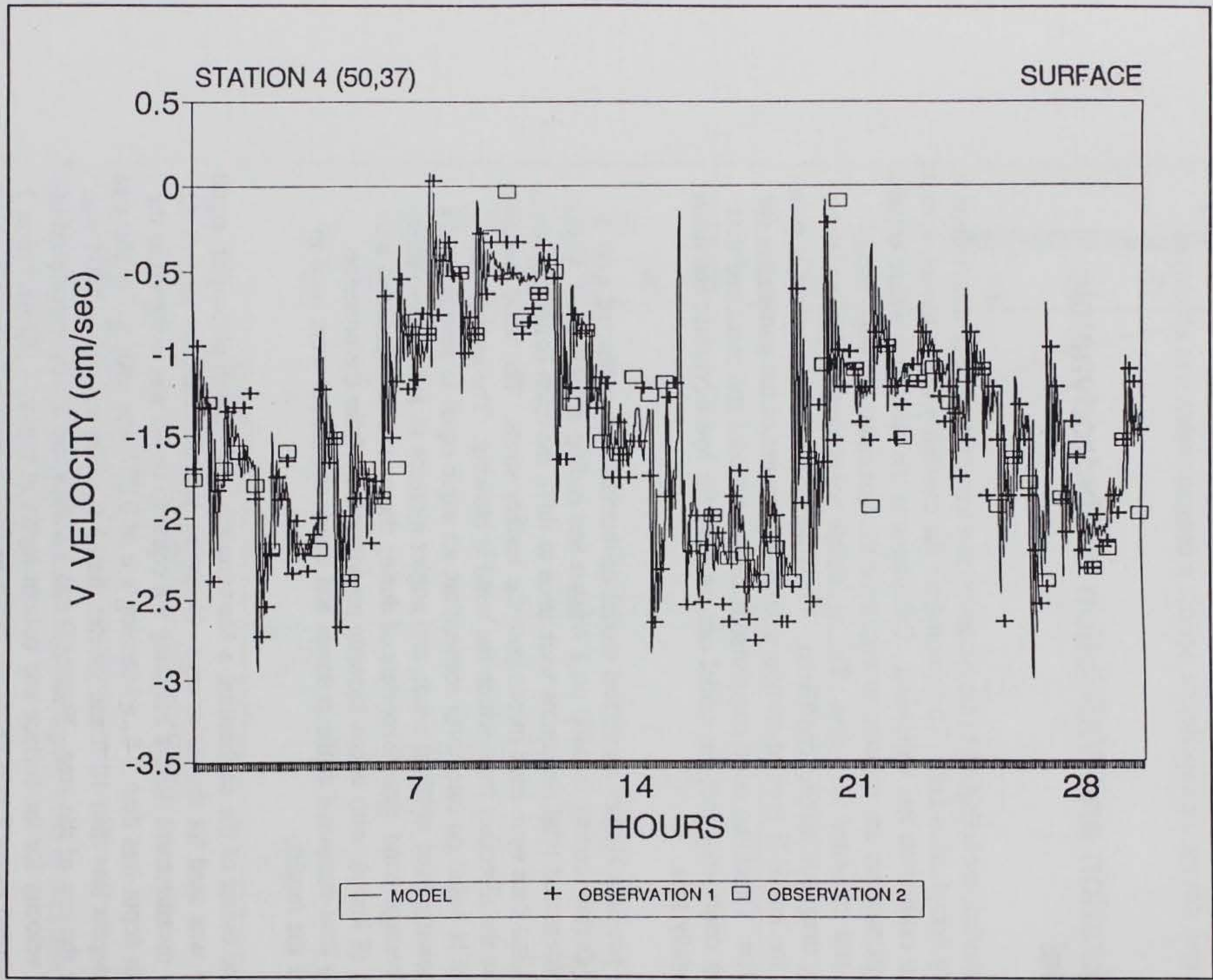
Figure 9. Numerical model calibration: model and data comparison for surface layer at station 4,
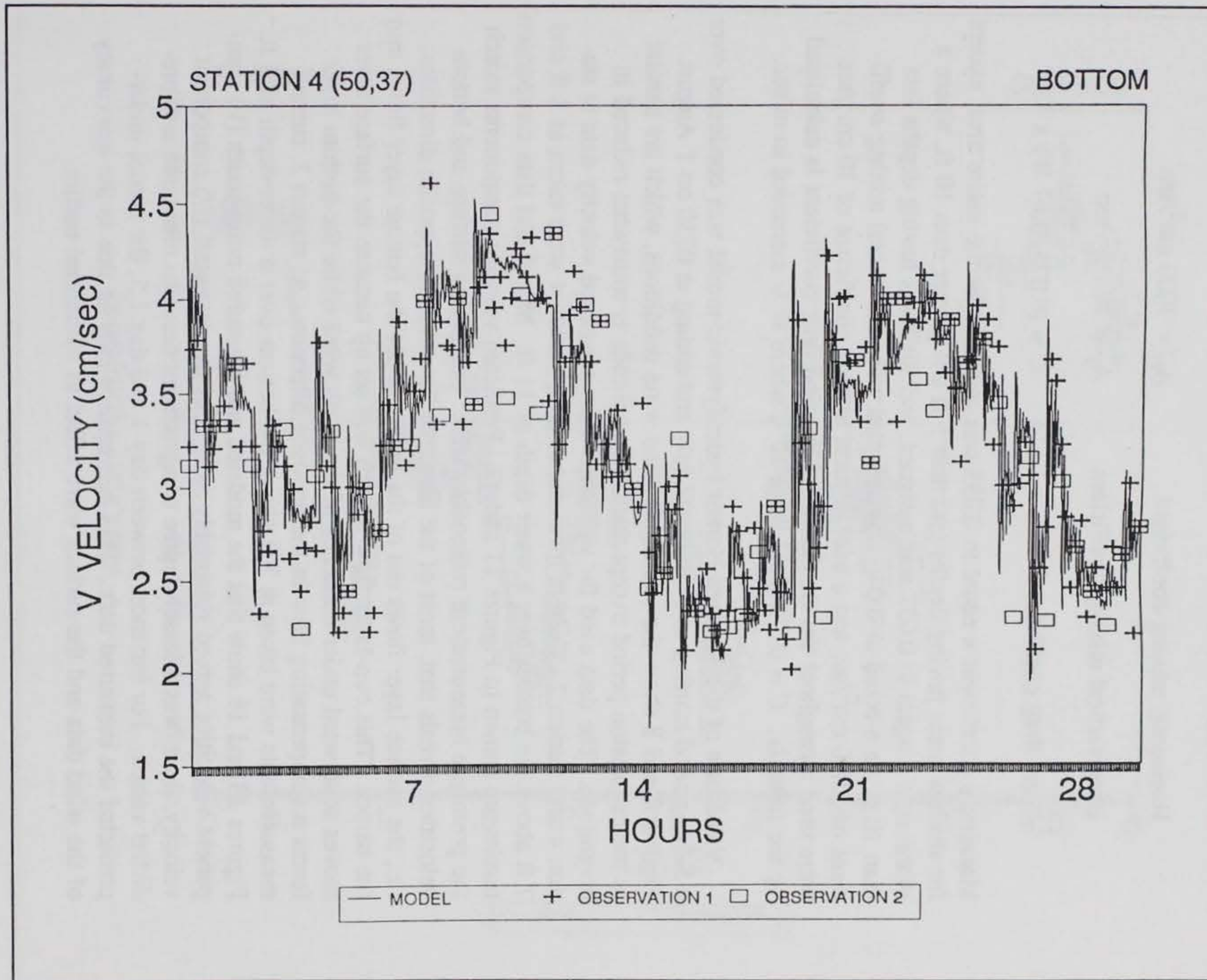1 August - 3 August 1993

Figure 10. Numerical model calibration: model and data comparison for bottom layer at station 4,
1 August - 3 August 1993

speed. It appears that during periods of high wind, wind-generated waves can degrade the accuracy of the Endeco current meter readings.

The final set of model coefficients thus determined is as follows:

Manning's coefficient	$n = 0.035\text{-}0.040$
Horizontal mixing coefficient	$A_H = 1000 \text{ cm}^2/\text{sec}$
Base vertical mixing coefficient	$A_V = 10 \text{ cm}^2/\text{sec}$
Wind drag coefficient	$C = (0.075 + 0.67 \ W) \times 10^{-3}$

Manning's coefficient n equal to 0.035 was assigned for the entire area, except for shallow areas having depths less than 5 ft but greater than 10 ft, where a Manning's n equal to 0.037 was assigned, and for areas having depths less than 10 ft, an n equal to 0.040 was assigned. The horizontal mixing coefficient of 1,000 cm^2/sec and a base vertical mixing coefficient of 10 cm^2/sec were used throughout the simulation. The wind drag coefficient is calculated by the formula: $C = (0.75 + 0.67 \ W) \times 10^{-3}$, where W is measured in m/sec.

Validation of the Maalaea Harbor hydrodynamic model was conducted over a 5-day period starting at 0730 on 27 July and ending at 0730 on 1 August. Figures 7 and 8 show the overall tide and wind conditions, which are similar to the calibration period except that tide amplitude is somewhat reduced in magnitude. The data used for validation were measured velocity data at station 4 and station 2. Current measurements at station 4 were taken at 3 ft and 7 ft above the bottom over a water depth of 11 ft. Model and data comparison results are shown in Figures 11 and 12. Predicted velocity components match the prototype measurement reasonably well. Comparing surface and bottom velocities reveals that, most of the time, the flows are in opposite directions; i.e., the surface layer flows out of the harbor while the bottom layer flows into the harbor. This two-layer flow pattern was set up because the surface layer moves southward under influence of the north wind while the bottom layer forms a compensating flow in the opposite direction. At station 2, current measurements were taken at 3 ft above the bottom over a water depth of 8 ft. Figures 13 and 14 show that the modeled and measured north-south (V) component velocities agreed reasonably well. For the east-west (U) component velocity, there was a lesser degree of agreement between measured and predicted values. For instance, between day 1 and day 1.5, the model under-predicted the measured data. This discrepancy may be due to the inaccuracy of the wind data and the surface wave effect as mentioned earlier.

Figure 11. Numerical model validation: model and data comparison for surface layer at station 4, 27 July - 1 August 1993
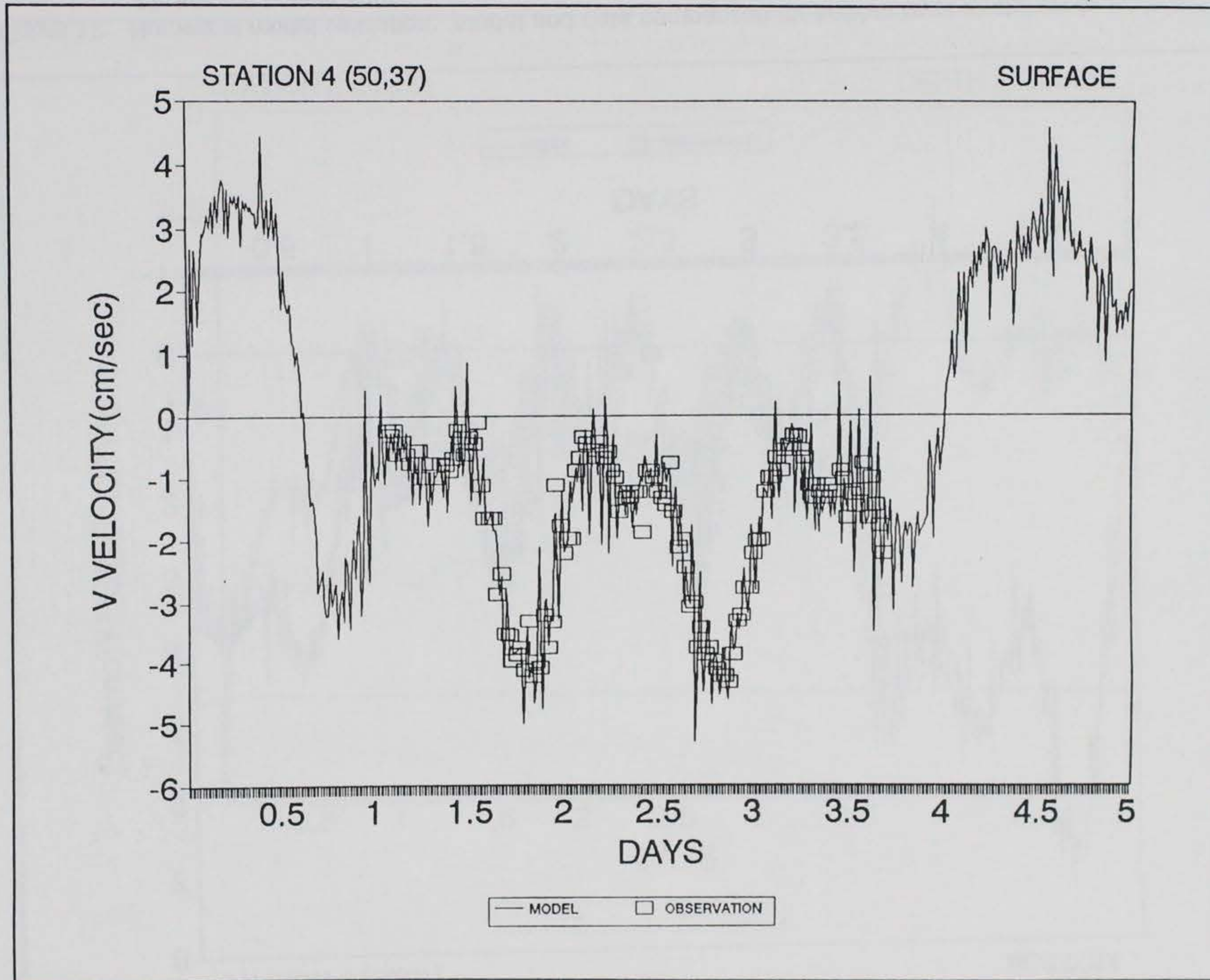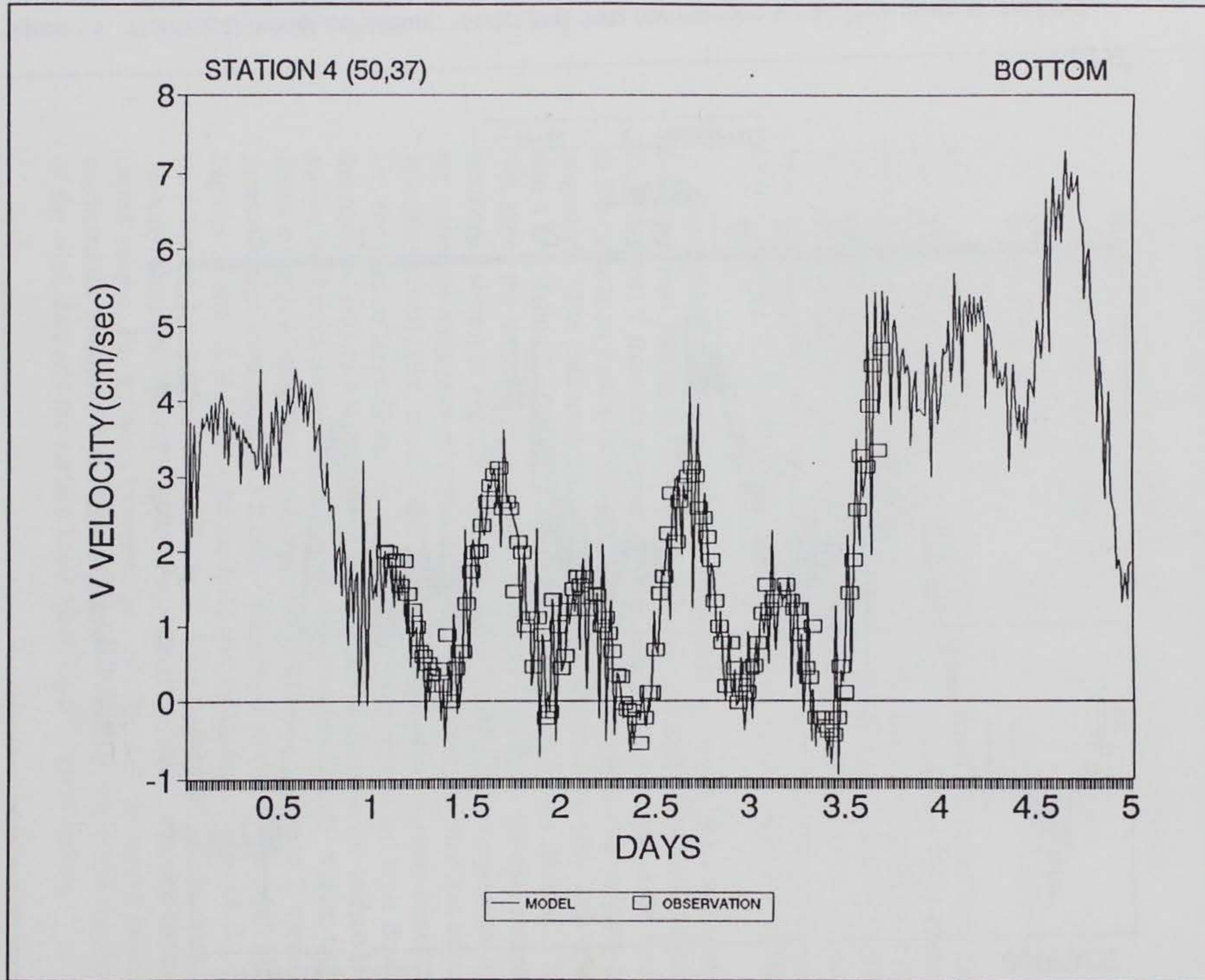
Figure 12. Numerical model validation: model and data comparison for bottom layer at station 4, 27 July - 1 August 1993
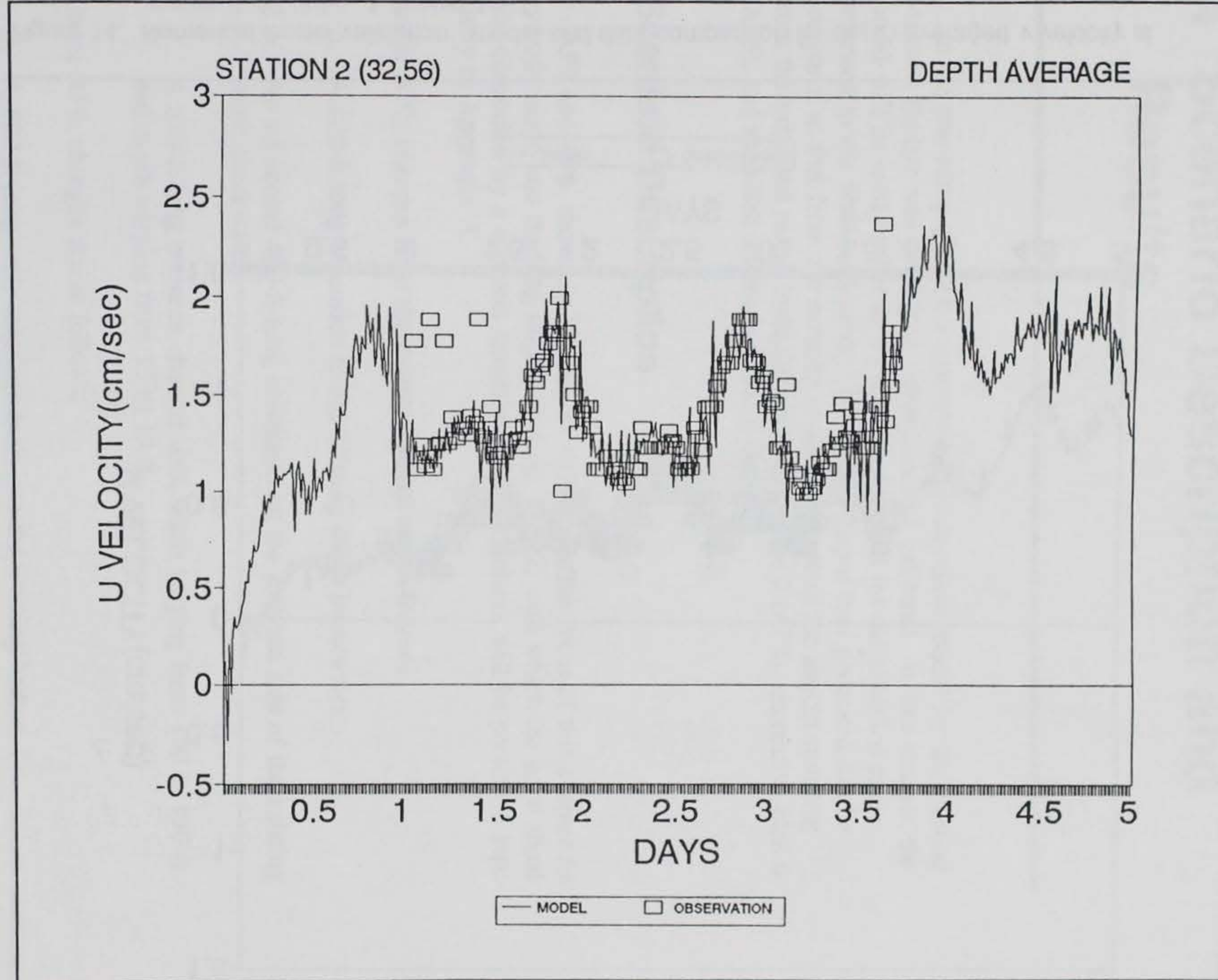
Figure 13. Numerical model validation: model and data comparison for depth-averaged *u* velocity at station 2, 27 July - 1 August 1993
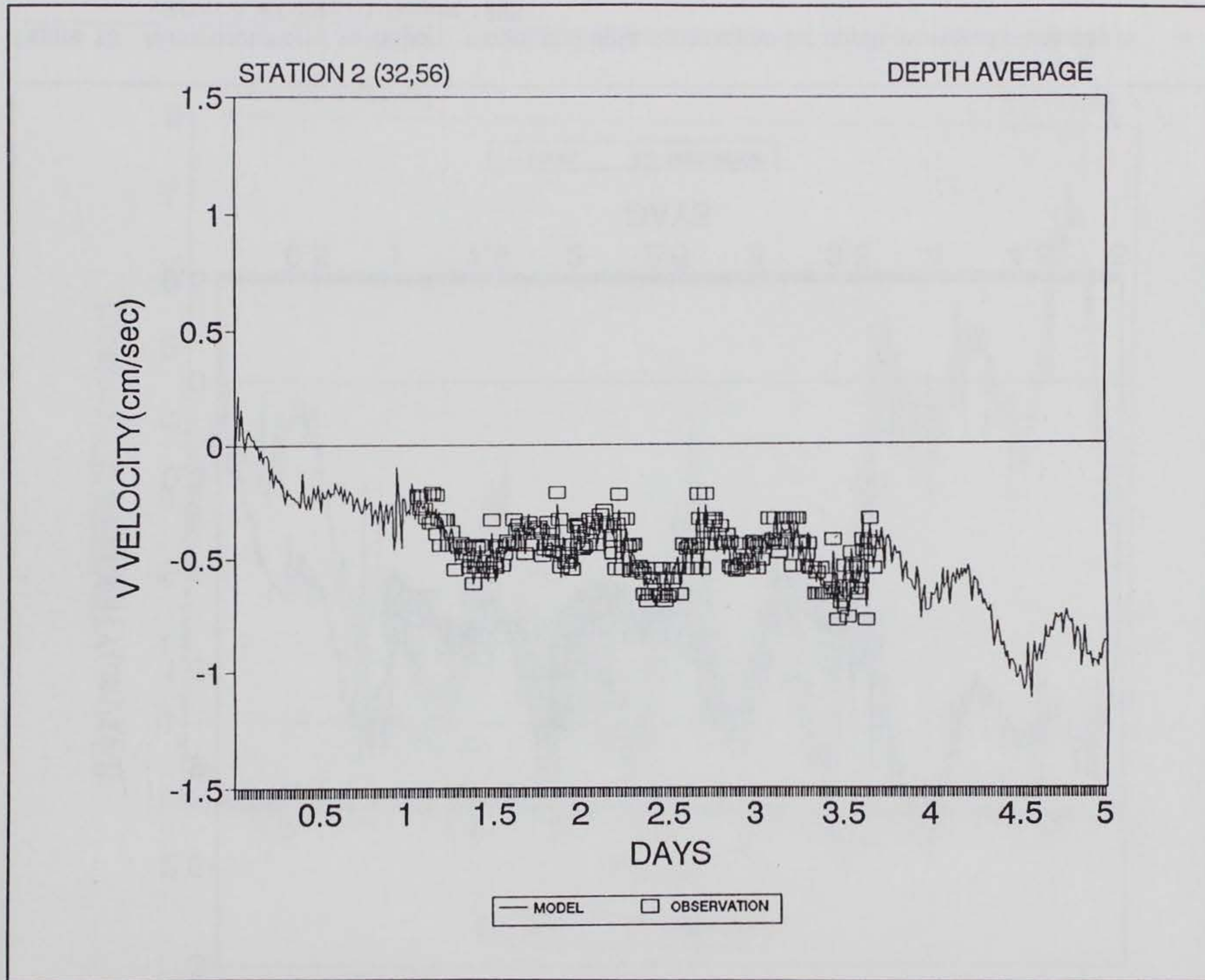
Figure 14. Numerical model validation: model and data comparison for depth-averaged *v* velocity at station 2, 27 July - 1 August 1993

4 Scenario Description and Results

In the preceding chapter, a numerical hydrodynamic model for the existing Maalaea Harbor was developed, calibrated, and validated. In this chapter, the model will be used further as a project design tool for the modified plans proposed in the Maalaea Harbor. The model output thus generated can be compared to that from the existing condition to assess the impact resulting from the proposed plans, including alternative plan 2 (AP2), alternative plan 6 (AP6), and modified alternative plan 2 (MAP2).

Scenario Description

AP2 and AP6, shown in Figures 15 and 16, are the focus of this chapter for hydrodynamic and flushing impact studies. MAP2, with which the coral shoal was connected by a concrete causeway to the mainland, will be presented separately in Appendix A.

Under AP2, changes from the existing harbor are as follows:

a. A 620-ft-long extension to the existing south breakwater.

b. An additional 400-ft-long revetment on the seaward side of the existing south breakwater.

c. A 610-ft-long entrance channel with width varying from 150 to 180 ft and depth varying from 12 to 15 ft.

Under AP6, changes are as follows:

a. A 600-ft-long mole structure built into the existing harbor.

b. An additional berth facility built on the inward side of the mole.

c. Removal of a submerged coral reef in the existing harbor to provide more berth space for the existing south breakwater.
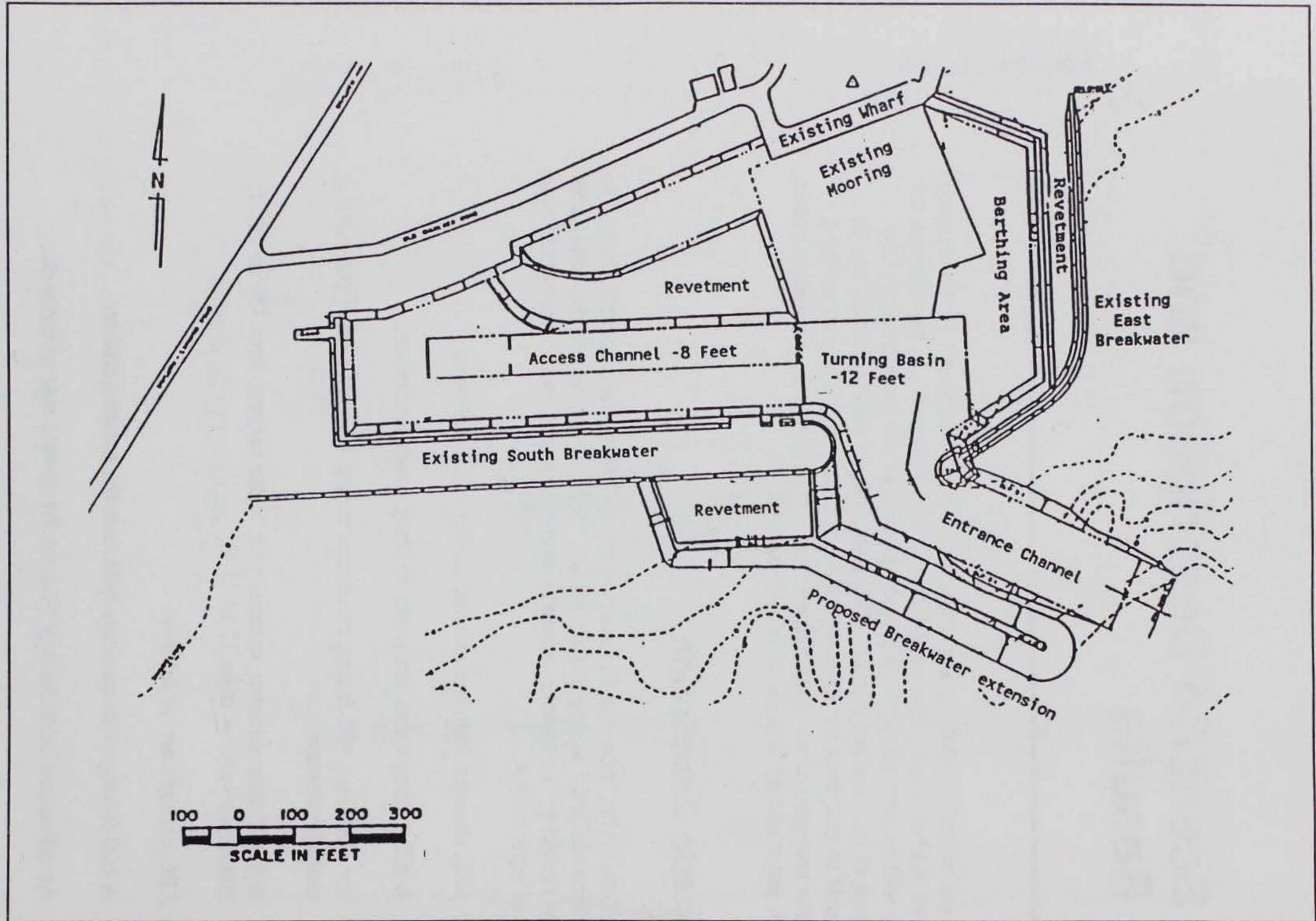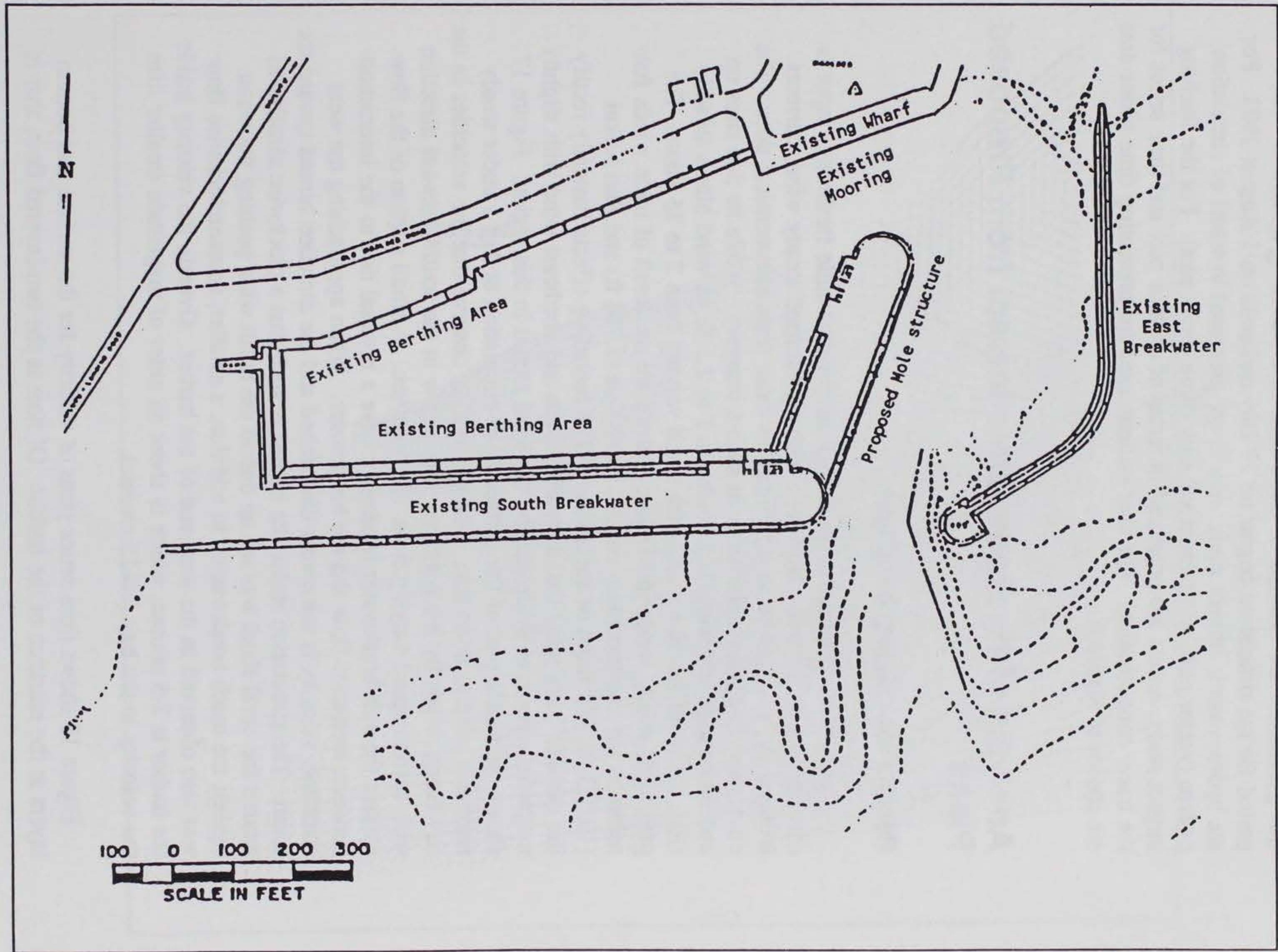
Figure 15. AP2

Figure 16. AP6

For scenario runs with the proposed plans, most of the input files stay the same, except the grid and topographic files, which are modified to reflect the new configurations. The forcing functions such as tide and wind, and calibration parameters are identical to those used in the existing condition. The period for the simulation begins on 27 July and ends on 1 August 1993. For the hydrodynamic impact study, results are presented in terms of circulation pattern (vector plot) and current velocity (time series plot). For the flushing impact study, results are presented in terms of contour plot and time series for the tracer concentration. The four stations used for presenting time series data are shown in Figure 6.

Analysis of Hydrodynamic Impact from Proposed Plans

Results for existing condition

In general, the circulation in a small harbor with little freshwater input is often driven by the tide. However, with a prolonged steady wind, currents induced by wind can be as significant as those from astronomical tides. The circulation in Maalaea Harbor is in such a category. While its tide rises up and down regularly with range between 2 to 2.5 ft, its wind blows steadily from the north and northeast, with speed varying from 2 to 25 knots. The prolonged steady winds in Maalaea Harbor are the result of trade winds funneled by the two mountain ranges, Puu Lalua (5,788 ft) and Puu Kukui (10,023 ft), just north of the harbor.[1] The funneling effects basically rectify the variable trade wind into a steadier north and northeast wind with slightly magnified speed, as evidenced by the wind record in this region. Figure 17 shows the vector plot of the surface layer circulation at day 3 under steady northeast wind at flood tide. One can readily observe that the velocities in the bay being driven by the northeast winds flow in the southwestward direction with current speed varying from 10-15 cm/sec. A small portion of the flow outside the east breakwater appears to have a reversal due to the interaction between westward flow and the breakwater. When approaching the west coastline, velocity is somewhat diminished and the direction turned toward the south. The circulation inside the harbor is such that a clockwise circulation around the coral shoal was set up due to the north wind pushing the water against the south breakwater. In addition, a smaller, counterclockwise flow was also observed in the west end of the harbor. Overall, the velocity inside the harbor is 2-5 cm/sec, which is about an order of magnitude smaller than the velocity in the bay (10-15 cm/sec).

Figure 18 shows time series plots of velocity for the surface and bottom layers at the entrance of the harbor. Of note is the two-layered flow, that is

---

[1] Personal Communication, 1994, H. Nakashima, U.S. Army Engineer Division, Pacific Ocean, Ft. Shafter, HI.
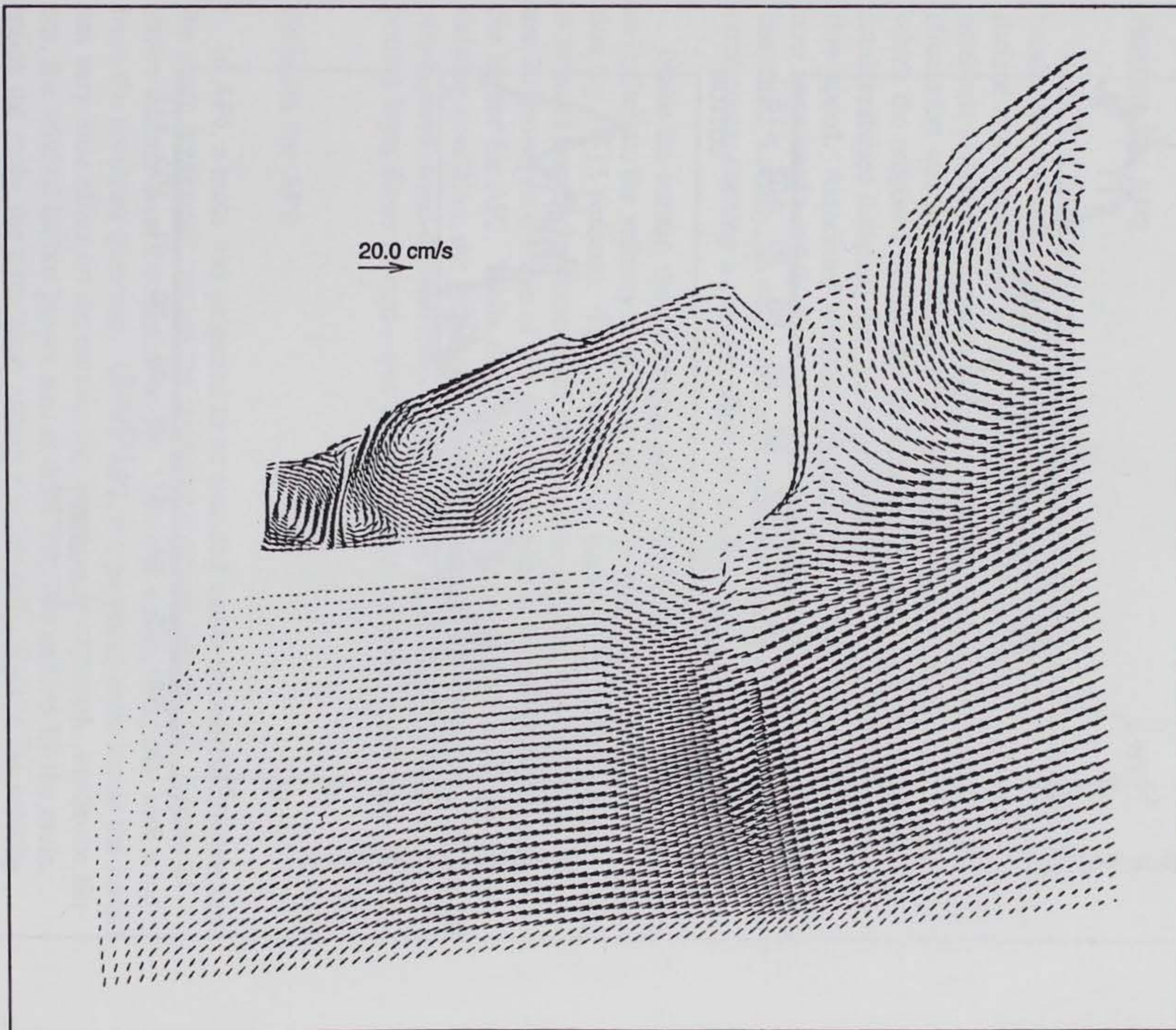
Figure 17. Vector plot of surface layer circulation at day 3 (0730, 30 July 1993) for the existing condition
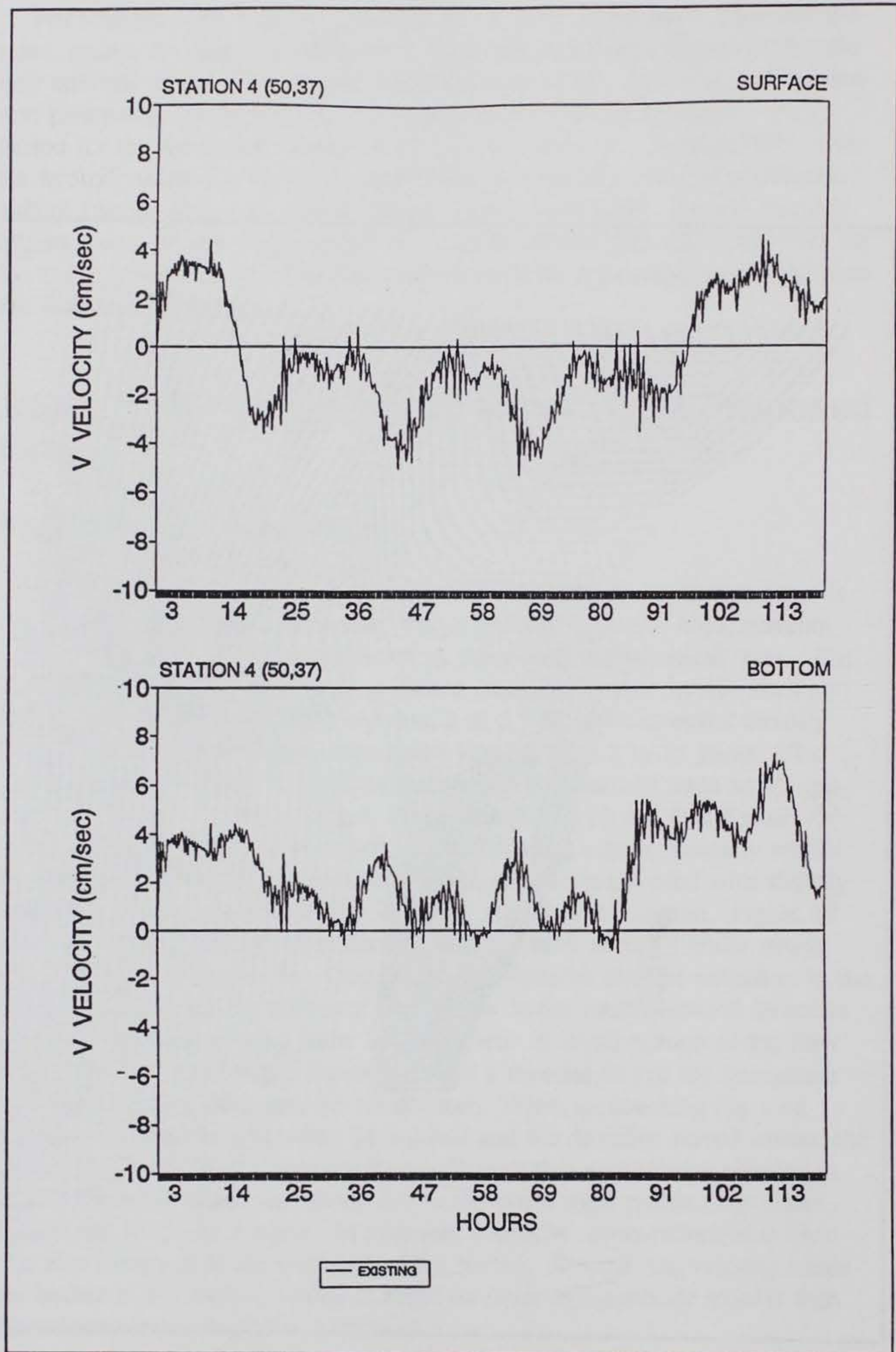
Figure 18. Time series of surface and bottom channel velocity at the entrance of the harbor for the existing condition

the opposite velocity direction on the surface and at the bottom, set up by the near steady wind from the north. It becomes obvious that superimposed on the regular astronomical tide, there is a significant vertical shear, set up by a prolonged north wind. This steady, wind-driven, two-layer circulation is what makes the dynamics of Maalaea Harbor circulation unique from the other small harbors, in which tidal force is the dominant force.

Results for AP2

In AP2, a breakwater was proposed to extend from the existing south breakwater toward the southeast direction (Figure 15). Figure 19 presents the surface layer circulation at day 3 when it was at flood tide with wind from the northeast direction. A noticeable effect of the proposed breakwater on the bay circulation was seen to occur at the south side of the new harbor entrance, in which the proposed breakwater deflects the incoming flow from its original southwestward direction into a straight southward direction with accelerating flow speed. Associated with the deflection, the original southwestward flow now turns northward in the area between the proposed breakwater and the west coastline. Locally, an eddy was generated around the tip of the proposed breakwater, exerting a circular effect on the flow around the harbor mouth.

Inside the harbor, the circulation pattern is similar to the existing condition; nevertheless, the velocity magnitude is smaller compared to the existing condition (by 10-15 percent). The exchange rate between the harbor and bay water is reduced due to the decrease of the available area for free exchange. Figure 20 shows time series of the surface and bottom velocity at the entrance of the harbor for AP2. While the variation of velocity pattern is similar to the existing condition, the velocity magnitude is smaller by 10 percent. Again, the two-layered, wind-driven flow—that is, surface layer flows outward while bottom layer flows inward—was seen to persist under the north wind.

Results for AP6

In AP6, a mole was proposed to be installed inside the existing harbor from the south breakwater toward the northeast direction (Figure 16). Figure 21 shows surface layer circulation at day 3 when it was at flood tide with wind from the northeast direction. Unlike AP2, the proposed mole inside the harbor has very little effect on the outside bay water, as is expected. Inside the harbor, the original harbor proper was divided into two regions by the mole. Inside the mole, the circulation pattern changes only slightly; the velocity magnitude is similar to the existing condition. Outside the mole, however, the channel velocity at the harbor entrance was reduced dramatically and has one of the smallest values among all conditions, as shown in Figure 22. Comparing time series for all three conditions (i.e., existing, AP2, and AP6) indicated that velocity for AP6 was only 30 to 40 percent that of the existing condition (a drop of 60-70 percent), as indicated in Figures 23-24. This is a significant reduction of the velocity at the harbor entrance and hence can have profound
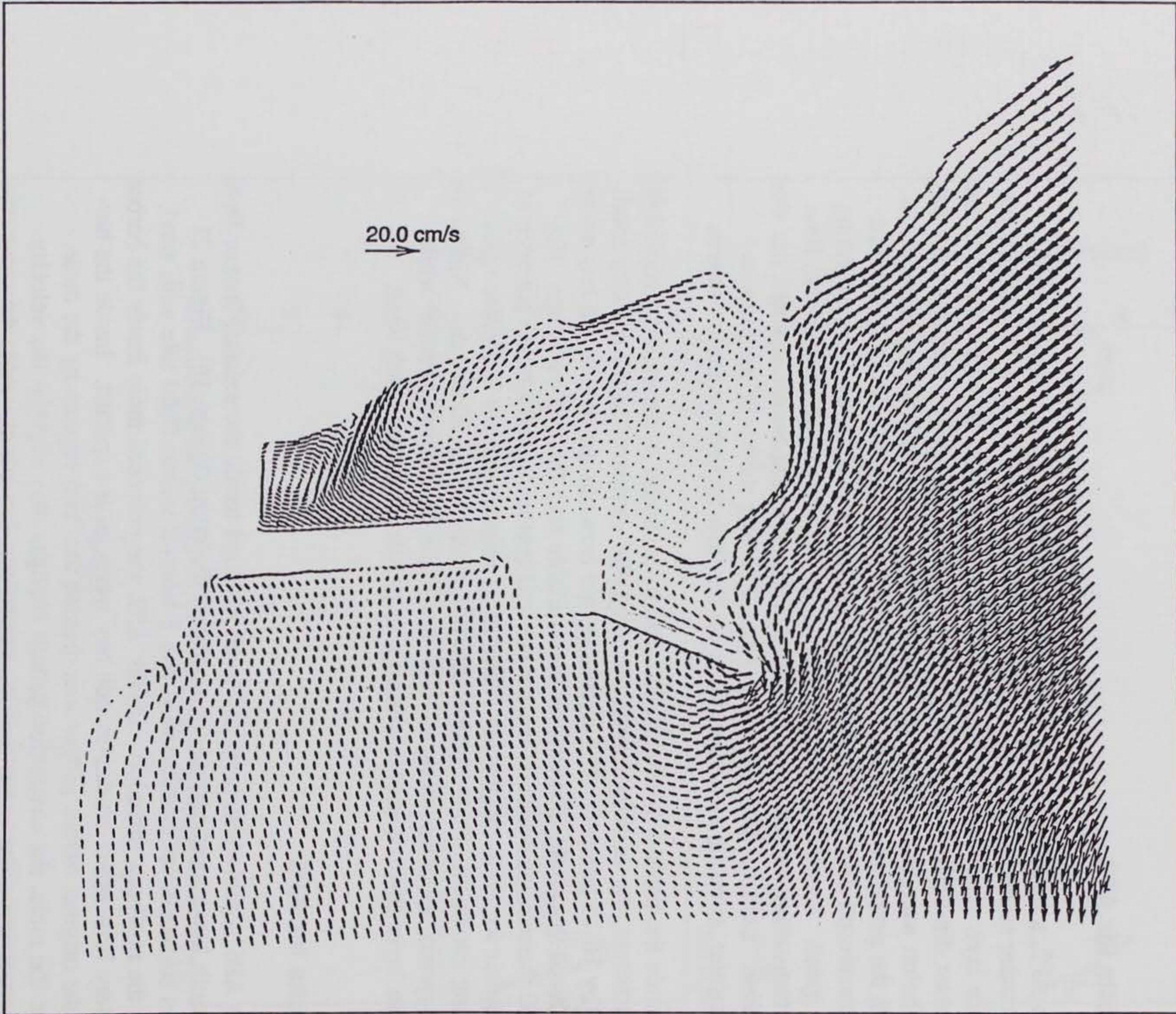
Figure 19. Vector plot of surface layer circulation at day 3 (0730, 30 July 1993) for AP2
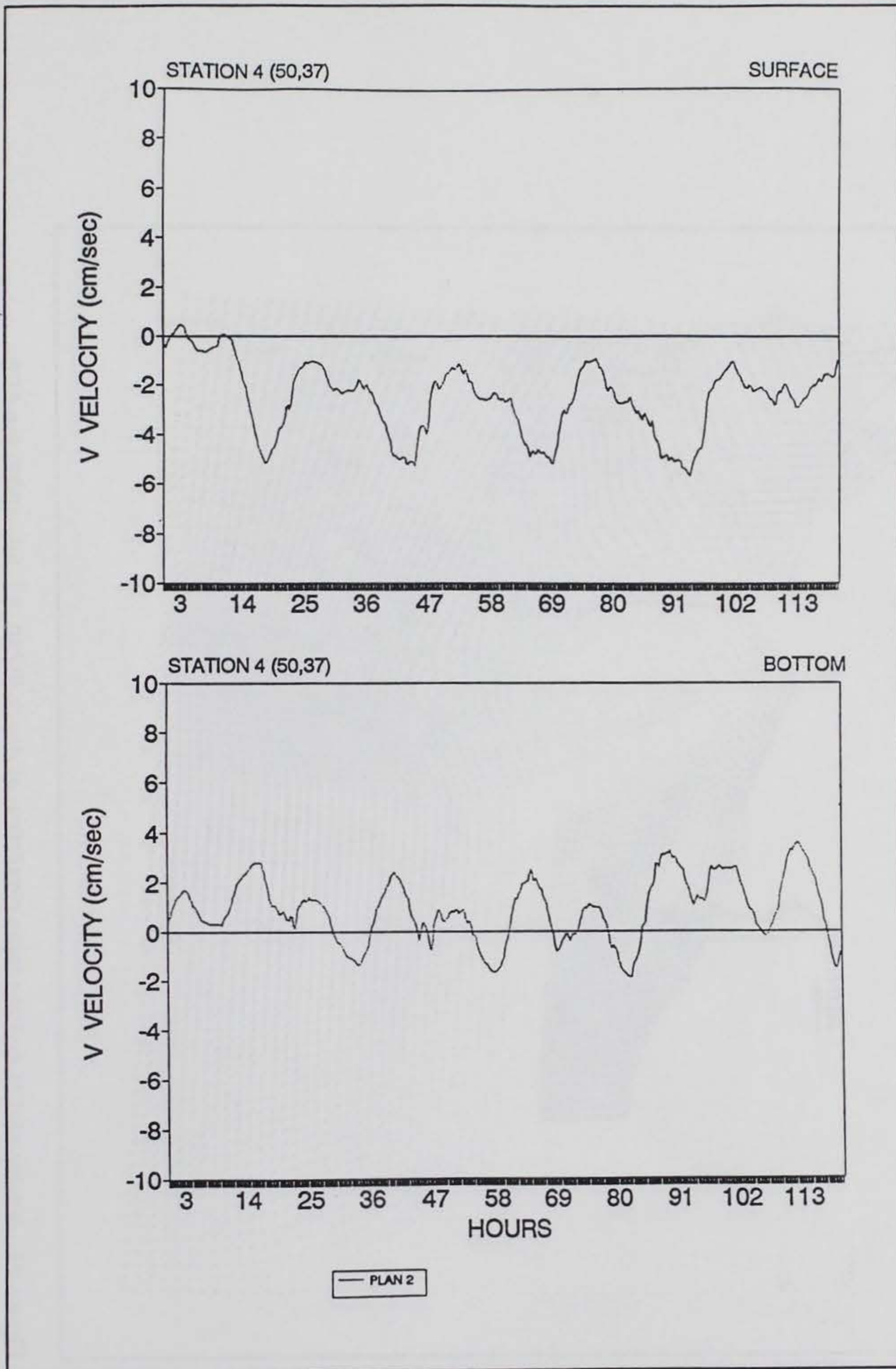
Figure 20. Time series of surface and bottom channel velocity at the
entrance of the harbor for AP2

Figure 21. Vector plot of surface layer circulation at day 3 (0730, 30 July 1993) for AP6
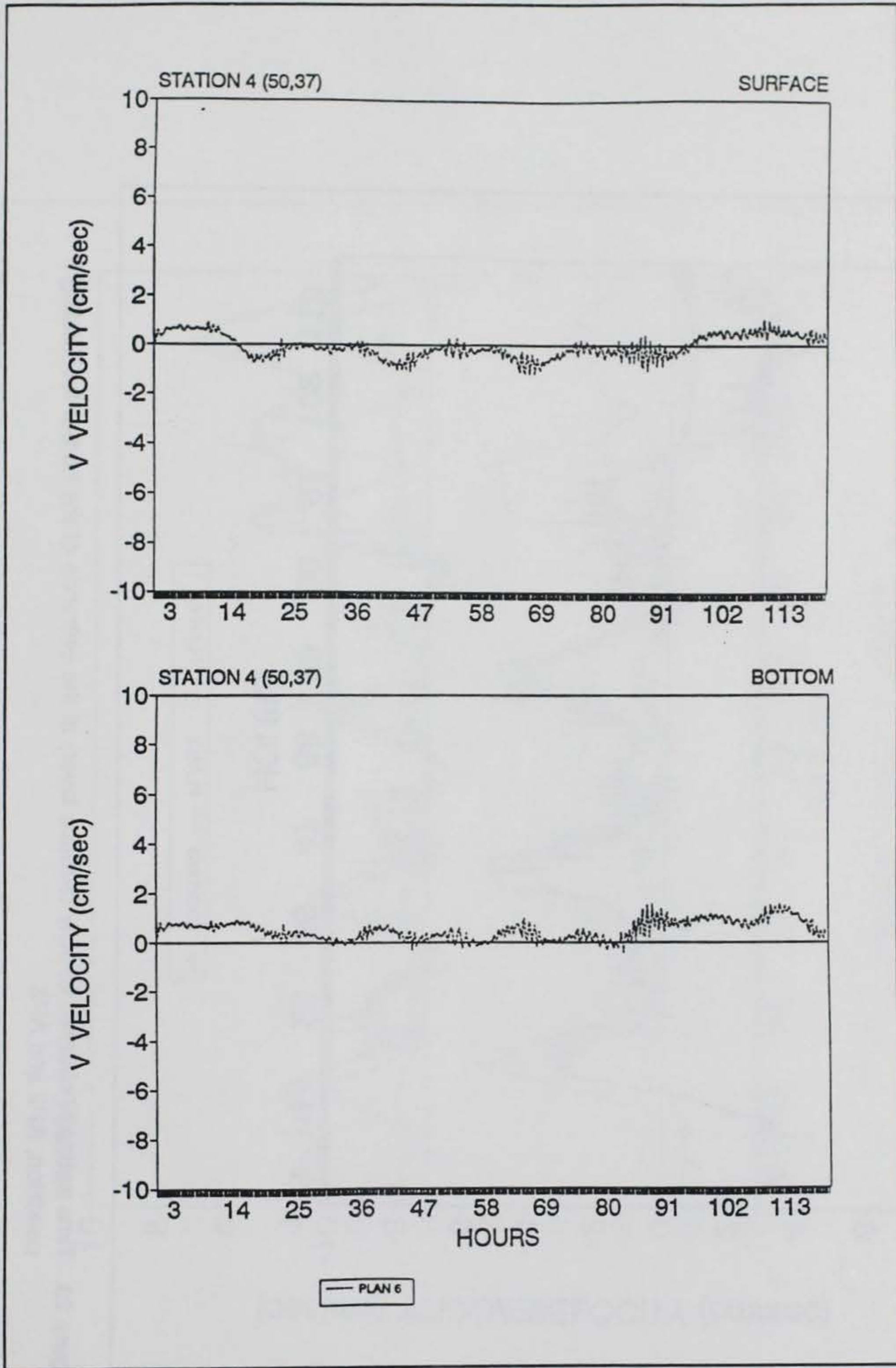
Figure 22. Time series of surface and bottom channel velocity at the entrance of the harbor for AP6
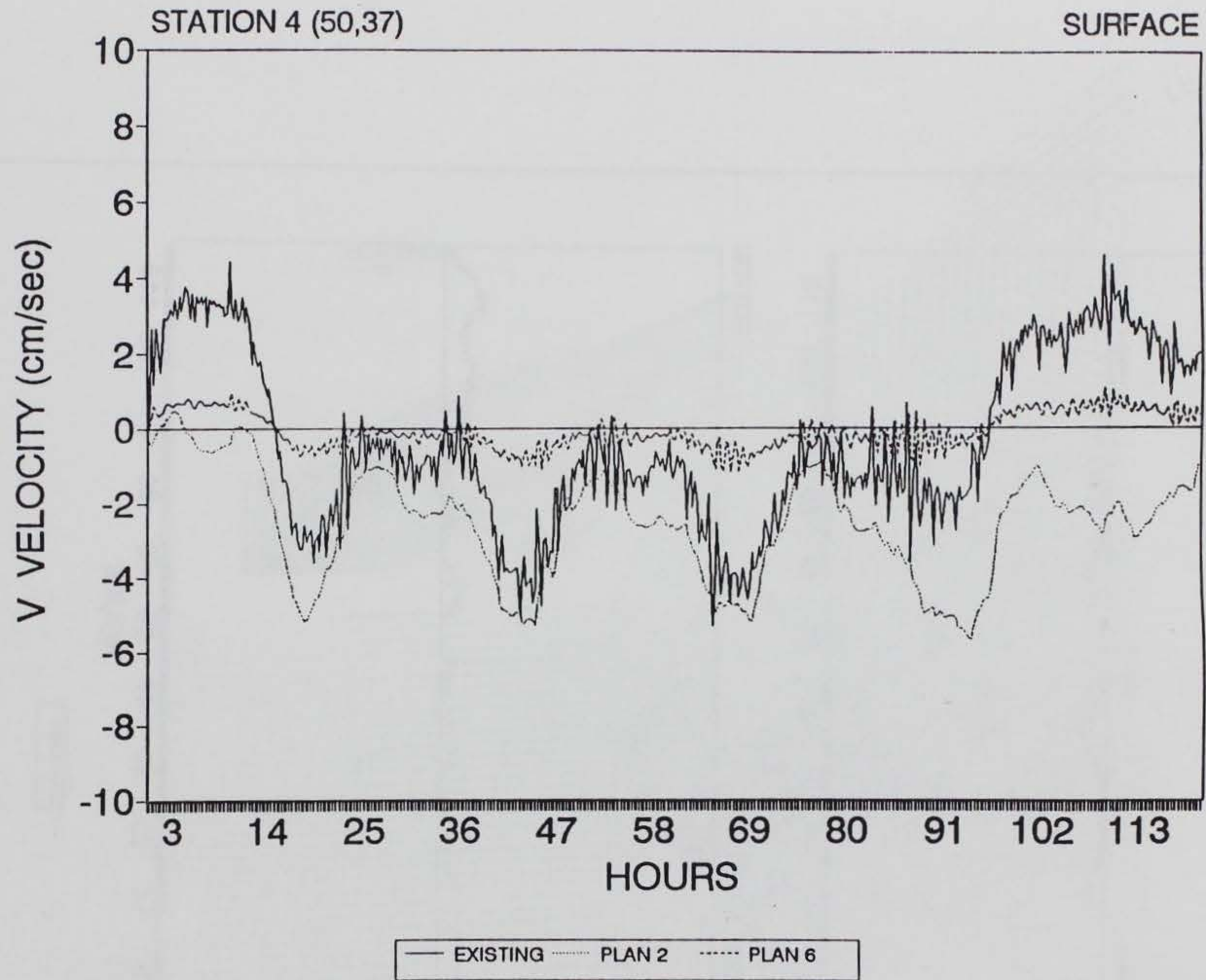
Figure 23. Time series of channel velocity (surface layer) at the entrance of the harbor for existing condition, AP2 and AP6
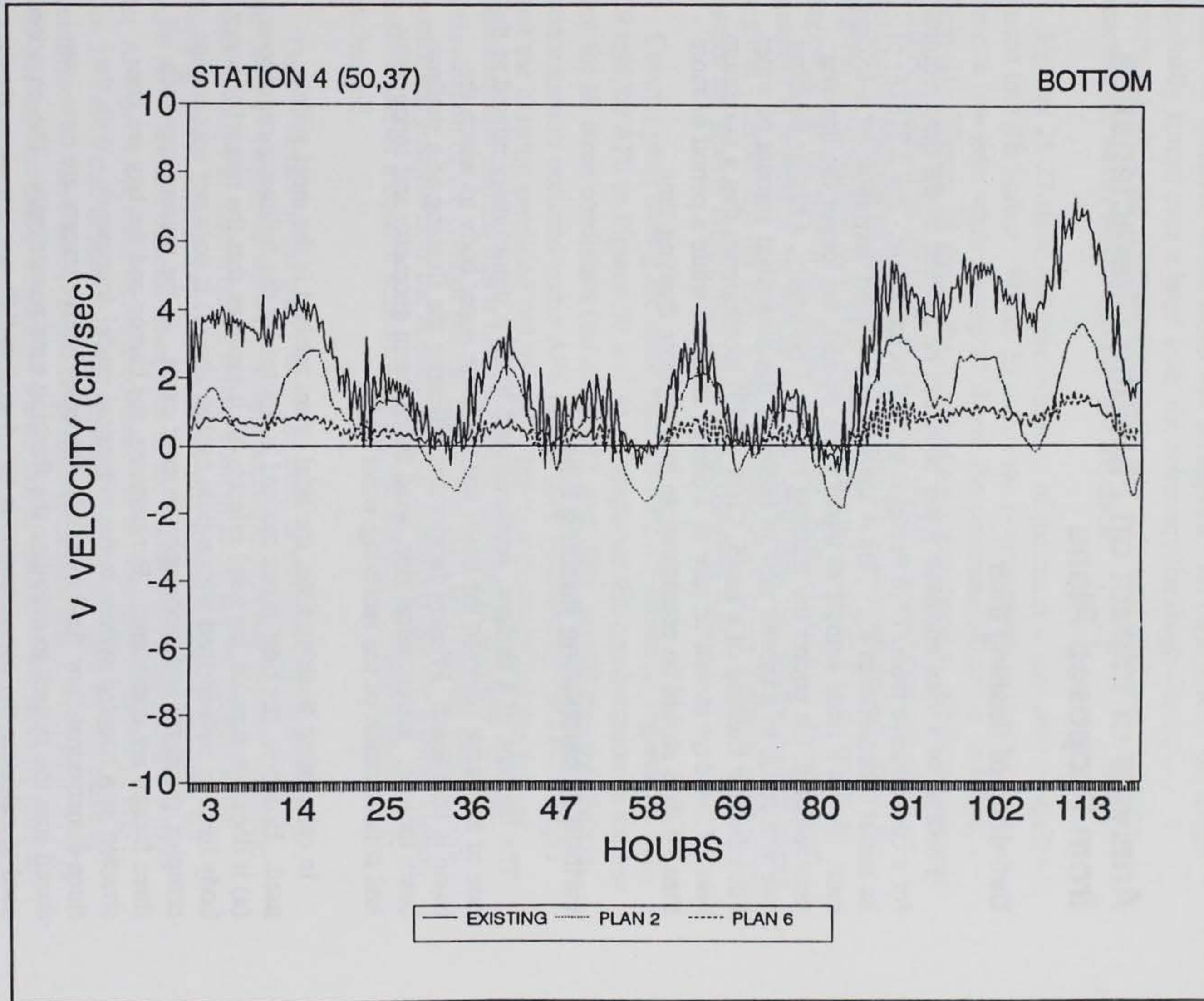
Figure 24. Time series of channel velocity (bottom layer) at the entrance of the harbor for existing
            condition, AP2 and AP6

influence on the exchange rate between the harbor and the bay. The reduction of harbor entrance velocity in AP6 is attributed to two factors. First, the creation of a constriction between the mole and the northern berth, which acts as a control section limiting the velocity through it. Second, the effect of the inverse U-shaped channel, which alters the pressure distribution around the harbor, and hence limits the exchange of harbor water and bay water.

Analysis of Impact on Flushing Characteristics from Proposed Plans

Definition of flushing time

Flushing of a semi-enclosed water body can be defined as the time required for a conservative tracer C to decrease to 36.8 percent ($1/e$, $e = 2.71828$) of its initial concentration C_0. This is the widely accepted definition for e-folding time. Given a fixed amount of tracer to be diluted, the longer the flushing time required, the poorer the flushing rate is. Conversely, a higher flushing rate will result in a shorter time to exchange the prescribed amount of water. For adequate flushing of a basin, Clark (1983) recommends that a maximum time of 2-4 days should be safe as a design criterion while a period of more than 10 days should be considered an unacceptable flushing time.

Method of calculating flushing time

The flushing of a shallow, semi-enclosed basin is dynamically related to the rate of exchange between the basin and the large water body to which the basin is connected. Primary factors that influence the flushing of a shallow basin include: astronomical tide, wind force, basin geometry and topography, and concentration of the receiving water body.

In calculating flushing time, the tidal prism method is the most widely used. However, the tidal prism method is limited by the following conditions: (a) it does not account for wind effects; (b) it assumes that the receiving water body itself is well-flushed within tidal cycles; and (c) it does not account for complex geometry and topography in most cases. In the present approach, all three factors are considered. Furthermore, the harbor and the bay are constructed as a coupled system in the numerical model framework. With the three-dimensional flow field available, the conservative tracers are now introduced into the system to calculate the flushing time numerically. The equation used to calculate the concentration is an advection-diffusion equation, similar to the one used for calculating salinity (see Chapter 2). Both are without internal source and sink terms.

50

Flushing characteristics in Maalaea Harbor

Initially, a tracer of 100 ppt was introduced into the entire harbor, with a 0-ppt tracer concentration in the bay. The boundary condition is such that during ebb, interior concentration values are advected out of the grid, while during flood, the specified return value will be applied. As time passed, the tracer gradually spread over a large area; the concentration inside the harbor decreased while the concentration in the bay increased until eventually it reached the steady state when the two are equal.

Figures 25-27 show the time evolution of the tracer 1 day after it was introduced into the harbor. Figure 25 shows the concentration at the beginning time, a low tide, while Figure 27 shows the concentration at the end time, a high tide. Figure 26 shows the intermediate concentration. While the contour usually grows in an irregular shape and a highly complex manner, there are consistent patterns recognizable throughout the simulation period. First, the highest concentration is always located at the west corner of the harbor, a region at the far side of the harbor entrance. Second, a strong concentration gradient is present at the harbor entrance, separating two relatively well-mixed regions - harbor and the bay. Third, concentrations at the northern bank of the harbor are always higher than those at the southern bank.

Contour plots during the same time for AP2 are shown in Figures 28 and 29 and for AP6 in Figures 30 and 31. Comparing the concentration in the harbor for all three conditions (existing, AP2, and AP6) reveals that the highest concentration occurred under AP6 (73.20 ppt), followed by AP2 (47.70 ppt) and the existing condition (43.95 ppt). The fact that AP6 has the highest concentration implies that it has the poorest flushing of all three. Further examination of the contour pattern shows that AP6 also has the highest concentration gradient near the constriction, an indication that the narrow section indeed acts as a control section, limiting the amount of water allowed to be exchanged.

Time histories of the tracer were recorded at stations 1, 2, and 3 inside the harbor. Figure 32 shows that the concentration at the existing condition takes 2.9 days to drop from its initial 100-ppt to 37 ppt, by definition the flushing time. Similar calculations show that flushing time is 3.3 days for AP2 (a 14-percent increase compared to the existing condition) and 6.3 days for AP6 (a 117-percent increase compared to the existing condition). Figure 33 shows that at station 2, the flushing time is 2.7 days for the existing condition, 3.2 days for AP2 (an 18-percent increase), and 5.5 days for AP6 (a 103-percent increase). Figure 34 shows that at station 3, the flushing time is 2.1 days for the existing condition, 2.3 days for AP2 (a 9.5-percent increase), and 5.3 days for AP6 (a 152-percent increase). Table 1 summarizes all the flushing times calculated at different locations under various conditions.

Figure 25. Contour plot of conservative tracer concentration at low tide, 1 day after it was introduced into the existing harbor condition

Figure 26. Contour plot of conservative tracer concentration at half tide, 1 day after it was introduced into the existing harbor condition

Figure 27. Contour plot of conservative tracer concentration at high tide, 1 day after it was introduced into the
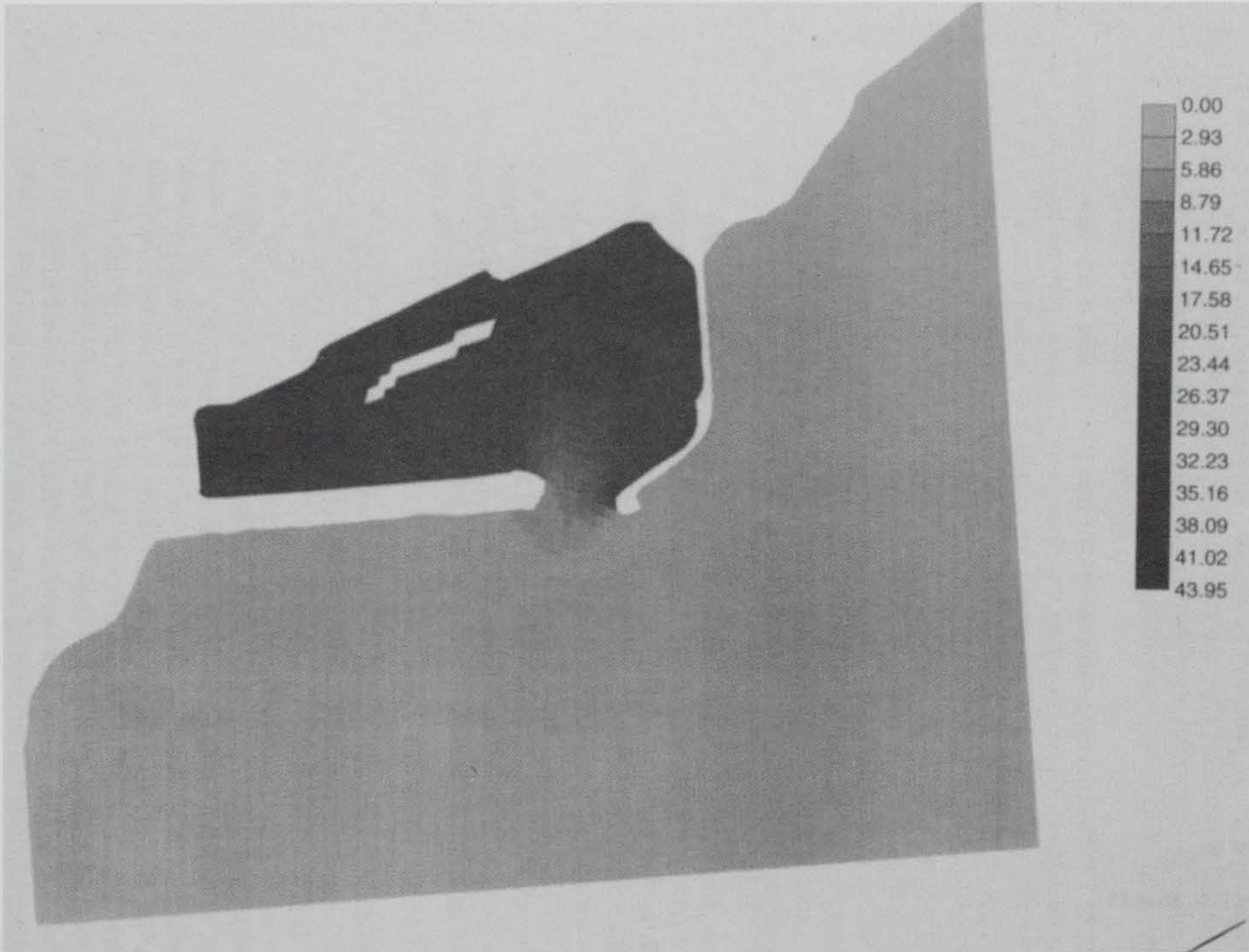existing harbor condition
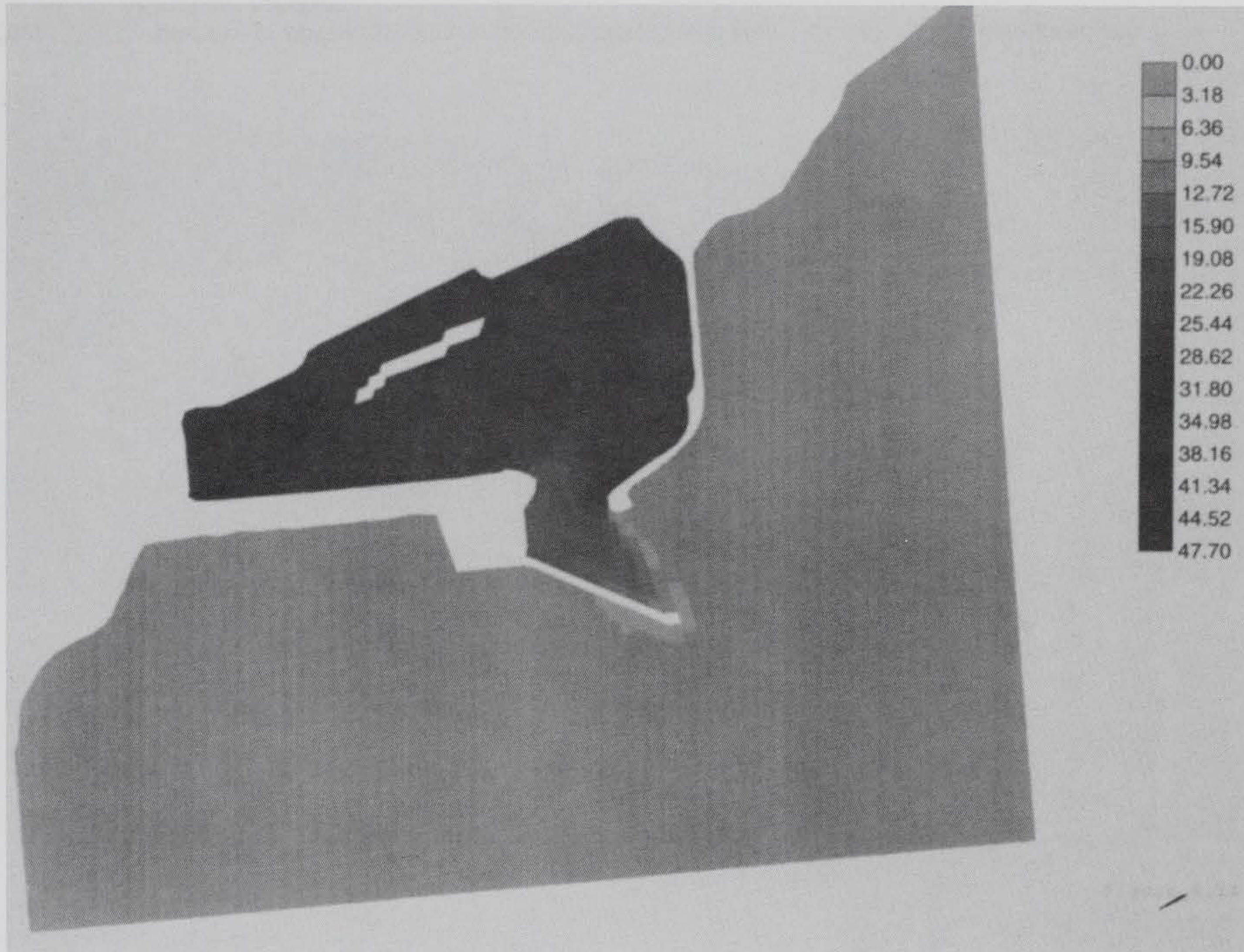
Figure 28. Contour plot of conservative tracer concentration at low tide, 1 day after it was introduced into the AP2 harbor condition
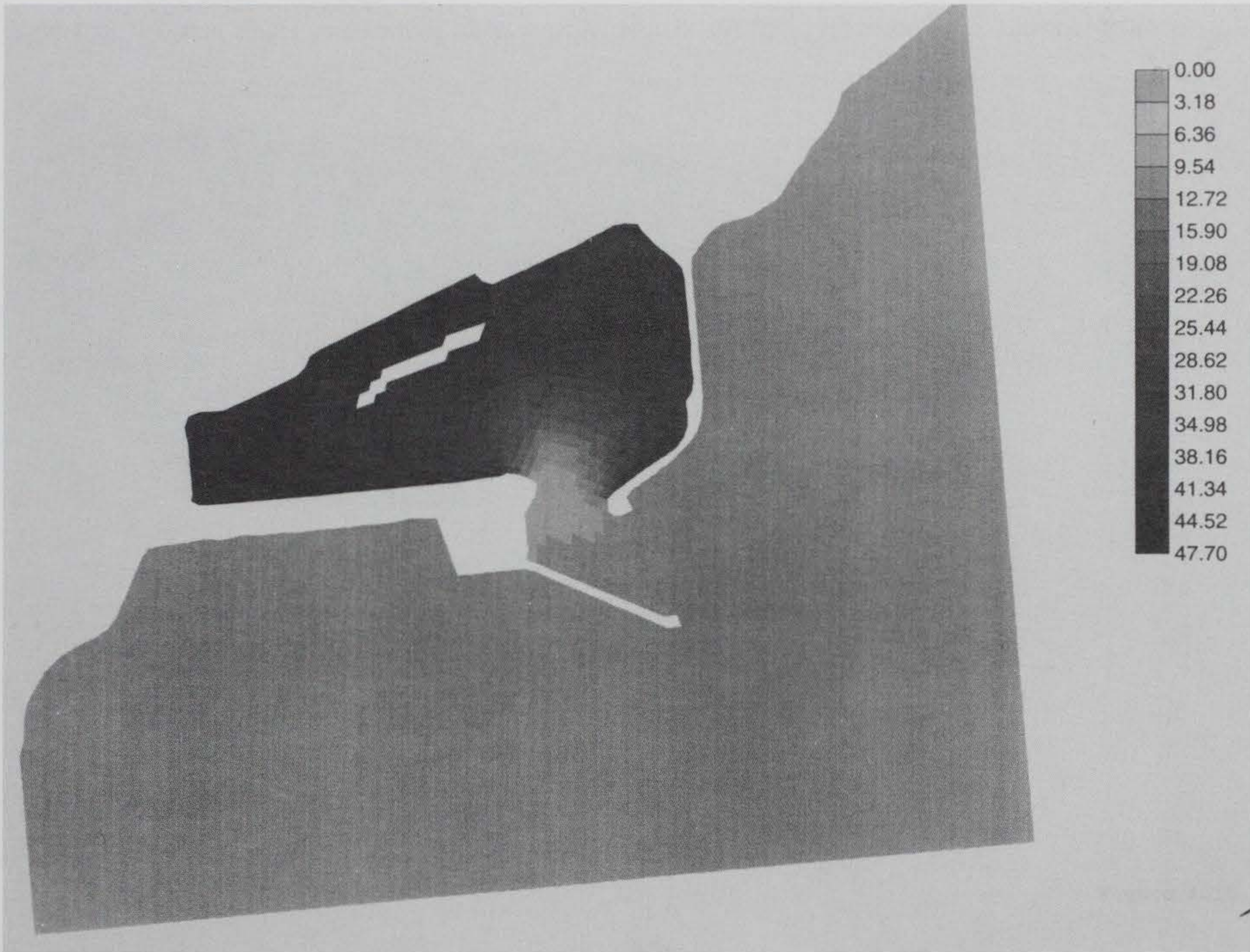
Figure 29. Contour plot of conservative tracer concentration at high tide, 1 day after it was introduced into the AP2 harbor condition
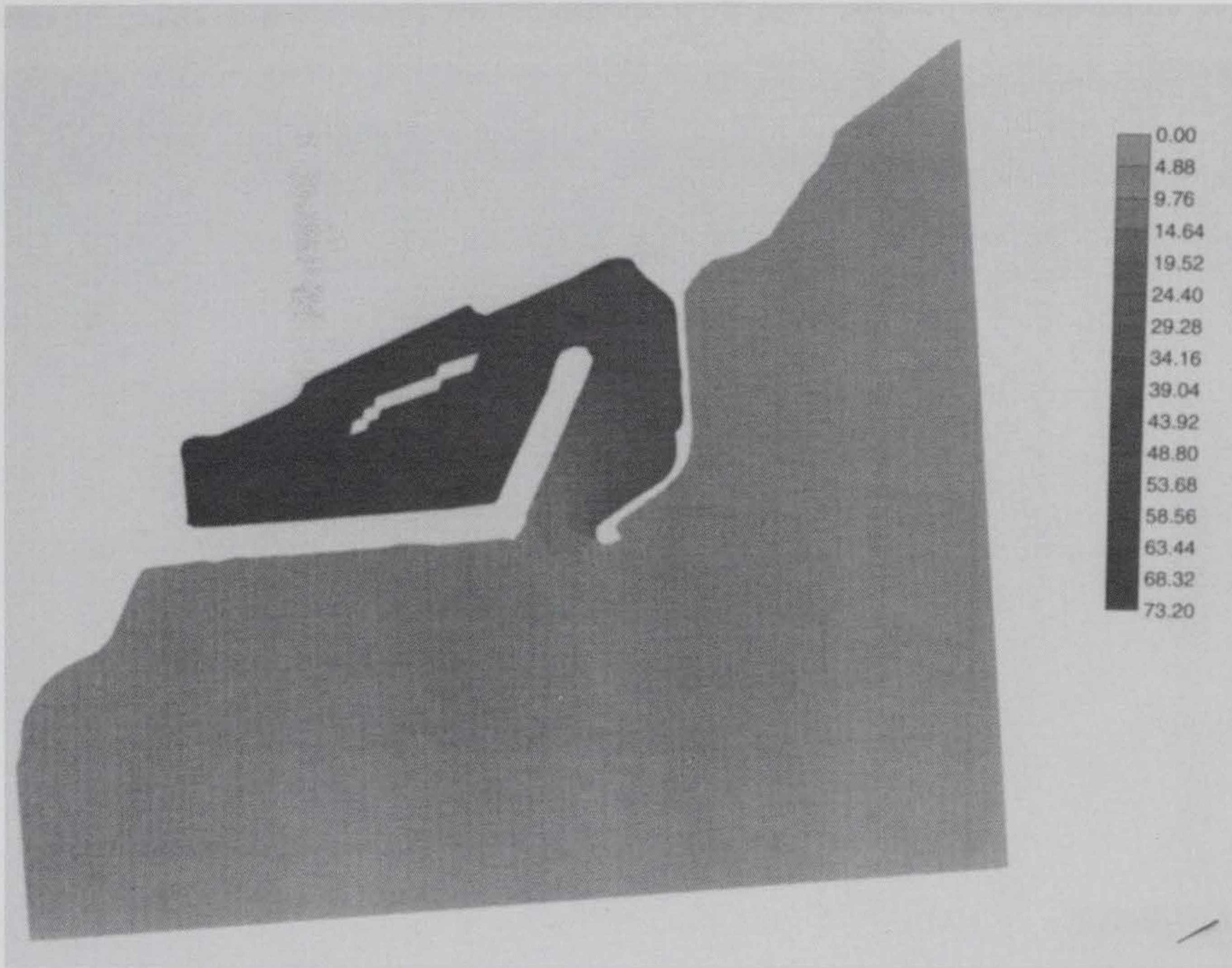
Figure 30. Contour plot of conservative tracer concentration at low tide, 1 day after it was introduced into the AP6 harbor condition
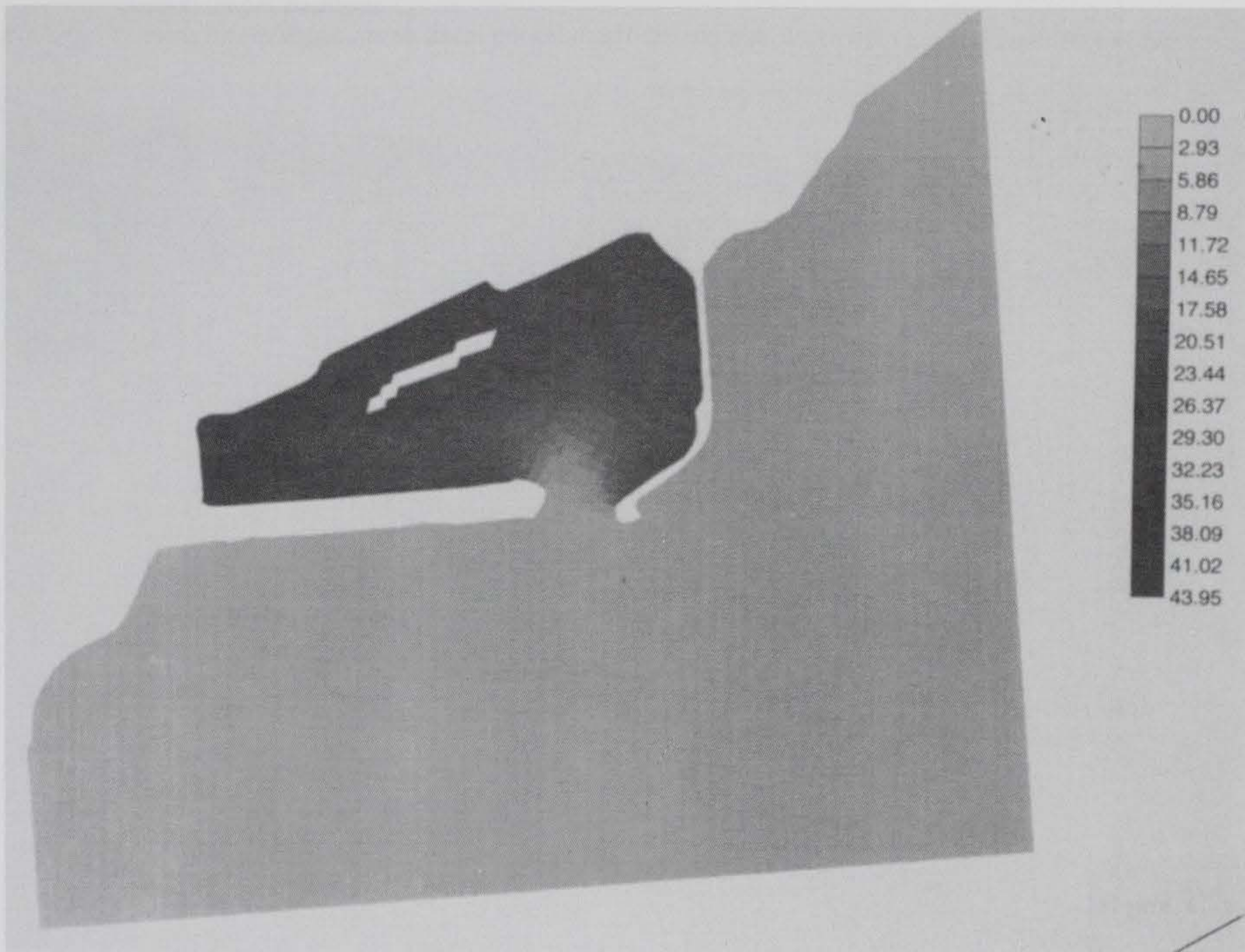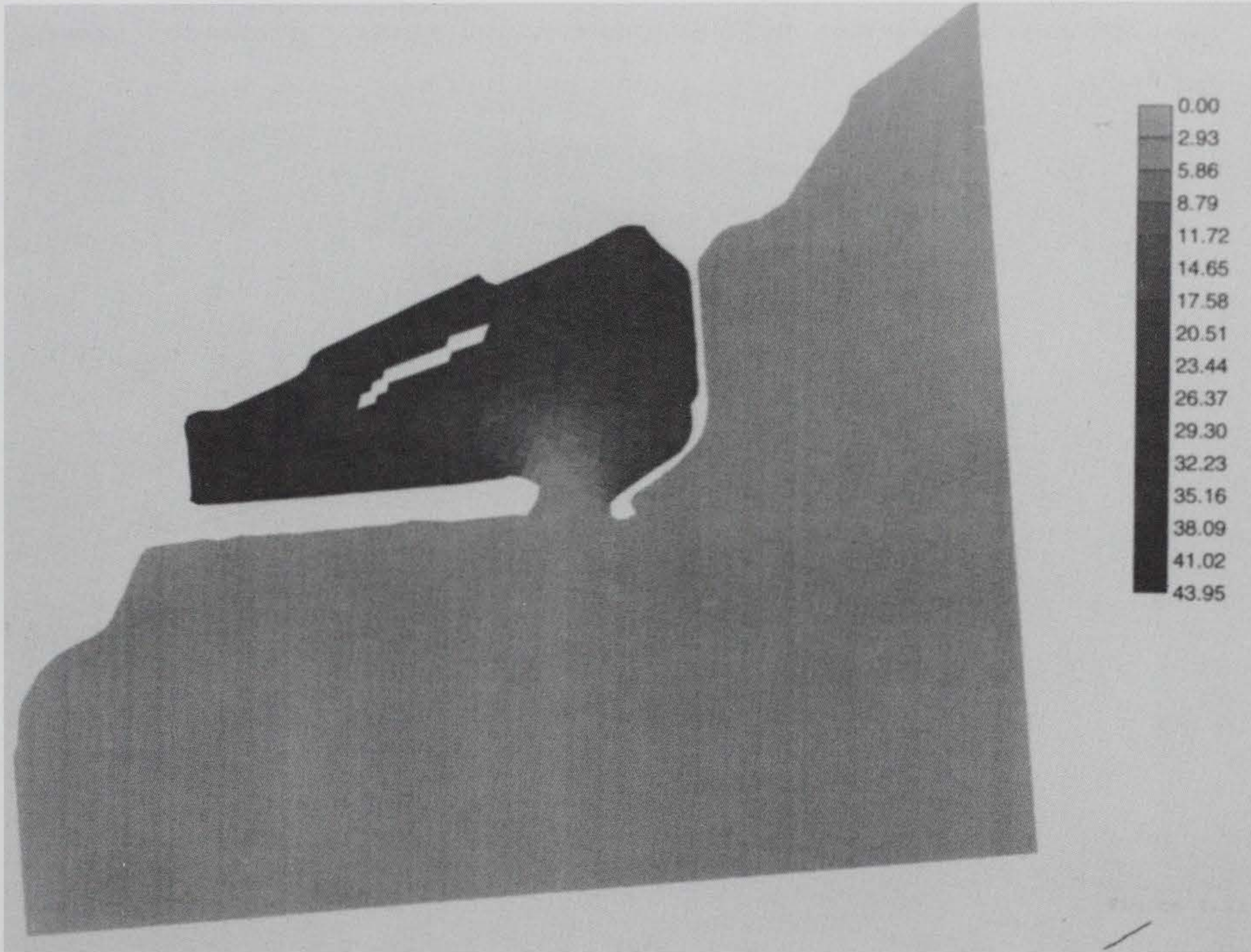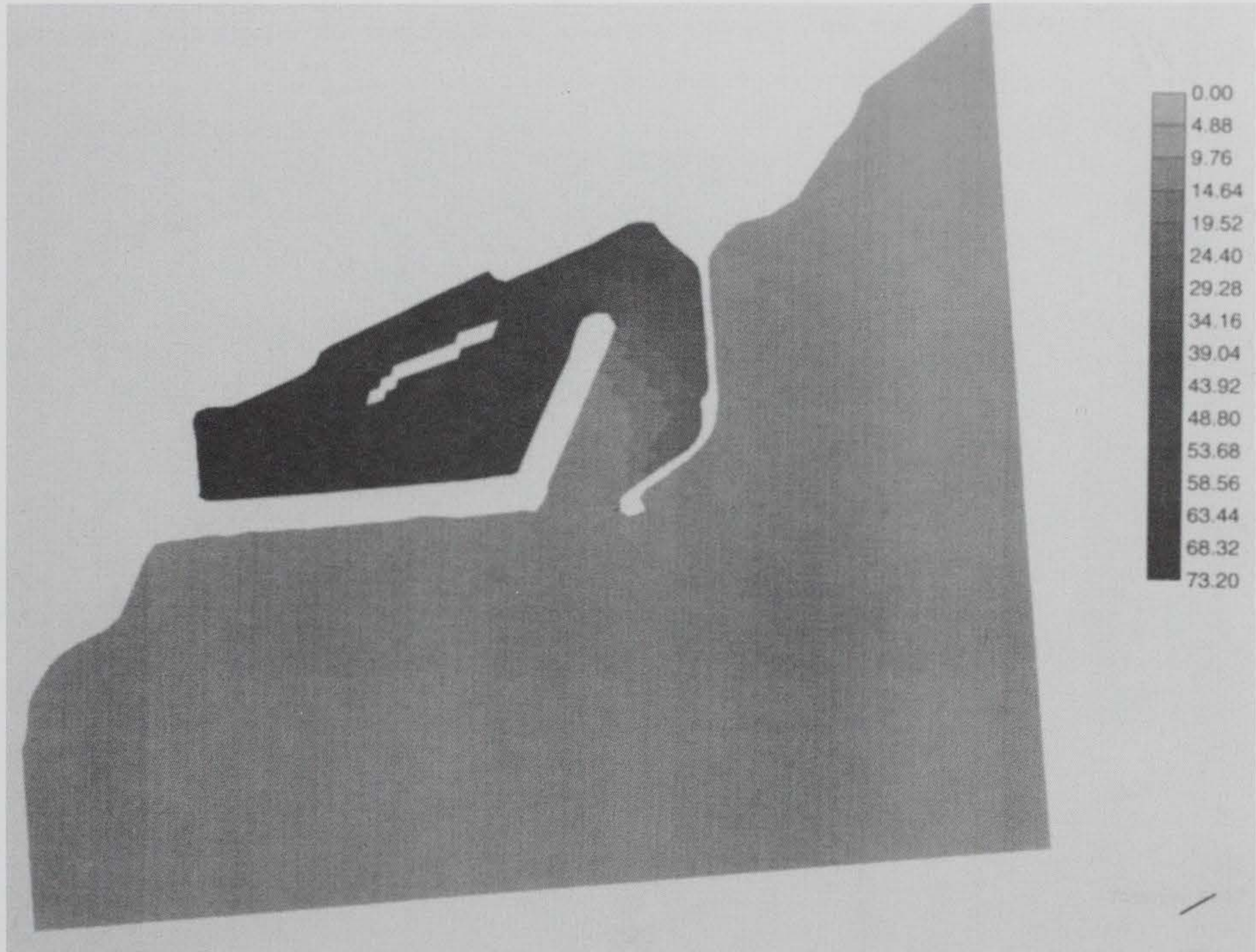
Figure 31. Contour plot of conservative tracer concentration at high tide, 1 day after it was introduced into the AP6 harbor condition
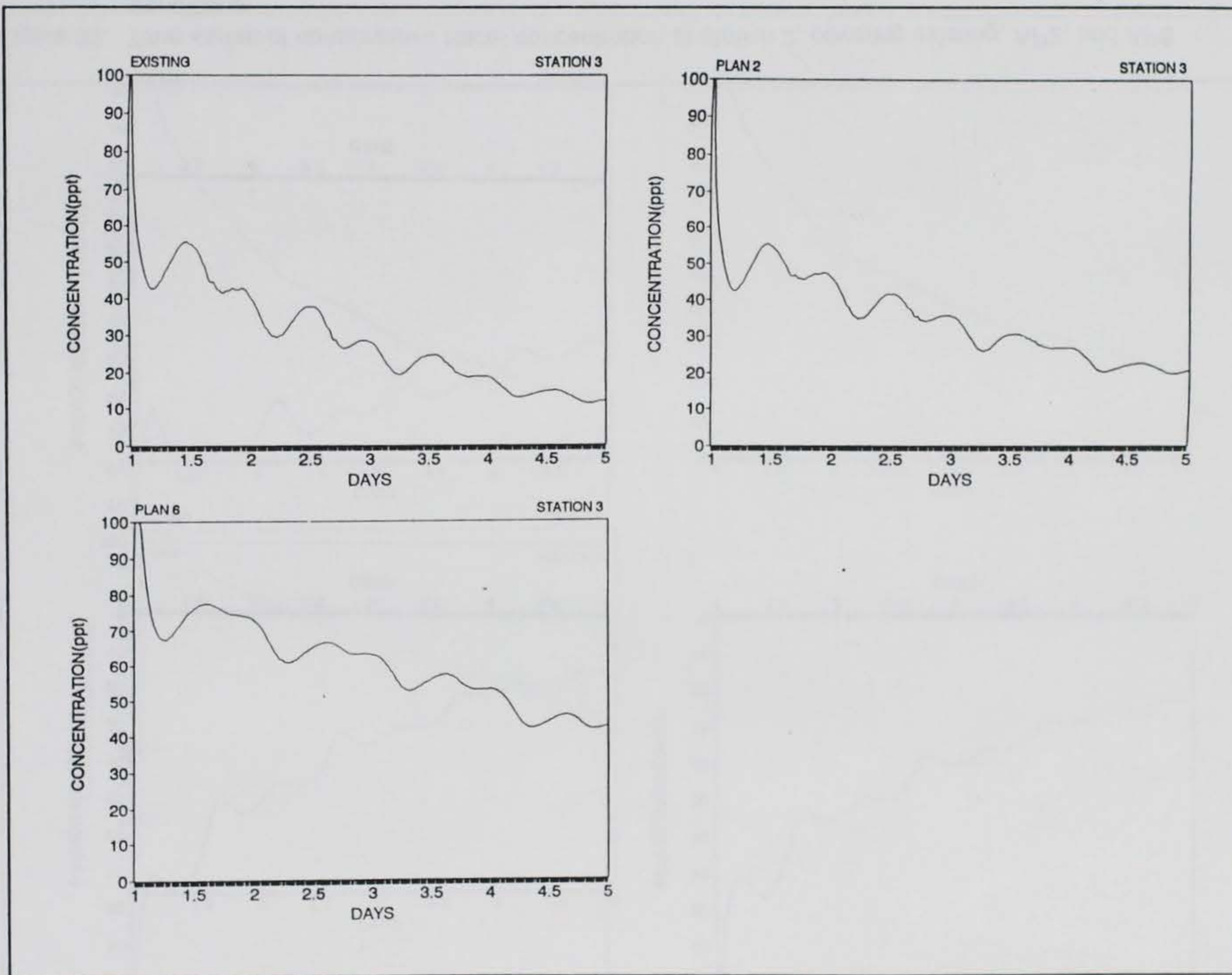
Figure 32. Time series of conservative tracer concentration at station 1, covering existing, AP2, and AP6 conditions
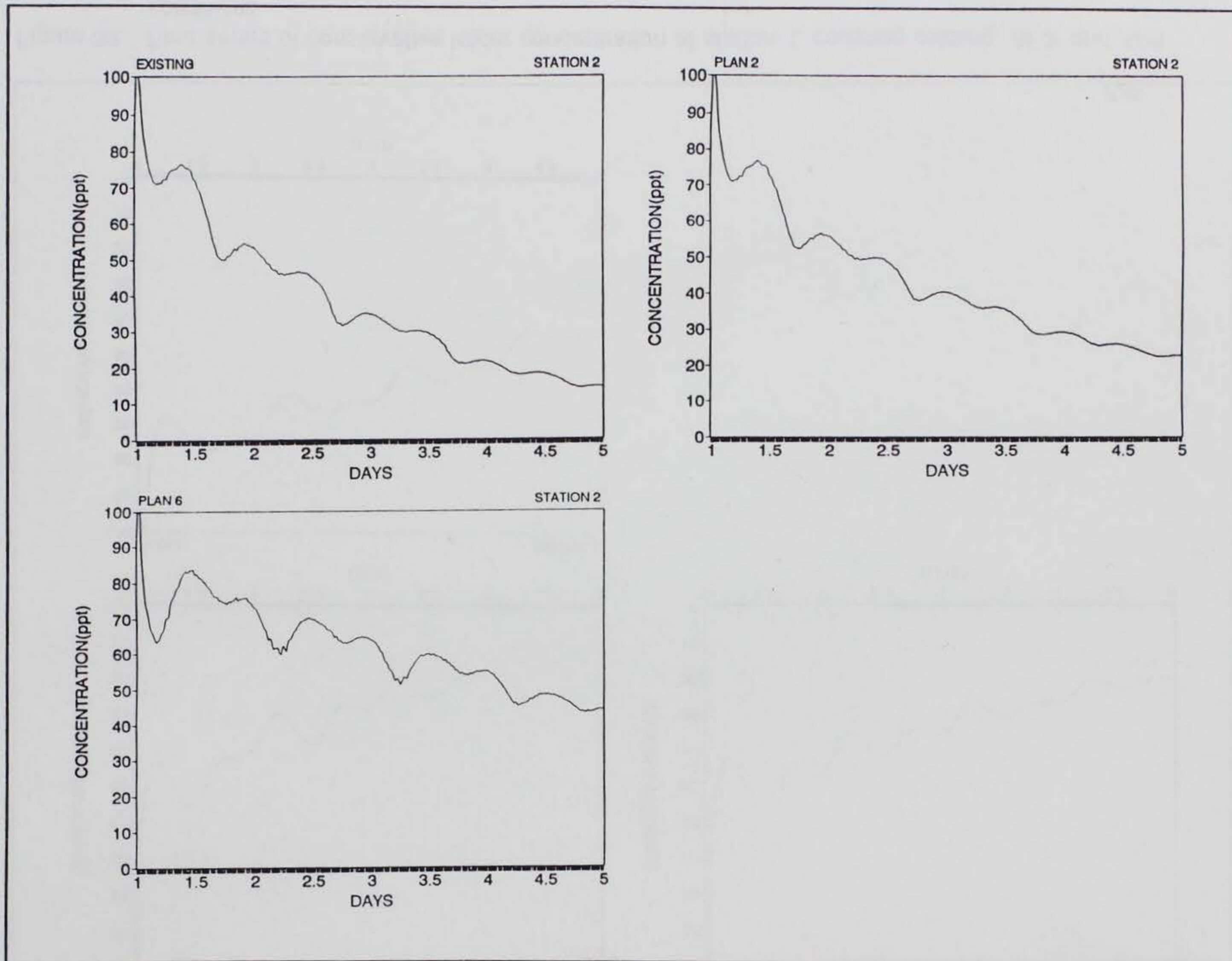
Figure 33. Time series of conservative tracer concentration at station 2, covering existing, AP2, and AP6 conditions
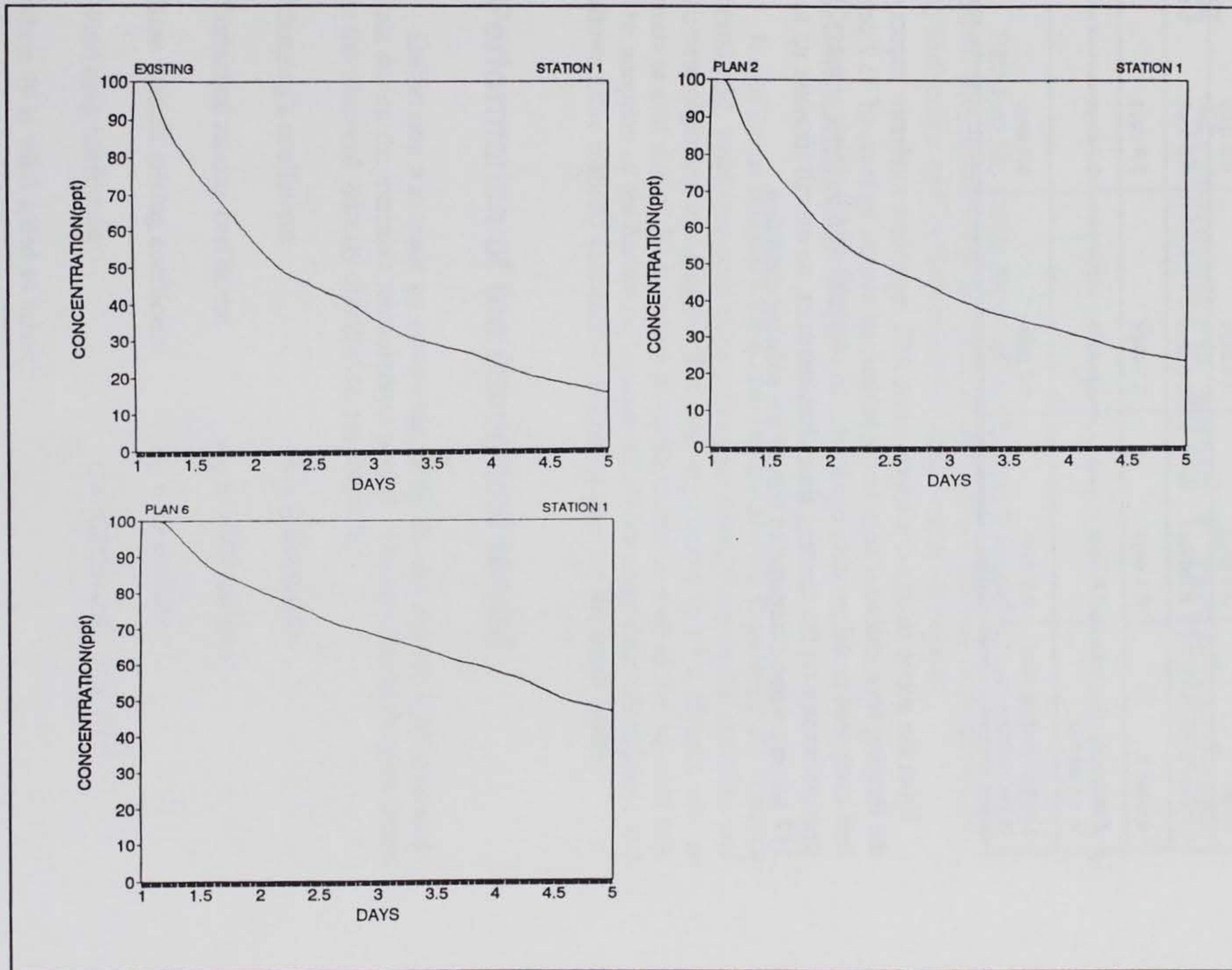
Figure 34. Time series of conservative tracer concentration at station 3, covering existing, AP2, and AP6 conditions

Table 1
Flushing Time Calculated Under Different Conditions

Station	Existing Condition	AP2	AP6
Station 1	2.9 days	3.3 days	6.3 days
Station 2	2.7 days	3.2 days	5.5 days
Station 3	2.1 days	2.3 days	5.3 days
Average flushing time in the harbor	2.6 days	2.9 days	5.7 days
Longest flushing time in the harbor	2.9 days	3.3 days	6.3 days

From the above analysis, it appears that AP2 imposes a moderate impact on the flushing time characteristics in the harbor, an overall increase of 13.7 percent compared to the existing condition. In contrast, AP6 imposes a much stronger impact on the flushing time characteristics, an overall increase up to 117 percent when compared to that of the existing condition.

5 Summary and Conclusion

Based on the results presented in Chapters 2 through 4, conclusions are drawn with regard to the performance of CH3D-WES, and its prediction of hydrodynamic and flushing properties under various conditions.

Computational Grid

A curvilinear boundary-fitted coordinate was used to generate the computational grid, which provides enhancement for fitting the irregular shoreline and discrete digitizing topography. The grid, represented by 81×60 cells with an average grid size of 50 ft, covers Maalaea Harbor as well as the adjacent bay. The adoption of the harbor-bay system eliminates unjustified assumptions and allows more realistic calculation of flushing time for the small harbor.

Performance of the Numerical Model

Calibration was made by comparing model results and the field-measured data during the intensive measurement period. The best fits of the parameters to the observed velocity distribution are found for:

Manning's coefficient $n = 0.035\text{-}0.040$

Horizontal mixing coefficient $A_H = 1,000 \text{ cm}^2/\text{sec}$

Base vertical mixing coefficient $A_V = 10 \text{ cm}^2/\text{sec}$

Wind drag coefficient $C = (0.075 + 0.67 \text{ W}) \times 10^{-3}$

where W is wind speed in m/sec.

During the validation, the model calculations are conducted without further changes and adjustments of the parameters. The model results compared favorably with the field-measured data, reaffirming the reliability of CH3D-WES. In the vertical direction, the model results show a persistent two-layered

circulation driven by the prevailing north wind, a unique feature observed in the Maalaea Harbor.

Hydrodynamic Results

The existing circulation in the Maalaea Harbor and its vicinity is strongly influenced by the prolonged north wind, resulting from the rectification of trade wind by two mountain ranges north of the harbor. The velocity in the bay generally flows southwestward with a speed of 10-15 cm/sec. The flow inside the harbor exhibits a large clockwise circulation around the coral shoal with a speed of 2-5 cm/sec. At the harbor mouth, superposed on the regular astronomical tide, is a two-layered wind-driven flow set up by the prolonged north wind.

Under AP2, the proposed breakwater has an impact on the bay circulation in that it deflects the incoming flow from southwestward to southward direction, which in turn drives a northward compensation flow in the region west of the proposed breakwater. Inside the harbor, the circulation pattern is similar to the existing condition; however, the magnitude of velocity is 10-15 percent smaller. The exchange between the harbor and the bay is somewhat reduced because the total available area for exchange at the mouth is decreased with the proposed breakwater.

Under AP6, the proposed mole structure has very little effect on the bay water outside the harbor. Inside the harbor, the original harbor proper was divided into two regions by the mole. Inside the mole, the circulation pattern changes only slightly; the velocity magnitude is similar to the existing condition. However, the velocity at the harbor mouth (outside the mole) was only 30-40 percent that of the existing condition, a significant reduction in terms of velocity magnitude. The reduction of the velocity is attributed to two factors. First, the creation of a constriction between mole and the northern berth, which acts as a control section limiting the velocity through it. Second, the effect of the inverse U-shaped channel, which alters the pressure distribution around the harbor, and hence limits the exchange of harbor water with bay water.

Analysis of Flushing Time

The concentration of conservative tracer was calculated using advection-diffusion equations in the numerical framework. Initially, a conservative tracer of 100 ppt was introduced into the entire harbor and a 0-ppt concentration was used in the bay. As concentration evolved in a complex manner with time, the contour was found to follow certain patterns. First, the highest concentration is always located at the west corner of the harbor. Second, the concentration at the northern bank of the harbor is always higher than at the southern bank. Third, a strong concentration gradient always occurs at the narrow section of the harbor. The typical calculation after 1 day of simulation shows that the

highest concentration inside the harbor is 43.95 ppt for the existing condition, 47.70 ppt for AP2, and 73.30 ppt for AP6. AP6 has the highest concentration and thus, the poorest flushing of all. Based on the e-folding formulation, it was shown that the existing harbor has a flushing time of 2.9 days. AP2 has a 3.3-day flushing time (a 14-percent increase) and AP6 has a 6.3-day flushing time (a 117-percent increase).

Additional scenario runs were conducted for Modified Alternative Plan 2 (see Appendix A for MAP2), in which the coral shoal was connected to the northern berth with a concrete causeway. The flushing time for MAP2 is 4.4 days, slightly higher than that of AP2 (3.3 days) and lower than AP6 (6.3 days).

References

Callaway, R. J. (1981). "Flushing study of South Beach Marina, Oregon."
J. Waterways, Port, Coastal, and Ocean Engin. Div., American Society of
Civil Engineers, 107(2), 47-58.

Carver, R. D., and Markle, D. G. (1981). "Stability of rubble-mound break-
water Maalaea Harbor, Maui, Hawaii, hydraulic model investigation,"
Miscellaneous Paper HL-81-1, U.S. Army Engineer Waterways Experiment
Station, Vicksburg, MS.

Clark, J. R. (1983). *Coastal ecosystem management: A technical manual for
the conservation of coastal zone resources.* John Wiley & Sons, New
York.

Donaldson, C. dup. (1973). "Atmospheric turbulence and the dispersal of
atmospheric pollutants." *Workshop on Micrometeorology.* D.A. Haugen,
ed., American Meteorological Society, Science Press, Boston, MA, 313-90.

Dyer, K. R. (1973). *Estuaries: A physical introduction.* John Wiley and
Sons, New York.

Edinger, J. E., Brady, D. K., and Geyer, J. C. (1974). "Heat exchange and
transport in the environment," Report 14, EPRI Publication
No. 74-049-00-3, prepared for Electric Power Research Institute,
Palo Alto, CA.

Garratt, J. R. (1977). "Review of drag coefficients over oceans and conti-
nents," *Monthly Weather Review* 105, 915-29.

Harleman, D. R. F. (1966). "Pollution in estuaries." *Estuary and coastline
hydrodynamics.* A. T. Ippen, ed. McGraw-Hill, Inc., New York, 630-47.

Jin, K. R. (1993). "Integration of radiation boundary condition and adaptive
grid technique in CH3D model application," unpublished paper prepared for
U.S. Army Engineer Waterways Experiment Station, Vicksburg, MS.

Johnson, B. H. (1980). "VAHM—A vertical averaged hydrodynamic model using boundary-fitted coordinates," Miscellaneous Paper HL-80-3, U.S. Army Engineer Waterways Experiment Station, Vicksburg, MS.

Johnson, B. H., Kim, K. W., Heath, R. E., and Butler, H. L. (1991). "User's guide for the Chesapeake Bay three-dimensional numerical hydrodynamic model," Technical Report HL-91-1, U.S. Army Engineer Waterways Experiment Station, Vicksburg, MS.

Leonard, B. P. (1979). "A stable and accurate convective modeling procedure based on upstream interpolation," *Computer Methods in Applied Mechanics and Engineering* 19, 59-98.

Lewellen, W. S. (1977). "Use of invariant modeling." *Handbook of turbulence.* W. Frost, ed., Plenum Press, New York, Vol 1, 237-80.

Lillycrop, L. S., Bratos, S. M., Thompson, E. F., and Rivers, P. (1993). "Wave response of proposed improvements to the small boat harbor at Maalaea, Maui, Hawaii," Miscellaneous Paper CERC-93-4, U.S. Army Engineer Waterways Experiment Station, Vicksburg, MS.

Sandford, L. P., Boicourt, W. C., and Rives, S. R. (1992). "Model for estimating tidal flushing of small embayments," *J. Waterways, Port, Coastal, and Ocean Engin. Div.*, American Society of Civil Engineers, 118(6), 635-54.

Sheng, Y. P. (1982). "Hydraulic applications of a second-order closure model of turbulent transport." *Applying research to hydraulic practice.* P. Smith, ed., American Society of Civil Engineers, New York, 106-19.

_____. (1986). "A three-dimensional mathematical model of coastal, estuarine and lake currents using boundary fitted grid" Report N. 585, A.R.A.P. Group of Titan Systems, Princeton, NJ.

_____. (1990). "A simplified second order closure model of turbulent transport," unpublished paper prepared for U.S. Army Engineer Waterways Experiment Station, Vicksburg, MS.

U.S. Army Engineer Division, Pacific Ocean. (1980). "General Design Memorandum and Final Environmental Impact Statement: Maalaea Harbor for Light-Draft Vessels," Maui, Hawaii.

U.S. Environmental Protect Agency. (1985). *Coastal marinas assessment handbook.* United States Environmental Protection Agency (USEPA) Region IV, Atlanta, Ga.

van de Kreeke, J. (1983). "Residence time: Application to small boat basins," *J. Waterways, Port, Coastal and Ocean Engin. Div.*, American Society of Civil Engineers, 109(4), 416-28.

Appendix A
An Additional Numerical Model Run for Modified Alternative Plan 2

Upon completion of numerical model runs for alternative plan 2 (AP2) and alternative plan 6 (AP6), an additional scenario run for a modified alternative plan 2 (hereafter MAP2) was requested and was conducted in the Maalaea Harbor. The modification was focused on the coral shoal region located slightly north of the central portion of the harbor. Previously, AP2 treated the coral shoal region as an isolated revetment, completely detached from the mainland. In the MAP2, however, the revetment is linked to the northern berthing area through a concrete causeway (see Figure A1).

Having adopted MAP2, the numerical hydrodynamic model was re-run using the initial boundary conditions and forcing functions identical to AP2 for a period of 5 days. Model results are analyzed and presented in terms of the velocity field and spatial and temporal variation of the conservative tracer. Figure A2 shows the spatial distribution of the surface velocity field at day 3 (0730, 30 July 1993) when the wind is blowing from the northeast and the tide stage is at high tide. It is obvious that the new concrete causeway in MAP2 has a blocking effect on flows, preventing water from moving through the old passway between the revetment and the northern berthing. Figures A3 and A4 show the spatial plot of conservative tracers 1 day after they were introduced in the harbor at high tide and low tide, respectively. Figure A5 shows the time variation of the tracer concentration for the entire 5-day simulation period. Initially, concentrations for all three stations were equally high; then each station decreased gradually according to the exchange rate with the receiving water. Based on the e-folding formula, flushing time is the time required for concentration to reach 37 percent of its original value. Table A1 lists flushing times under different conditions for each of the three stations.

Under MAP2, the calculated longest flushing time for Maalaea Harbor is 4.4 days, which is higher than that of AP2 (3.3 days) and lower than AP6 (6.3 days); however, it is still under the EPA's coastal marina criteria (5 days).

Table A1
Flushing Times Under Different Conditions Including MAP2

Station	Existing	AP2	AP6	MAP2
Station 1	2.9	3.3	6.3	4.4
Station 2	2.7	3.2	5.5	4.1
Station 3	2.1	2.3	5.3	3.8
Averaged flushing time	2.6	2.9	5.7	4.1
Longest flushing time	2.9	3.3	6.3	4.4

As for individual stations in the harbor, station 1 in the far west has the longest flushing time (4.4 days), followed by station 2 in the north (4.1 days), and station 3 in the south (3.8 days). The average flushing time is 4.1 days for MAP2.
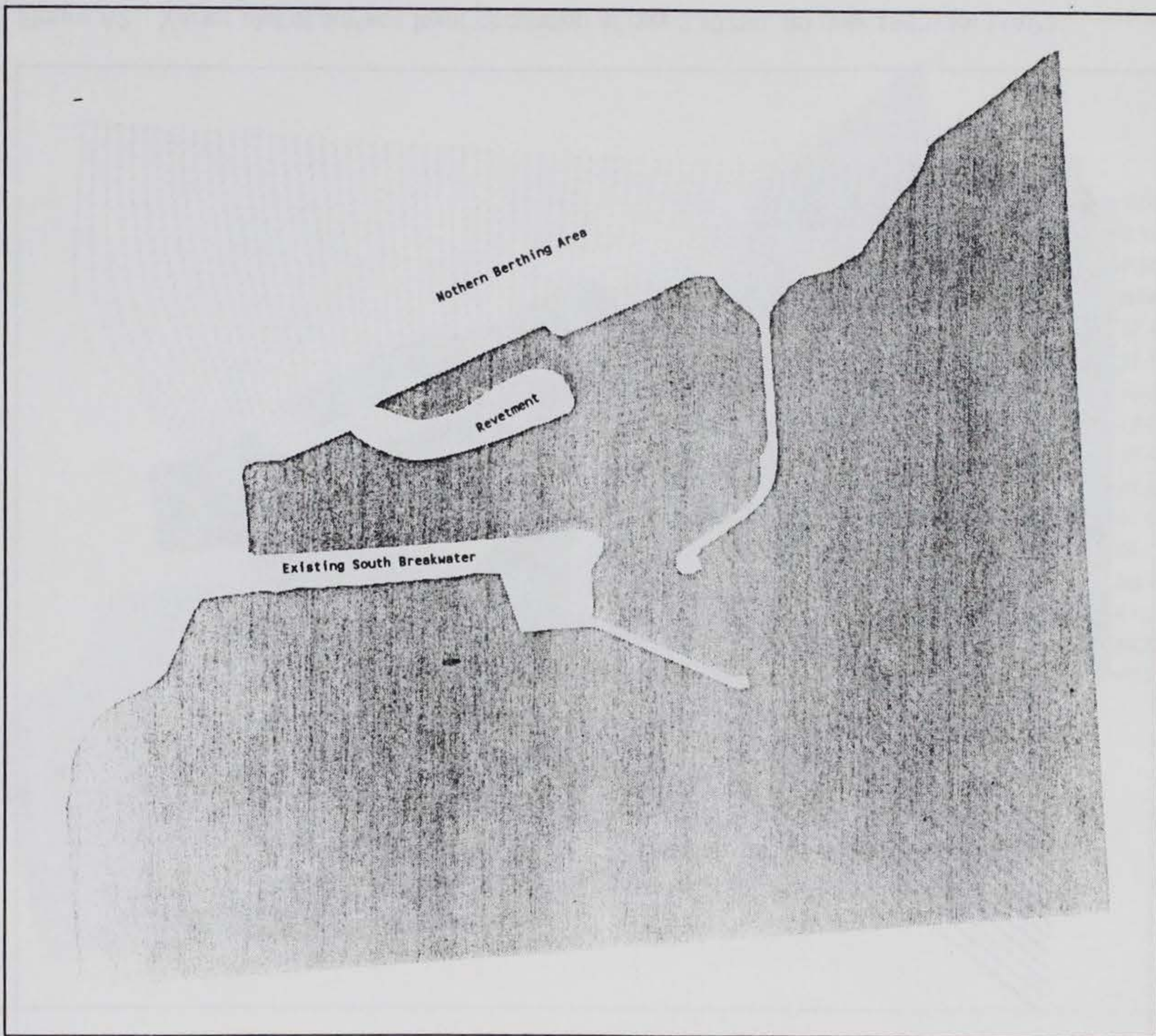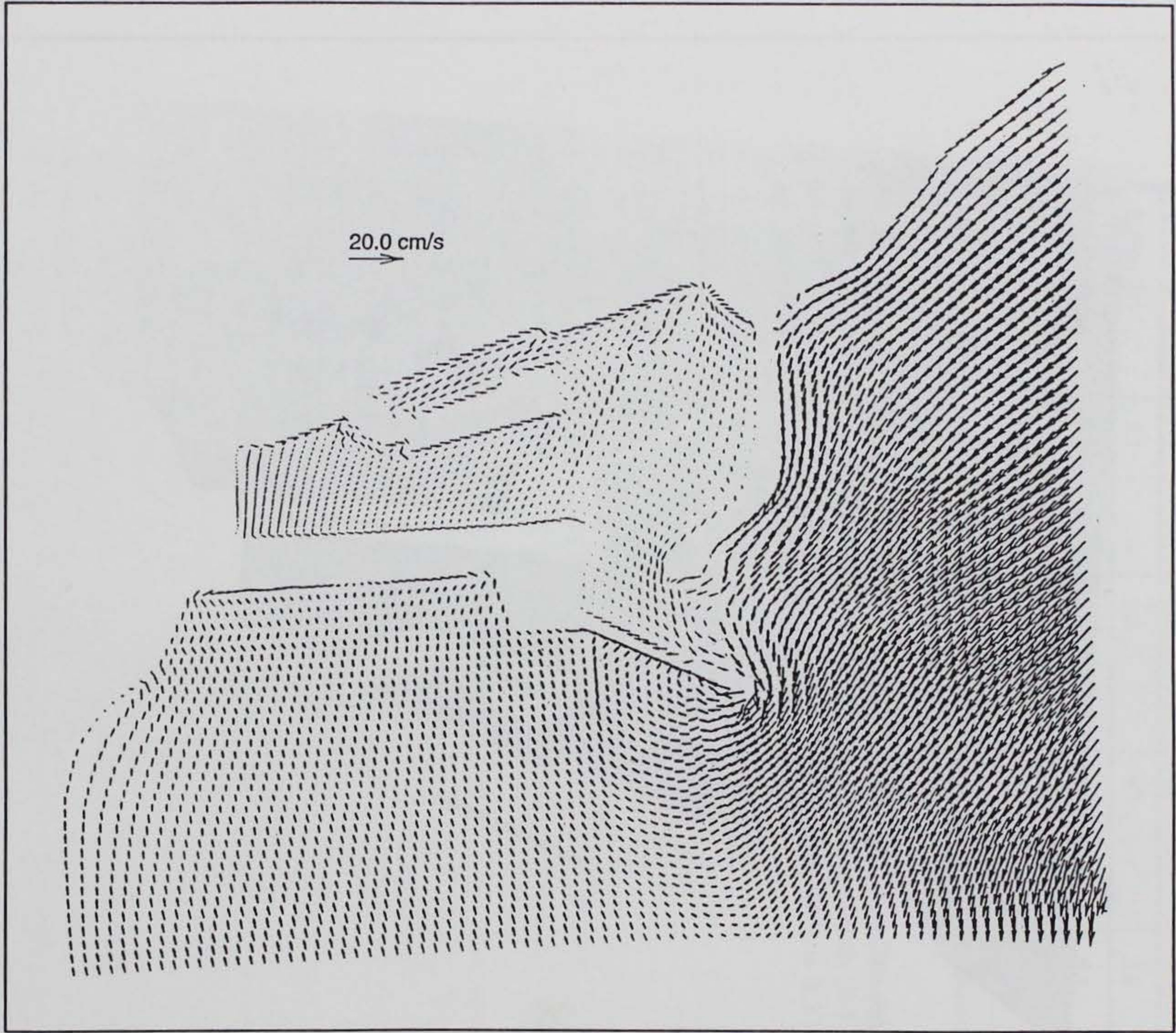
Figure A1. Geometry for MAP2

Figure A2.   Vector plot of surface layer circulation at day 3 (0730, 30 July 1993) for MAP2
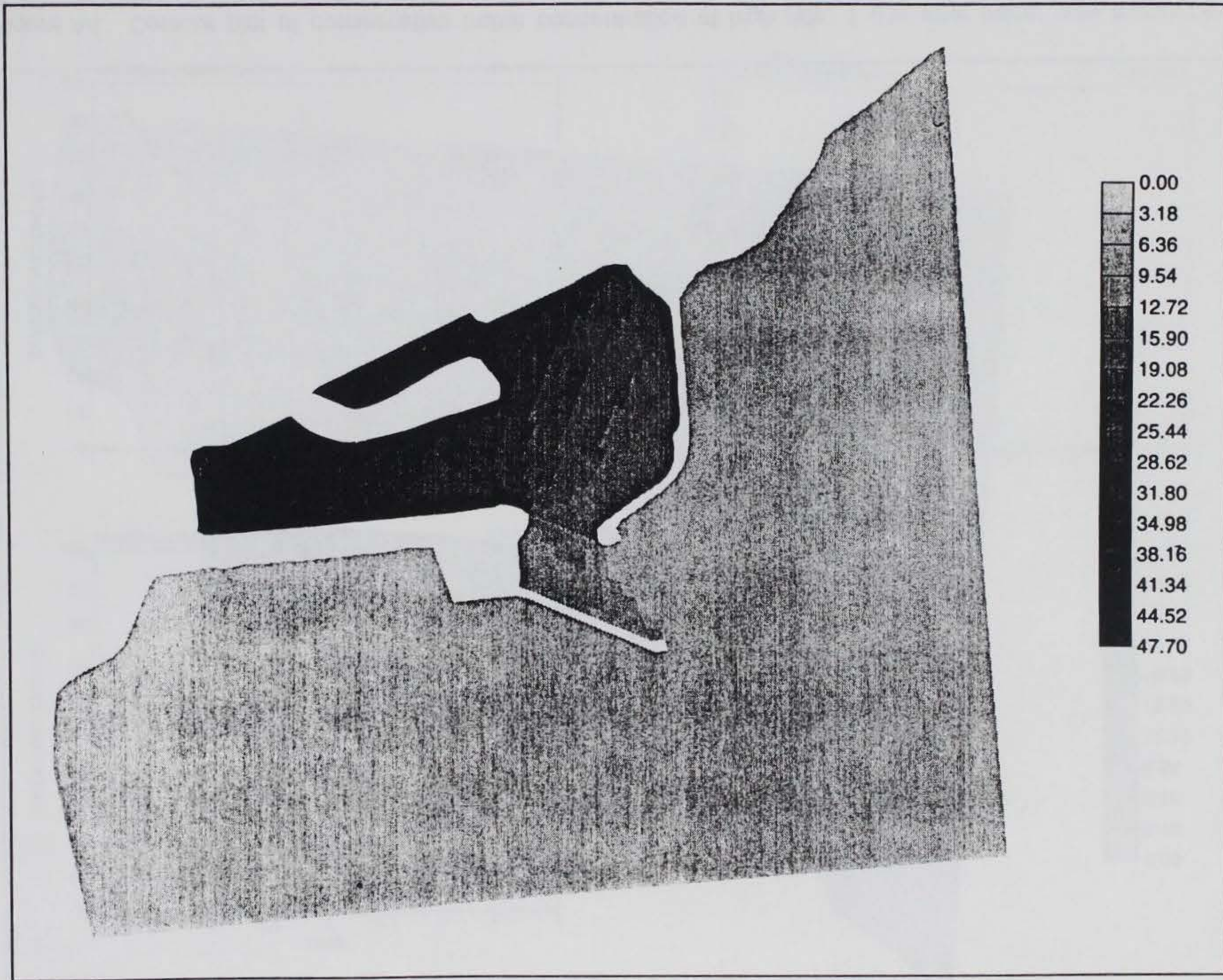
Figure A3. Contour plot of conservative tracer concentration at low tide, 1 day after tracer was introduced into the harbor under MAP2
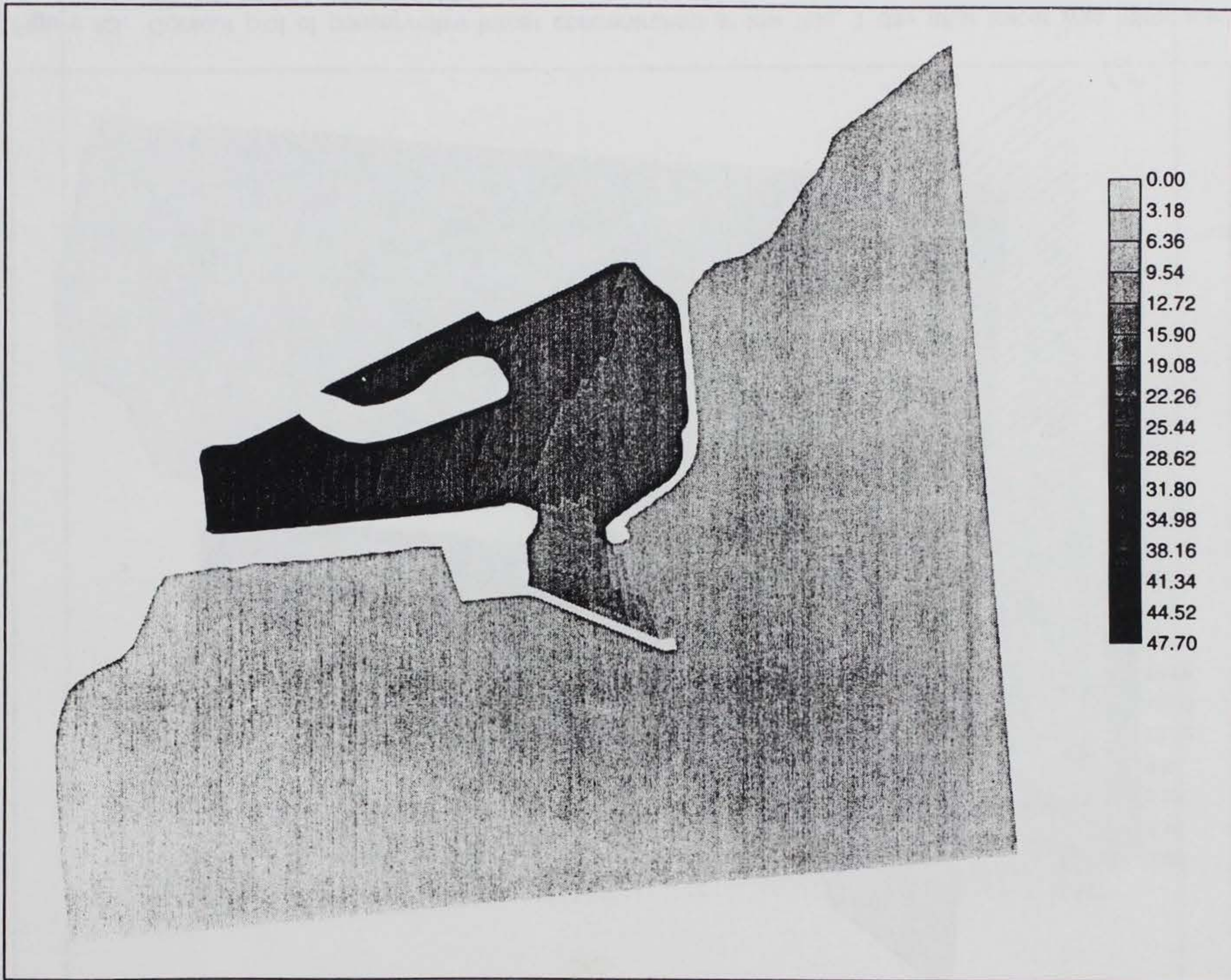
Figure A4.   Contour plot of conservative tracer concentration at high tide, 1 day after tracer was introduced into the harbor under MAP2
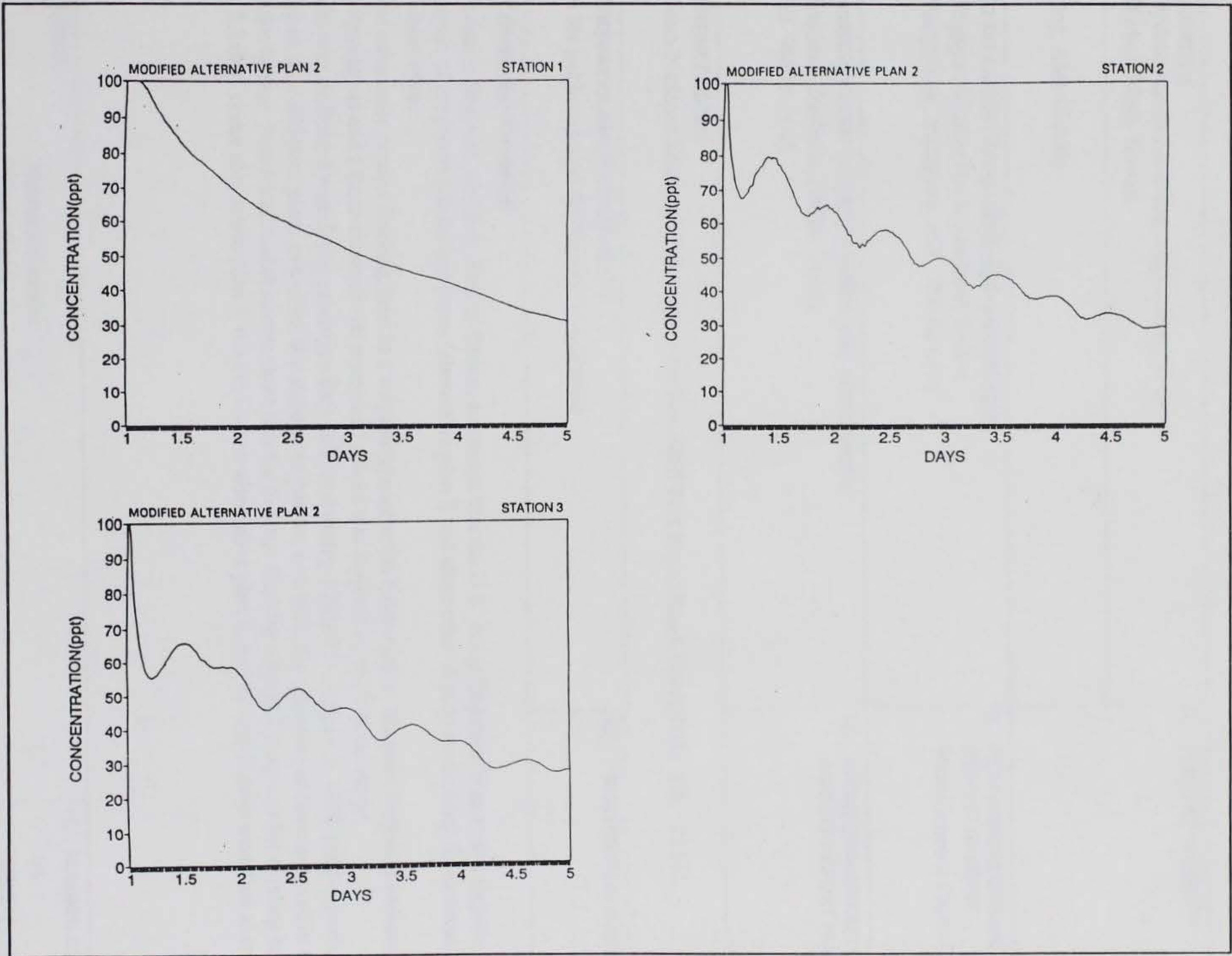
Figure A5.   Time series of conservative tracer concentration under MAP2 for stations 1, 2, and 3

REPORT DOCUMENTATION PAGE

Public reporting burden for this collection of information is estimated to average 1 hour per response, including the time for reviewing instructions, searching existing data sources, gathering and maintaining the data needed, and completing and reviewing the collection of information. Send comments regarding this burden estimate or any other aspect of this collection of information, including suggestions for reducing this burden, to Washington Headquarters Services, Directorate for Information Operations and Reports, 1215 Jefferson Davis Highway, Suite 1204, Arlington, VA 22202-4302, and to the Office of Management and Budget, Paperwork Reduction Project (0704-0188), Washington, DC 20503.

1. AGENCY USE ONLY (Leave blank)	2. REPORT DATE September 1995	3. REPORT TYPE AND DATES COVERED Final report

4. TITLE AND SUBTITLE
Numerical Hydrodynamic Modeling and Flushing Study
at Maalaea Harbor, Maui, Hawaii

5. FUNDING NUMBERS

6. AUTHOR(S)
Harry V. Wang, Alan Cialone

7. PERFORMING ORGANIZATION NAME(S) AND ADDRESS(ES)
U.S. Army Engineer Waterways Experiment Station
3909 Halls Ferry Road, Vicksburg, MS 39180-6199

8. PERFORMING ORGANIZATION REPORT NUMBER
Miscellaneous Paper CERC-95-8

9. SPONSORING/MONITORING AGENCY NAME(S) AND ADDRESS(ES)
U.S. Army Engineer Division, Pacific Ocean,
Ft. Shafter, HI 96858-5440

10. SPONSORING/MONITORING AGENCY REPORT NUMBER

11. SUPPLEMENTARY NOTES
Available from National Technical Information Service, 5285 Port Royal Road, Springfield, VA 22161.

12a. DISTRIBUTION/AVAILABILITY STATEMENT
Approved for public release; distribution is unlimited.

12b. DISTRIBUTION CODE

13. ABSTRACT (Maximum 200 words)

The U.S. Army Engineer Division, Pacific Ocean, requested that the U.S. Army Engineer Waterways Experiment Station study the impact of proposed breakwater plans (alternative plan 2 and alternative plan 6) on flushing characteristics in the Maalaea Harbor, Maui.

In order to accurately predict flushing time in a wind-dominant water body such as Maalaea Harbor, a harbor-bay coupled system was developed and a three-dimensional numerical model was invoked to conduct the study.

The model was calibrated with 5-day prototype data collected during a July 27 - August 3, 1993, field experiment, The report describes how different plans can affect the circulation pattern and, thus, the transport of the conservative tracer, inside and outside the harbor. Numerical model results show that the average flushing time is 2.9 days under existing harbor conditions, 3.3 days under alternative plan 2, 6.3 days under alternative plan 6, and 4.1 days under modified alternative plan 2.

14. SUBJECT TERMS
Circulation
Hydrodynamics
Maalaea Harbor
Numerical model
Wind effects

15. NUMBER OF PAGES
84

16. PRICE CODE

17. SECURITY CLASSIFICATION OF REPORT UNCLASSIFIED	18. SECURITY CLASSIFICATION OF THIS PAGE UNCLASSIFIED	19. SECURITY CLASSIFICATION OF ABSTRACT	20. LIMITATION OF ABSTRACT